DETERMINATION OF THE OPTICAL AND DYNAMIC PROPERTIES OF TURBID MEDIA VIA INTERFEROMETRIC DIFFUSE OPTICS

BINBIN ZHANG

DETERMINATION OF THE OPTICAL AND DYNAMIC PROPERTIES OF TURBID MEDIA VIA INTERFEROMETRIC DIFFUSE OPTICS

DETERMINATION OF THE OPTICAL AND DYNAMIC PROPERTIES OF TURBID MEDIA VIA INTERFEROMETRIC DIFFUSE OPTICS

Dissertation

for the purpose of obtaining the degree of doctor
at Delft University of Technology
by the authority of the Rector Magnificus,
prof. dr. ir. H. Bijl,
chair of the Board for Doctorates
to be defended publicly on Wednesday, 11 March 2026, 12:30.

by

Binbin ZHANG

This dissertation has been approved by the promotor and the copromotor.

Composition of the doctoral committee:

Rector Magnificus,	chairperson
Dr. N. Bhattacharya,	Delft University of Technology, promotor
Dr. ir. S. Iskander-Rizk ,	Delft University of Technology, copromotor
Independent members:	
Prof. dr. J. Dankelman,	Delft University of Technology
Prof. dr. ir. C. Poelma,	Delft University of Technology
Prof. dr. A. P. Mosk,	Utrecht University
Prof. dr. T. Durduran,	ICFO-The Institute of Photonic Sciences, Spain
Dr. V. J. Srinivasan,	NYU Grossman School of Medicine, USA
Dr. S. H. Hossein Nia Kani,	Delft University of Technology, reserve member

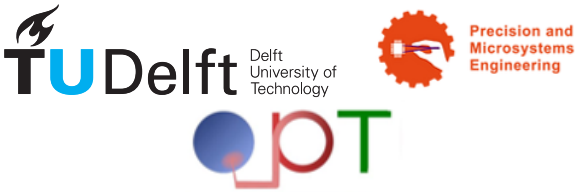

Keywords: Diffuse optics, interference, blood flow, scattering, absorption, quantum-limited detection

Printed by: Proefschriftmaken

Cover art: A scanning laser illuminates the human head and scattered photons are interfered with the reference beam at a camera. Partly generated with ChatGPT by B. Zhang.

ISBN 978-94-6384-927-2

An electronic version of this dissertation is available at
http://repository.tudelft.nl/.

Propositions

accompanying the dissertation

DETERMINATION OF THE OPTICAL AND DYNAMIC PROPERTIES OF TURBID MEDIA VIA INTERFEROMETRIC DIFFUSE OPTICS

by

Binbin Zhang

1. Signal-to-noise ratio, deep-layer specificity, and data throughput are the trade-off triangle in interferometric diffuse optics (iDO). (This thesis)
2. Time-of-flight discrimination allows for higher photon throughput and spatial resolution in speckle-based flow measurement. (This thesis)
3. Coherence gate is more robust than the electrical gate used in photon-counting techniques. (This thesis)
4. Wearability and information richness are conflicting goals in interferometric diffuse optics, posing a key challenge for practical system design. (This thesis)
5. Optical brain-computer interface (BCI) provides a non-invasive approach to access brain activities, which is complementary to electroencephalogram (EEG).
6. Photons are information shuttles; deciphering their messages is the art of photonics.
7. Life flows like a sinusoidal wave—our descents are not defeats, but the gathering of kinetic energy for the next ascent.
8. Through hardship, the spirit finds liberation.
9. Intuition reveals where the treasure lies; logic provides the tools to unearth it.
10. Sometimes growth begins with resisting who you were.

Those propositions are regarded as opposable and defendable, and have been approved as such by the promotor Dr. N. Bhattacharya and copromotor Dr. S. Iskander-Rizk.

Being thin, the blade finds the natural gaps and slides through with ease.

Zhuang Zhou, BC 369

Contents

SUMMARY

This thesis presents a comprehensive investigation into the determination of optical and dynamical properties of turbid media, with the ultimate goal of developing a non-invasive, portable, and potentially wearable interferometric diffuse optics system for cerebral blood flow (CBF) measurement. The work is organized into six chapters.

In Chapter 1, we provide an overview of the field of diffuse optics, covering techniques such as near-infrared spectroscopy (NIRS), diffuse correlation spectroscopy (DCS), laser Doppler flowmetry (LDF), and speckle contrast optical spectroscopy (SCOS). We also review the current state of cerebral blood flow measurement using diffuse optics and articulate the motivation behind this thesis.

Chapter 2 introduces a novel technique that combines time-domain near-infrared spectroscopy (TD-NIRS) and diffusing-wave spectroscopy (DWS) using a single-cavity dual-comb laser—termed dual-comb diffusing-wave spectroscopy (DC-DWS). Leveraging asynchronous optical sampling (ASOPS) and the high mutual coherence of the dual-comb source, we demonstrate the reconstruction of the diffuse time-of-flight (DTOF) distribution from turbid media, enabling the retrieval of optical properties. By repeatedly measuring DTOF faster than the decorrelation time of scatterers and compensating for laser phase fluctuations using a reference interferometer, we extract dynamic information as well. We further optimize the system in terms of temporal resolution, measurement speed, and signal-to-noise ratio (SNR). DC-DWS enables simultaneous measurement of optical and dynamic properties in a single modality, and its time-of-flight (ToF) discrimination helps mitigate shallow-layer contamination, making it valuable for CBF monitoring.

Due to the stringent temporal and spatial coherence requirements, DC-DWS collects only single or few speckles, resulting in limited photon throughput. Moreover, dual-comb interferometry suffers from low photon utilization. To address these issues, Chapter 3 introduces frequency-modulated scattering holography (FMSH). FMSH utilizes the slow frequency modulation speed and replaces single-point detectors with a camera, where each pixel captures a temporal interferogram. This camera-wise detection enables parallel acquisition of DTOF and Doppler-broadened DTOF signals, allowing for both static and dynamic measurements. The parallel nature of the detection provides SNR performance comparable to, or better than, photon-counting detectors.

In Chapter 4, we demonstrate that FMSH can measure depth-dependent speckle contrast by applying a time-frequency domain bandpass (BP) filter. This filter removes the DC component of the interferogram and suppresses short-ToF photons, effectively acting as a ToF gate. As a result, FMSH enhances specificity to deep tissue blood flow.

However, the combination of high parallel detection and high frame rate in FMSH leads to substantial data throughput, which challenges real-time processing. To address this, Chapter 5 introduces a simplified system that combines a modulated distributed-

feedback laser with a conventional CMOS camera. Rapid modulation of the laser diode during the camera exposure time selectively enables interference between photons with specific times of flight, thereby generating depth-resolved heterodyne speckle holography. This approach enhances sensitivity to deep-layer flow even at short source–detector separations, while substantially reducing system complexity and data volume.

Finally, Chapter 6 summarizes the key findings of the thesis and discusses potential directions for future research.

SAMENVATTING

Dit proefschrift presenteert een uitgebreid onderzoek naar de bepaling van optische en dynamische eigenschappen van troebele media, met als uiteindelijk doel de ontwikkeling van een niet-invasief, draagbaar en mogelijk draagbaar interferometrisch diffuus optisch systeem voor het meten van de cerebrale bloedstroom (CBF). Het werk is onderverdeeld in zes hoofdstukken.

In hoofdstuk 1 geven we een overzicht van het vakgebied diffuse optica, met technieken zoals nabij-infraroodspectroscopie (NIRS), diffuse correlatiespectroscopie (DCS), laserdopplerflowmetrie (LDF) en speckle contrast optische spectroscopie (SCOS). We bespreken ook de huidige stand van zaken op het gebied van cerebrale bloedstroommeting met behulp van diffuse optica en beschrijven de motivatie achter dit proefschrift.

Hoofdstuk 2 introduceert een nieuwe techniek die tijdsdomein nabij infraroodspectroscopie (TD-NIRS) en diffusing-wave spectroscopie (DWS) combineert met behulp van een laser met één holte en dubbele kam – genaamd dual-comb diffusing-wave spectroscopie (DC-DWS). Door gebruik te maken van asynchrone optische bemonstering (ASOPS) en de hoge wederzijdse coherentie van de bron met dubbele kam, demonstreren we de reconstructie van de diffuse time-of-flight (DTOF)-verdeling vanuit troebele media, waardoor optische eigenschappen kunnen worden bepaald. Door herhaaldelijk DTOF sneller te meten dan de decorrelatietijd van verstrooiers en te compenseren voor laserfasefluctuaties met behulp van een referentie-interferometer, extraheren we ook dynamische informatie. We optimaliseren het systeem verder wat betreft temporele resolutie, meetsnelheid en signaal-ruisverhouding (SNR). DC-DWS maakt gelijktijdige meting van optische en dynamische eigenschappen in één modaliteit mogelijk, en de time-of-flight (ToF)-onderscheiding helpt verontreiniging in ondiepe lagen te verminderen, waardoor het waardevol is voor CBF-monitoring.

Vanwege de strenge eisen voor temporele en ruimtelijke coherentie verzamelt DC-DWS slechts enkele of enkele speckles, wat resulteert in een beperkte fotonendoorvoer. Bovendien heeft dual-comb interferometrie last van een laag fotonengebruik. Om deze problemen aan te pakken, introduceert Hoofdstuk 3 frequentiegemoduleerde verstrooiingsholografie (FMSH). FMSH maakt gebruik van de lage frequentiemodulatiesnelheid en vervangt enkelvoudige puntdetectoren door een camera, waarbij elke pixel een tijdelijk interferogram vastlegt.. Deze camera-gewijze detectie maakt parallelle acquisitie van DTOF- en Doppler-verbrede DTOF-signalen mogelijk, waardoor zowel statische als dynamische metingen mogelijk zijn. De parallelle aard van de detectie zorgt voor signaal-ruisverhouding (SNR) die vergelijkbaar is met, of beter is dan, fotonentellende detectoren.

In hoofdstuk 4 tonen we aan dat FMSH diepteafhankelijk specklecontrast kan meten door een tijd-frequentiedomein banddoorlaatfilter (BP) toe te passen. Dit filter verwijdert de DC-component van het interferogram en onderdrukt fotonen met een korte ToF-

waarde, waardoor het effectief als een ToF-poort fungeert. Hierdoor verbetert FMSH de specificiteit voor de bloedstroom in diep weefsel.

De combinatie van hoge parallelle detectie en hoge framesnelheid in FMSH leidt echter tot een aanzienlijke datadoorvoer, wat realtime verwerking bemoeilijkt. Om dit probleem aan te pakken, introduceert dit hoofdstuk 5 een vereenvoudigd systeem dat een gemoduleerde distributed-feedback laser combineert met een conventionele CMOS-camera. Snelle modulatie van de laserdiode tijdens de belichtingstijd van de camera maakt selectieve interferentie mogelijk tussen fotonen met specifieke vluchttijden, waardoor diepte-opgeloste heterodyne speckle holografie wordt gegenereerd. Deze aanpak verbetert de gevoeligheid voor stroming in diepere lagen, zelfs bij korte afstanden tussen bron en detector, terwijl de complexiteit van het systeem en het datavolume aanzienlijk worden verminderd.

Tot slot vat hoofdstuk 6 de belangrijkste bevindingen van het proefschrift samen en worden mogelijke richtingen voor toekomstig onderzoek besproken.

1

1

Introduction

In this chapter, we give a overview of background and current status of diffuse optics, with biological tissue in mind. We provide a motivation for using interferometric diffuse optics to determine the optical and dynamic properties of turbid media in this thesis.

1

OPTICAL imaging techniques such as optical coherence tomography[1] (Figure 1.1 (a)) and optical microscopy [2] (Figure 1.1 (b)) have been extensively employed in both clinical diagnostics and fundamental research. However, due to significant absorption and scattering in turbid media, achieving deep-tissue imaging with visible and near-infrared wavelengths remains a substantial challenge. Recent developments—such as measuring the transmission[3] or reflectance matrix of turbid media[4] (Figure 1.1 (d)), employing wavefront shaping[5], and temporarily increasing transparency via dye molecules[6] (Figure 1.1 (e))—have pushed imaging depths to approximately 20 transport mean free paths or more[7]. Nonetheless, reaching centimeter-scale depths in biological tissues remains elusive. Ultrasound imaging[8, 9], while noninvasive, requires skilled operators to achieve optimal results. Photoacoustic imaging (PAI)[10, 11] (Figure 1.1 (c)) has emerged as a hybrid modality that combines optical contrast with ultrasonic resolution, enabling imaging at greater depths than purely optical techniques. However, it requires bulky ultrasound transducers, and is sensitive to acoustic heterogeneities[12]. Short-wavelength electromagnetic radiation, such as that used in X-ray computed tomography (CT)[13] or positron emission tomography (PET)[14], enables deeper imaging but also involves exposure to ionizing radiation[15]. Magnetic resonance imaging (MRI)[16–18] (Figure 1.1 (f)) offers comparable diagnostic information without ionizing radiation but is expensive and generally accessible only in specialized clinical settings.

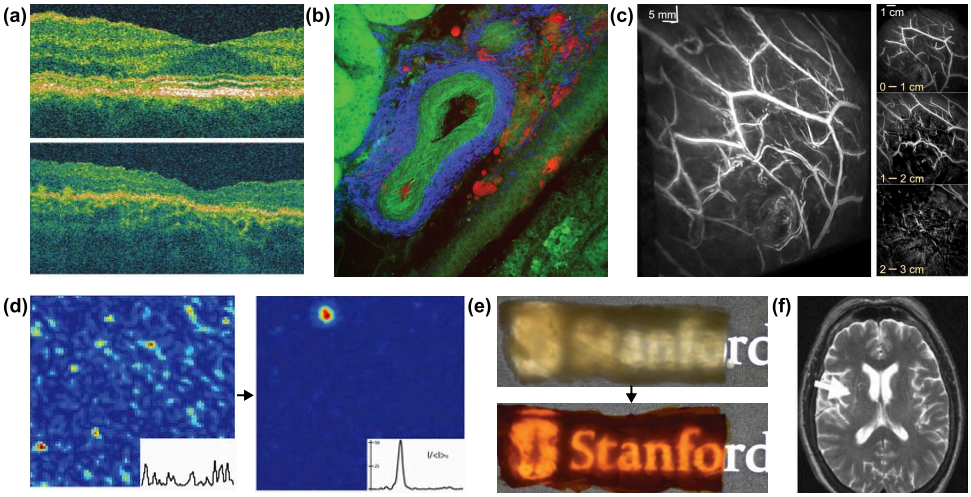

Figure 1.1: Different imaging methods. **(a)** Optical coherence tomography (OCT) of a human retina. Reprinted from [1], with permission from Elsevier. **(b)** Multiple-photon microscopy (MPM) of a blood vessel in kidney tissue. Reprinted from [2], with permission from Springer Nature. **(c)** Photoacoustic computed tomography (PACT) of human breasts. Reprinted from [19], under the CC BY license. **(d)** Measuring the transmission matrix of turbid media enables focusing through it. Reprinted from[3], with permission from Springer Nature. **(e)** Increasing transparency of tissue via dye molecules. Reprinted from [6], with permission from the American Physical Society. **(f)** Magnetic resonance imaging for human brain. Reprinted from [20] under the CC BY license.

Diffuse optical methods exploit the statistical behavior of scattered photons to characterize tissue properties[21–25]. By leveraging the low absorption of tissue in the

near-infrared window[26], this approach offers a promising, low-cost, and noninvasive modality for deep tissue imaging with potential applications in stroke assessment[27, 28], cancer diagnosis[29], and optical brain-computer interface developments[30, 31] (Fig 1.2 (c)-(e)).

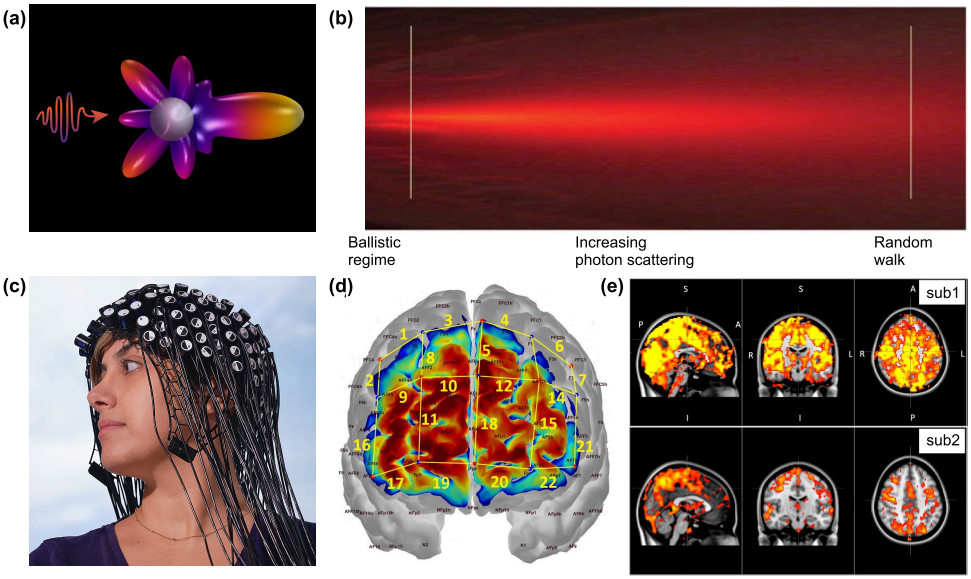

Figure 1.2: From Mie scattering to diffuse optics. **(a)** Mie scattering pattern with a single particle[32]. **(b)** Multiple Mie scattering events happen when light propagates in a turbid media. Reprinted from [33], with permission from Springer Nature. **(c)** Using functional near-infrared spectroscopy (fNIRS) to explore brain activity. Reproduced from [30], under the terms of the CC BY-NC-ND 4.0 license. **(d)** Probe configuration and photon sensitivity profile in fNIRS. Reproduced from [34] under the terms of the CC BY license. **(e)** fNIRS measurement shows high correlation with MRI. Reprinted from [35], with permission from SPIE.

1.1. OPTICAL PROPERTIES OF TURBID MEDIA

Elastic scattering is a fundamental optical phenomenon whereby light (or other electromagnetic waves) interacts with particles without experiencing any shift in wavelength or frequency, thereby conserving the energy of the photons [36]. Rayleigh scattering[37], constitutes a specific regime of elastic scattering in which particles are significantly smaller than the wavelength of the incident light, resulting in an approximately uniform angular distribution of scattered light. Mie scattering, a more general theory, formulated by Gustav Mie [38], pertains to particles with dimensions on the order of, or exceeding, the incident wavelength, which results in pronounced forward-scattering (Figure 1.2(a)) and underpinning the characteristic optical phenomena observed in turbid media (Figure 1.2(b)).

As illustrated in Figure 1.2(b), a small number of scattering events typically, preserves the initial propagation direction of the photons (i.e., ballistic regime); however, with increasing scattering, photons undergo a so-called “random walk”, effectively losing all

vestiges of their initial direction. Quantitatively, the mean free path (MFP) denotes the average distance a photon travels before undergoing a scattering event, while the transport mean free path (TMFP) describes the average distance a photon travels before losing its original direction. The scattering coefficient, μ_s, is defined as the reciprocal of the MFP (i.e., μ_s=1/MFP), and the reduced scattering coefficient, $\mu_s^{'}$, is the reciprocal of the TMFP (i.e.,$\mu_s^{'}$=1/TMFP). In addition to scattering, photons may be absorbed by the medium; the absorption coefficient, μ_a, is defined similarly as the reciprocal of the mean absorption path length. These parameters collectively characterize light propagation in turbid media and are called optical properties, forming the basis for quantitative descriptions of radiative transport.

Due to the strong scattering properties of biological tissue, ballistic photons undergo exponential attenuation, thereby limiting the imaging depth of optical microscopy to the millimeter scale. The identification of a low-absorption spectral window in tissue within the near-infrared (NIR) range (600–950 nm) [26, 39] led to the development of optical techniques capable of probing deep tissue properties at the centimeter scale. This advancement, which emerged in the late 1970s, gave rise to near-infrared spectroscopy (NIRS). In NIRS, light scattering dominates over absorption (i.e., $\mu_s^{'} \gg \mu_a$), allowing the application of the diffusion equation (DE) [40–44] to determine the reduced scattering coefficient ($\mu_s^{'}$) and the absorption coefficient (μ_a), or their relative variations using the modified Beer-Lambert law [45, 46]. This can be further analyzed to infer hemodynamic concentrations or their changes due to different absorption of oxy-hemoglobin and deoxy-hemoglobin.

Table 1.1: The comparison of three different NIRS modalities, adapted from [47].I :Intensity, t:time, T: tissue, φ: phase shift, and DTOF: The photon time-of-flight distribution.

Technique	Source	Detection	Schematic diagram
CW-NIRS	CW laser	Intensity attenuation	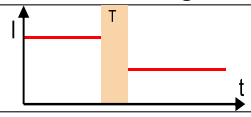
FD-NIRS	Laser with mudolated intensity	Intensity and phase shift	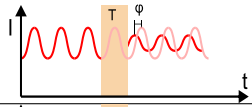
TD-NIRS	Pulsed laser	DTOF	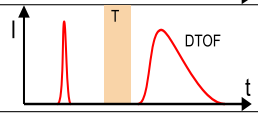

NIRS techniques can be classified into three primary categories based on their light source and detection methods: continuous-wave NIRS (CW-NIRS) [26], frequency-domain NIRS (FD-NIRS) [48], and time-domain NIRS (TD-NIRS) [49, 50]. CW-NIRS employs a continuous-wave laser with constant intensity and measures intensity attenuation to monitor variations in $\mu_s^{'}$ and μ_a. FD-NIRS, by modulating laser intensity, detects phase shifts that encode photon time-of-flight information. In contrast, TD-NIRS utilizes pulsed laser illumination and directly measures photon time-of-flight through

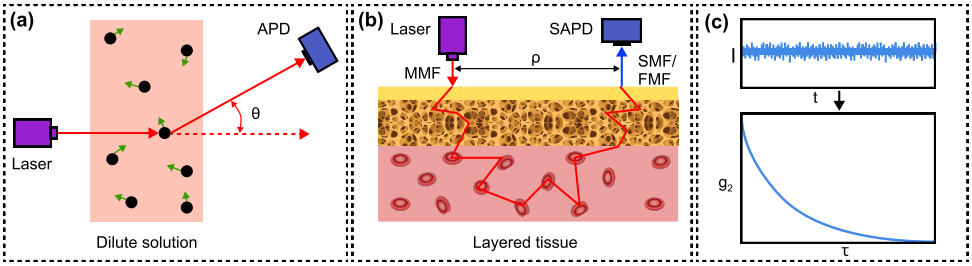

Figure 1.3: Autocorrelation-based dynamic measurements. **(a)** Dynamic light scattering (DLS) measures particle size in dilute solution. **(b)** Dynamic correlation spectroscopy (DCS) measures blood flow in a layered tissue. The multi-mode fiber (MMF) illuminates tissue and back-scattered photons are collected by single-mode fiber (SMF) or few-mode fiber (FMF) with a distance ρ. **(c)** The intensity fluctuations from single photon avalanche diode (SPAD) and its autocorrelation.

temporal correlated single-photon counting (TCSPC) techniques, yielding the distribution of time-of-flight (DTOF), also referred to as the temporal point spread function (TPSF). The DTOF enables the direct retrieval of absolute values for $\mu_s^{'}$ and μ_a by solving the DE under various geometries and boundary conditions [42–44].

1.2. DYNAMIC PROPERTIES OF TURBID MEDIA

In human tissue, blood flow serves as a critical physiological biomarker, playing a vital role in oxygen and nutrient delivery, metabolic regulation, and tissue health. Impairments in blood flow are associated with various pathological conditions, including stroke, cardiovascular diseases, and neurodegenerative disorders. While changes in optical absorption can indirectly reflect scatter dynamics, this approach lacks efficiency and sensitivity in detecting blood flow variations [51]. Several complementary optical techniques based on intensity autocorrelation[24], speckle contrast[52], or Doppler spectrum [53]that have been developed to assess blood dynamics directly.

1.2.1. DIFFUSE CORRELATION SPECTROSCOPY (DCS)

Dynamic light scattering (DLS), first developed in the 1960s [54], is employed to measure the diffusion coefficient of particles undergoing Brownian motion in dilute solutions (Figure 1.3(a)). This coefficient can subsequently be used to determine particle size [55, 56]. In its classical form, DLS assumes that photons undergo only single scattering. The technique was later extended to account for multiple scattering, giving rise to diffusing-wave spectroscopy (DWS) [57].

Building upon these developments, subsequent work applied the correlation transport equation (CTE) [58, 59] to formalize the analysis of scattered light for the quantification of blood flow in biological tissues, using either transmission or reflectance geometries. This led to the establishment of diffuse correlation spectroscopy (DCS) [24].

In DCS (Figure 1.3(b)), coherent light is used to illuminate tissue, where multiple scattering events give rise to a dynamic interference pattern known as a speckle[60]. The motion of red blood cells (RBCs) within the tissue induces temporal phase shifts, resulting in speckle fluctuations (Figure 1.3(c)). A single-mode (or few-mode) optical fiber is

positioned at a source-detector separation ρ to collect one or a few speckles. Empirically, the average penetration depth is approximately $\rho/2$[22, 61]. The temporal fluctuations in the detected speckle intensity are quantified by calculating the normalized intensity autocorrelation function, using either hardware or software-based correlators:

$$g_2(\tau) = \frac{< I(t)I(t+\tau) >}{< I^2(t) >} \tag{1.1}$$

By Siegert relation, the intensity autocorrelation is related to field autocorrelation:

$$g_2(\tau) = 1 + \beta g_1^2(\tau) \tag{1.2}$$

The parameter β, known as the coherence factor, accounts for both the temporal and spatial coherence properties of the illumination—specifically, the coherence length of the source and the number of speckles collected. $g_2(\tau)$ is the intensity autocorrelation function, I represents the intensity and $g_1(\tau)$ is the field autocorrelation function, which correlates the electric field of the light. Employing a laser source with a long coherence length and limiting the number of detected speckles enhances the signal-to-noise ratio (SNR) of dynamic signal. Specifically, $g_1(\tau) = G_1(\tau)/G_1(0) = < \mathbf{E}(t)\mathbf{E}^*(t+\tau) > / < \mathbf{E}(t)\mathbf{E}^*(t) >$ is the normalized electric field autocorrelation function, and can be derived by solving CTE under various geometrical configurations. For a semi-infinite medium[22]:

$$G_1(\tau) = \frac{3\mu_s^{'}}{4\pi}[\frac{\exp(Kr_1)}{r_1} - \frac{\exp(Kr_2)}{r_2}] \tag{1.3}$$

where $K(\tau) = \sqrt{3\mu_a\mu_s^{'} + \mu_s^{'}k_0^2 6\alpha D_B\tau}$, $r_1 = (\rho^2 + z_o^2)^{1/2}$, $r_2 = [\rho^2 + (z_o + 2z_b)^2]^{1/2}$, $k_0 = 2\pi/\lambda$, $z_o = 1/\mu_s^{'}$, and $z_b = 1.76/\mu_s^{'}$ given an index of refraction for tissue of 1.37[43]. The parameter αD_B, commonly referred to as the blood flow index (BFi), serves as a quantitative measure of tissue perfusion. Here, D_B represents the effective Brownian diffusion coefficient of the moving scatterers, primarily RBCs. The term α denotes the tissue blood volume fraction and accounts for the proportion of scattering events arising specifically from dynamic scatterers. In this thesis, we use the general term DCS to refer to this group of technologies, except in Chapter 3, to avoid confusion between dual-comb spectroscopy and diffuse correlation spectroscopy.

1.2.2. LASER DOPPLER FLOWMETRY (LDF)

Laser Doppler flowmetry (LDF) was developed before DCS as a technique for assessing microvascular blood flow. In a typical LDF setup, the detected signal is acquired using photodetectors such as an avalanche photodiode (APD), photomultiplier tube (PMT), or single-photon avalanche diode (SPAD)[62]. The resulting signal is then processed using a Fourier transform, and its statistical moments are computed via dedicated hardware.

In its simplest theoretical formulation, LDF assumes a single-scattering regime, where each detected photon interacts with a moving scatterer—typically a red blood cell—only once before exiting the tissue. However, in biological tissues, particularly at greater depths, multiple scattering dominates. In these cases, photons undergo numerous scattering events before reaching the detector, and the observed Doppler shift

results from the cumulative motion effects across these interactions. This phenomenon causes a broadening of the Doppler power spectrum (DPS) and a loss of directional information[63].

Several approaches have been developed to extract blood flow information from the DPS. For example, fitting the logarithm of the DPS [64] or calculating the first and zeroth moments of the spectrum [65] can yield estimates of tissue perfusion. While LDF and DCS share similar instrumentation, they differ fundamentally in their analytical frameworks. The Wiener–Khinchin theorem establishes a theoretical connection between them, as the DPS and the autocorrelation function are Fourier transform pairs. Recent comparative studies have further explored this relationship [66].

1.2.3. SPECKLE CONTRAST OPTICAL SPECTROSCOPY (SCOS)

In contrast to techniques that analyze the intensity autocorrelation function or DPS of single or few speckles, flow dynamics can also be characterized using the temporal or spatial contrast of a speckle pattern formed by multiple speckles. Laser speckle contrast imaging (LSCI, Figure 1.4(a))[52] is a full-field, wide-area imaging technique employed to visualize blood flow in tissue. As in DCS, coherent light scattered by moving particles (such as RBCs) produces a dynamic speckle pattern (Figure 1.4(b)). This pattern is recorded by a camera, and the spatial speckle contrast is computed as:

$$K = \frac{\sigma}{< I >} \tag{1.4}$$

where K denotes the speckle contrast, σ is the standard deviation of the intensity in a local region, $< I >$ is the mean intensity in the same region.

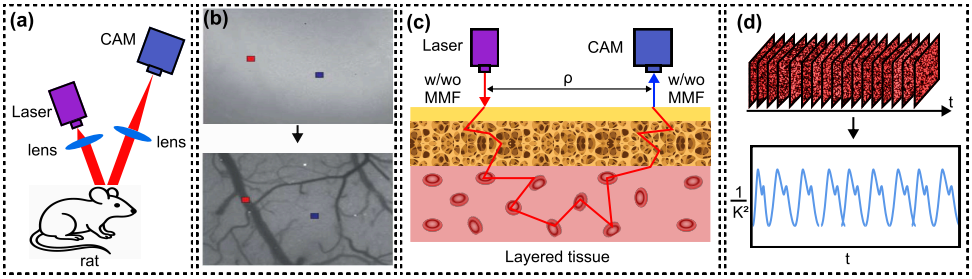

Figure 1.4: speckle-contrast-based dynamic measurements. **(a)** Typical laser speckle contrast imaging (LSCI) is used to visualize blood flow in the rat brain. **(b)** The speckle pattern captured by the camera (CAM) reveals the shape of blood vessels through its contrast. Reprinted from [67], with permission from SAGE Publications. **(c)** Speckle contrast optical spectroscopy (SCOS) is used to measure blood flow in deep tissue. **(d)** The ensemble speckle contrast can be used to extract heart rate.

LSCI primarily captures single-scattered photons and is thus most effective for imaging superficial blood flow. To probe deeper tissue layers, speckle contrast optical spectroscopy (SCOS)[68–71] employs a large source-detector separation (ρ) to collect photons that have traveled through deeper regions (Figure 1.4(c)). The full speckle pattern is then analyzed to compute the contrast (Figure 1.4(d)), from which changes in blood flow can be inferred (Figure 1.4(d)) by evaluating the time dependent behaviour.

1

1.3. THE STATE OF THE ART

Cerebral blood flow (CBF) is a clinically critical parameter, essential for assessing brain function and pathology. Measuring blood flow beneath the scalp and skull remains challenging, and DCS is currently limited by SNR and accuracy. Specifically, the decay rate of the electric field autocorrelation function depends on both the reduced scattering coefficient μ_s' and the effective diffusion coefficient of RBCs, D_B (as shown in equation 1.2). Since μ_s' varies significantly across individuals and tissue types, assuming a fixed value for μ_s' can introduce substantial errors in the estimation of blood flow.

To address this limitation, DCS has been integrated with NIRS, enabling simultaneous measurement of optical properties and dynamics. Time-domain DCS (TD-DCS)[72–74] represents the first effort to combine time-domain NIRS (TD-NIRS) and DCS into a unified modality, allowing for concurrent acquisition of DTOF and time-of-flight–dependent dynamics.

Interferometric near-infrared spectroscopy (iNIRS)[75–79] extends swept-source optical coherence tomography (SS-OCT) from the ballistic to the diffusive regime. By separating the source and detector collimators, iNIRS selectively collects diffusely scattered photons and measures DTOF. Additionally, it employs high-speed wavelength sweeping to obtain time-of-flight–resolved field autocorrelations. However, both TD-DCS and iNIRS suffer from low photon throughput due to the use of single-mode fiber (SMF) detection, thereby limiting their SNR for measuring CBF in adult subjects.

Recent advancements in single-photon detection technologies—such as single-photon avalanche diode (SPAD) arrays[80–82] and superconducting nanowire single-photon detectors (SNSPDs)[83–85]—have significantly improved SNR and enabled successful CBF measurements for source-detector separations $\geqslant 3$ cm.

Alternatively, interferometric diffusing-wave spectroscopy (iDWS)[86–88] employs multimode fiber (MMF) to collect multiple speckles and uses a high-speed CMOS camera to resolve them spatially, enabling CBF measurements at source-detector separations up to 3.5 cm. Studies have demonstrated that iDWS can achieve SNR comparable to or even exceeding that of SNSPD-based systems[89], while offering lower cost and greater robustness to ambient light. Interferometric speckle visibility spectroscopy (iSVS)[90, 91], in contrast, uses low-frame-rate cameras to detect heterodyne speckle contrast for assessing dynamic scattering. Despite their advantages, both iDWS and iSVS face challenges in quantifying μ_s'. While iSVS lacks this functionality entirely, iDWS necessitates a variable ToF gate—a requirement that adds system-level complexity.

1.4. THE AIM OF THIS THESIS

To enable the development of next-generation portable, and potentially wearable, diffuse optical systems for continuous CBF monitoring, this dissertation adopts the interferometric route. Compared to photon-counting detectors, interferometric systems offer key advantages including insensitivity to ambient light and significantly lower cost. This thesis proposes several technical innovations to advance the state of the art:

1. Dual-comb diffusing-wave Spectroscopy (DC-DWS): To improve the accuracy and depth specificity of flow measurements, a hybrid modality integrating time-domain near-infrared spectroscopy (TD-NIRS) and diffusing-wave spectroscopy (DWS) is devel-

oped using a single-cavity dual-comb laser.

2. Frequency-modulated scattering holography (FMSH): To address the low signal-to-noise ratio (SNR) challenges inherent in DC-DWS and interferometric NIRS (iNIRS), a novel technique termed frequency-modulated scattering holography is introduced. FMSH measures the DTOF of static sample and Doppler-broadened DTOF (DB-DTOF) of dynamic sample. The DB-DTOF is subsequently used to determine the ToF-gated speckle contrast.

3. Coherence-gated interferometric speckle visibility spectroscopy (CG-iSVS): To reduce system complexity, cost and data throughput while maintaining sensitivity to flow dynamics, a coherence-gated version of interferometric speckle visibility spectroscopy is proposed.

Table 1.2: Summary of techniques proposed in this thesis. DC-DWS: dual-comb diffusing-wave specrtroscopy, FMSH: freqency-modulated scattering holography, CG-iSVS: coherence-gated interferometric speckle visibility spectroscopy, BD: balanced detector, CMOS: complementary metal-oxide-semiconductor, K: speckle contrast, S: specificity to deep flow, BFI: blood flow index.

Technique	Source	Detector	Advantages	Disadvantages
DC-DWS	Dual-comb laser	BD	Measures $\mu_s^{'}$, μ_a and BFI, high S	Low SNR
FMSH	Swept-source laser	Fast CMOS	Measures $\mu_s^{'}$, μ_a, high S and SNR	High data throughput, no absolute BFI
CG-iSVS	Swept-source laser	Normal CMOS	high S and SNR, low-cost	No $\mu_s^{'}$,μ_a and absolute BFI

1.5. THE FRAMEWORK OF THIS THESIS

In this thesis, we explore various methodologies for advancing interferometric diffuse optics (iDO).

Chapter 2 presents a novel approach that extends coherent light detection and ranging (Co-LiDAR) techniques to iDO. Specifically, we adapt dual-comb LiDAR to develop a dual-comb diffusing-wave spectroscopy (DC-DWS) system. By leveraging heterodyne gain and electro-optic sampling (EOS), the DC-DWS system enables simultaneous measurement of the DTOF and time-of-flight–dependent dynamics. We analyze and optimize the SNR of this system and validate its performance in tissue-mimicking phantoms. Despite its advantages, the dual-comb system suffers from a low duty cycle, which limits its SNR and hinders in vivo application.

In Chapter 3, we conduct a comparative analysis of the SNR performance among dual-comb LiDAR, frequency-modulated continuous-wave (FMCW) LiDAR, and SPAD-based LiDAR. Building on this comparison, we introduce a novel technique—frequency-modulated scattering holography (FMSH)—which enables measurement of Doppler-broadened DTOF with SNR comparable to, or even exceeding, that of SPAD-based systems when paired with an optimized camera.

In Chapter 4, we investigate the time-of-flight–dependent speckle contrast in FMSH by applying a high-pass filter in the frequency domain. This approach enhances the specificity of speckle contrast measurements to deeper blood flow. The technique is experimentally validated using a tissue-mimicking phantom.

The high-pass filter in FMSH effectively acts as a coherence gate. Based on this insight, Chapter 5 introduces a low-cost implementation of coherence-gated interferometric speckle visibility spectroscopy (CG-iSVS). This system employs a wavelength-modulated distributed-feedback laser as the light source and a standard camera as the detector. By adjusting the optical path length difference between the sample and reference arms, it enables depth-resolved measurement of heterodyne speckle contrast. This method is validated in both tissue-mimicking phantoms and human subjects.

Finally, Chapter 6 provides a summary and conclusion of the thesis, along with a forward-looking discussion on the future directions and potential impact of iDO.

BIBLIOGRAPHY

[1] W. Drexler and J. G. Fujimoto, "State-of-the-art retinal optical coherence tomography", Progress in retinal and eye research **27**, 45–88 (2008).

[2] E. E. Hoover and J. A. Squier, "Advances in multiphoton microscopy technology", Nature photonics **7**, 93–101 (2013).

[3] S. M. Popoff, G. Lerosey, R. Carminati, M. Fink, A. C. Boccara, and S. Gigan, "Measuring the transmission matrix in optics: an approach to the study and control of light propagation in disordered media", Physical review letters **104**, 100601 (2010).

[4] W. Lambert, L. A. Cobus, M. Couade, M. Fink, and A. Aubry, "Reflection matrix approach for quantitative imaging of scattering media", Physical Review X **10**, 021048 (2020).

[5] H. Cao, A. P. Mosk, and S. Rotter, "Shaping the propagation of light in complex media", Nature Physics **18**, 994–1007 (2022).

[6] Z. Ou, Y.-S. Duh, N. J. Rommelfanger, C. H. Keck, S. Jiang, K. Brinson Jr, S. Zhao, E. L. Schmidt, X. Wu, F. Yang, et al., "Achieving optical transparency in live animals with absorbing molecules", Science **385**, eadm6869 (2024).

[7] S. Yoon, M. Kim, M. Jang, Y. Choi, W. Choi, S. Kang, and W. Choi, "Deep optical imaging within complex scattering media", Nature Reviews Physics **2**, 141–158 (2020).

[8] T. L. Szabo, *Diagnostic ultrasound imaging: inside out* (Academic press, 2013).

[9] K. Nightingale, "Acoustic radiation force impulse (arfi) imaging: a review", Current medical imaging reviews **7**, 328–339 (2011).

[10] M. Xu and L. V. Wang, "Photoacoustic imaging in biomedicine", Review of scientific instruments **77** (2006).

[11] L. V. Wang and S. Hu, "Photoacoustic tomography: in vivo imaging from organelles to organs", science **335**, 1458–1462 (2012).

[12] L. Wang, *Photoacoustic imaging and spectroscopy* (CRC press, 2017).

[13] W. A. Kalender, "X-ray computed tomography", Physics in medicine & Biology **51**, R29 (2006).

[14] M. E. Phelps, "Pet: the merging of biology and imaging into molecular imaging", Journal of Nuclear Medicine **41**, 661–681 (2000).

[15] S. R. Cherry, J. A. Sorenson, and M. E. Phelps, *Physics in nuclear medicine* (Saunders, 2013).

[16] P. C. Lauterbur, "Image formation by induced local interactions: examples employing nuclear magnetic resonance", nature **242**, 190–191 (1973).

[17] K. P. Pruessmann, M. Weiger, M. B. Scheidegger, and P. Boesiger, "Sense: sensitivity encoding for fast mri", Magnetic Resonance in Medicine: An Official Journal of the International Society for Magnetic Resonance in Medicine **42**, 952–962 (1999).

[18] D. J. Larkman and R. G. Nunes, "Parallel magnetic resonance imaging", Physics in Medicine & Biology **52**, R15 (2007).

[19] L. Lin, P. Hu, X. Tong, S. Na, R. Cao, X. Yuan, D. C. Garrett, J. Shi, K. Maslov, and L. V. Wang, "High-speed three-dimensional photoacoustic computed tomography for preclinical research and clinical translation", Nature communications **12**, 882 (2021).

[20] B. Heim, F. Krismer, R. De Marzi, and K. Seppi, "Magnetic resonance imaging for the diagnosis of parkinson's disease", Journal of neural transmission **124**, 915–964 (2017).

[21] G. Strangman, D. A. Boas, and J. P. Sutton, "Non-invasive neuroimaging using near-infrared light", Biological psychiatry **52**, 679–693 (2002).

[22] T. Durduran, R. Choe, W. B. Baker, and A. G. Yodh, "Diffuse optics for tissue monitoring and tomography", Reports on progress in physics **73**, 076701 (2010).

[23] D. A. Boas, D. H. Brooks, E. L. Miller, C. A. DiMarzio, M. Kilmer, R. J. Gaudette, and Q. Zhang, "Imaging the body with diffuse optical tomography", IEEE signal processing magazine **18**, 57–75 (2001).

[24] T. Durduran and A. G. Yodh, "Diffuse correlation spectroscopy for non-invasive, micro-vascular cerebral blood flow measurement", Neuroimage **85**, 51–63 (2014).

[25] H. Ayaz, W. B. Baker, G. Blaney, D. A. Boas, H. Bortfeld, K. Brady, J. Brake, S. Brigadoi, E. M. Buckley, S. A. Carp, et al., "Optical imaging and spectroscopy for the study of the human brain: status report", Neurophotonics **9**, S24001 (2022).

[26] F. F. Jöbsis, "Noninvasive, infrared monitoring of cerebral and myocardial oxygen sufficiency and circulatory parameters", Science **198**, 1264–1267 (1977).

[27] K. M. Brady, J. K. Lee, K. K. Kibler, P. Smielewski, M. Czosnyka, R. B. Easley, R. C. Koehler, and D. H. Shaffner, "Continuous time-domain analysis of cerebrovascular autoregulation using near-infrared spectroscopy", Stroke **38**, 2818–2825 (2007).

[28] K.-C. Wu, J. Sunwoo, F. Sheriff, P. Farzam, P. Y. Farzam, F. Orihuela-Espina, S. L. LaRose, A. D. Monk, M. A. Aziz-Sultan, N. Patel, et al., "Validation of diffuse correlation spectroscopy measures of critical closing pressure against transcranial doppler ultrasound in stroke patients", Journal of biomedical optics **26**, 036008–036008 (2021).

[29] V. R. Kondepati, H. M. Heise, and J. Backhaus, "Recent applications of near-infrared spectroscopy in cancer diagnosis and therapy", Analytical and bioanalytical chemistry **390**, 125–139 (2008).

[30] J. Sakai, "Functional near-infrared spectroscopy reveals brain activity on the move", Proceedings of the National Academy of Sciences **119**, e2208729119 (2022).

[31] H. Y. Ban, G. M. Barrett, A. Borisevich, A. Chaturvedi, J. L. Dahle, H. Dehghani, J. Dubois, R. M. Field, V. Gopalakrishnan, A. Gundran, et al., "Kernel flow: a high channel count scalable time-domain functional near-infrared spectroscopy system", Journal of biomedical optics **27**, 074710 (2022).

[32] Wikipedia contributors, *Mie scattering*, https://en.wikipedia.org/wiki/Mie_scattering, 2025.

[33] V. Ntziachristos, "Going deeper than microscopy: the optical imaging frontier in biology", Nature methods **7**, 603–614 (2010).

[34]M. C. Mutlu, S. B. Erdoğan, O. C. Öztürk, R. Canbeyli, and H. Saybaşılı, "Functional near-infrared spectroscopy indicates that asymmetric right hemispheric activation in mental rotation of a jigsaw puzzle decreases with task difficulty", Frontiers in Human Neuroscience **14**, 252 (2020).

[35]Y. Tong, L. M. Hocke, S. C. Licata, and B. deB. Frederick, "Low-frequency oscillations measured in the periphery with near-infrared spectroscopy are strongly correlated with blood oxygen level-dependent functional magnetic resonance imaging signals", Journal of biomedical optics **17**, 106004–106004 (2012).

[36]M. Born and E. Wolf, *Principles of optics: electromagnetic theory of propagation, interference and diffraction of light* (Elsevier, 2013).

[37]L. Rayleigh, "X. on the electromagnetic theory of light", The London, Edinburgh, and Dublin Philosophical Magazine and Journal of Science **12**, 81–101 (1881).

[38]G. Mie, "Beiträge zur optik trüber medien, speziell kolloidaler metallösungen", Annalen der physik **330**, 377–445 (1908).

[39]F. F. Jobsis-vander Vliet, "Discovery of the near-infrared window into the body and the early development of near-infrared spectroscopy", Journal of biomedical optics **4**, 392–396 (1999).

[40]A. Ishimaru, "Diffusion of a pulse in densely distributed scatterers", Journal of the Optical Society of America **68**, 1045–1050 (1978).

[41]K. Furutsu, "Diffusion equation derived from space-time transport equation", Journal of the Optical Society of America **70**, 360–366 (1980).

[42]M. S. Patterson, B. Chance, and B. C. Wilson, "Time resolved reflectance and transmittance for the noninvasive measurement of tissue optical properties", Applied optics **28**, 2331–2336 (1989).

[43]R. C. Haskell, L. O. Svaasand, T.-T. Tsay, T.-C. Feng, M. S. McAdams, and B. J. Tromberg, "Boundary conditions for the diffusion equation in radiative transfer", Journal of the Optical Society of America A **11**, 2727–2741 (1994).

[44]D. Contini, F. Martelli, and G. Zaccanti, "Photon migration through a turbid slab described by a model based on diffusion approximation. i. theory", Applied optics **36**, 4587–4599 (1997).

[45]D. T. Delpy, M. Cope, P. van der Zee, S. Arridge, S. Wray, and J. Wyatt, "Estimation of optical pathlength through tissue from direct time of flight measurement", Physics in Medicine & Biology **33**, 1433 (1988).

[46]A. Sassaroli and S. Fantini, "Comment on the modified beer–lambert law for scattering media", Physics in Medicine & Biology **49**, N255 (2004).

[47]F. Scholkmann, S. Kleiser, A. J. Metz, R. Zimmermann, J. M. Pavia, U. Wolf, and M. Wolf, "A review on continuous wave functional near-infrared spectroscopy and imaging instrumentation and methodology", Neuroimage **85**, 6–27 (2014).

[48]B. Chance, E. Anday, S. Nioka, S. Zhou, L. Hong, K. Worden, C. Li, T. Murray, Y. Ovetsky, D. Pidikiti, et al., "A novel method for fast imaging of brain function, non-invasively, with light", Optics express **2**, 411–423 (1998).

[49]Y. Kuga, A. Ishimaru, and A. P. Bruckner, "Experiments on picosecond pulse propagation in a diffuse medium", Journal of the Optical Society of America **73**, 1812–1815 (1983).

[50]R. Cubeddu, A. Pifferi, P. Taroni, A. Torricelli, and G. Valentini, "Experimental test of theoretical models for time-resolved reflectance", Medical physics **23**, 1625–1633 (1996).

[51]J. Selb, D. A. Boas, S.-T. Chan, K. C. Evans, E. M. Buckley, and S. A. Carp, "Sensitivity of near-infrared spectroscopy and diffuse correlation spectroscopy to brain hemodynamics: simulations and experimental findings during hypercapnia", Neurophotonics **1**, 015005–015005 (2014).

[52]D. A. Boas and A. K. Dunn, "Laser speckle contrast imaging in biomedical optics", Journal of biomedical optics **15**, 011109–011109 (2010).

[53]L. E. Drain, "The laser doppler techniques", Chichester (1980).

[54]R. d. Pecora, "Doppler shifts in light scattering from pure liquids and polymer solutions", The Journal of Chemical Physics **40**, 1604–1614 (1964).

[55]F. Hallett, J. Watton, and P. Krygsman, "Vesicle sizing: number distributions by dynamic light scattering", Biophysical journal **59**, 357–362 (1991).

[56]F. R. Hallett, "Particle size analysis by dynamic light scattering", Food research international **27**, 195–198 (1994).

[57]D. Weitz, J. Zhu, D. Durian, H. Gang, and D. Pine, "Diffusing-wave spectroscopy: the technique and some applications", Physica Scripta **1993**, 610 (1993).

[58]D. A. Boas, L. Campbell, and A. G. Yodh, "Scattering and imaging with diffusing temporal field correlations", Physical review letters **75**, 1855 (1995).

[59]D. A. Boas and A. G. Yodh, "Spatially varying dynamical properties of turbid media probed with diffusing temporal light correlation", Journal of the Optical Society of America A **14**, 192–215 (1997).

[60]J. W. Goodman, *Speckle phenomena in optics: theory and applications* (Roberts and Company Publishers, 2007).

[61]M. S. Patterson, S. Andersson-Engels, B. C. Wilson, and E. K. Osei, "Absorption spectroscopy in tissue-simulating materials: a theoretical and experimental study of photon paths", Applied optics **34**, 22–30 (1995).

[62]T. Binzoni, D. Van De Ville, and B. Sanguinetti, "Time-domain algorithm for single-photon laser-doppler flowmetry at large interoptode spacing in human bone", Applied Optics **53**, 7017–7024 (2014).

[63]M. D. Stern, "Laser doppler velocimetry in blood and multiply scattering fluids: theory", Applied optics **24**, 1968–1986 (1985).

[64]R. Lohwasser and G. Soelkner, "Experimental and theoretical laser-doppler frequency spectra of a tissuelike model of a human head with capillaries", Applied optics **38**, 2128–2137 (1999).

[65]A. Humeau, W. Steenbergen, H. Nilsson, and T. Strömberg, "Laser doppler perfusion monitoring and imaging: novel approaches", Medical & biological engineering & computing **45**, 421–435 (2007).

[66]T. Binzoni and F. Martelli, "Study on the mathematical relationship existing between single-photon laser-doppler flowmetry and diffuse correlation spectroscopy with static background", Journal of the Optical Society of America A **34**, 2096–2101 (2017).

[67]S. S. Kazmi, L. M. Richards, C. J. Schrandt, M. A. Davis, and A. K. Dunn, "Expanding applications, accuracy, and interpretation of laser speckle contrast imaging of cerebral blood flow", Journal of Cerebral Blood Flow & Metabolism **35**, 1076–1084 (2015).

[68]C. P. Valdes, H. M. Varma, A. K. Kristoffersen, T. Dragojevic, J. P. Culver, and T. Durduran, "Speckle contrast optical spectroscopy, a non-invasive, diffuse optical method for measuring microvascular blood flow in tissue", Biomedical optics express **5**, 2769–2784 (2014).

[69]R. Bandyopadhyay, A. Gittings, S. Suh, P. Dixon, and D. J. Durian, "Speckle-visibility spectroscopy: a tool to study time-varying dynamics", Review of scientific instruments **76** (2005).

[70]B. Kim, S. Zilpelwar, E. J. Sie, F. Marsili, B. Zimmermann, D. A. Boas, and X. Cheng, "Measuring human cerebral blood flow and brain function with fiber-based speckle contrast optical spectroscopy system", Communications Biology **6**, 844 (2023).

[71]S. Mahler, Y. X. Huang, M. Ismagilov, D. Álvarez-Chou, A. Abedi, J. M. Tyszka, Y. T. Lo, J. Russin, R. L. Pantera, C. Liu, et al., "Portable six-channel laser speckle system for simultaneous measurement of cerebral blood flow and volume with potential applications in characterization of brain injury", Neurophotonics **12**, 015003–015003 (2025).

[72]J. Sutin, B. Zimmerman, D. Tyulmankov, D. Tamborini, K. C. Wu, J. Selb, A. Gulinatti, I. Rech, A. Tosi, D. A. Boas, et al., "Time-domain diffuse correlation spectroscopy", Optica **3**, 1006–1013 (2016).

[73]M. Pagliazzi, S. K. V. Sekar, L. Colombo, E. Martinenghi, J. Minnema, R. Erdmann, D. Contini, A. D. Mora, A. Torricelli, A. Pifferi, et al., "Time domain diffuse correlation spectroscopy with a high coherence pulsed source: in vivo and phantom results", Biomedical optics express **8**, 5311–5325 (2017).

[74]D. Mazumder, M. M. Wu, N. Ozana, D. Tamborini, M. A. Franceschini, and S. A. Carp, "Optimization of time domain diffuse correlation spectroscopy parameters for measuring brain blood flow", Neurophotonics **8**, 035005–035005 (2021).

[75]L. Mei, S. Svanberg, and G. Somesfalean, "Frequency-modulated light scattering in colloidal suspensions", Applied Physics Letters **102** (2013).

[76]L. Mei, G. Somesfalean, and S. Svanberg, "Frequency-modulated light scattering interferometry employed for optical properties and dynamics studies of turbid media", Biomedical Optics Express **5**, 2810–2822 (2014).

[77]D. Borycki, O. Kholiqov, S. P. Chong, and V. J. Srinivasan, "Interferometric near-infrared spectroscopy (inirs) for determination of optical and dynamical properties of turbid media", Optics express **24**, 329–354 (2016).

[78] O. Kholiqov, D. Borycki, and V. J. Srinivasan, "Interferometric near-infrared spectroscopy (inirs): performance tradeoffs and optimization", Optics express **25**, 28567–28589 (2017).

[79] O. Kholiqov, W. Zhou, T. Zhang, V. Du Le, and V. J. Srinivasan, "Time-of-flight resolved light field fluctuations reveal deep human tissue physiology", Nature communications **11**, 391 (2020).

[80] E. J. Sie, H. Chen, E.-F. Saung, R. Catoen, T. Tiecke, M. A. Chevillet, and F. Marsili, "High-sensitivity multispeckle diffuse correlation spectroscopy", Neurophotonics **7**, 035010–035010 (2020).

[81] W. Liu, R. Qian, S. Xu, P. Chandra Konda, J. Jönsson, M. Harfouche, D. Borycki, C. Cooke, E. Berrocal, Q. Dai, et al., "Fast and sensitive diffuse correlation spectroscopy with highly parallelized single photon detection", APL Photonics **6** (2021).

[82] M. A. Wayne, E. J. Sie, A. C. Ulku, P. Mos, A. Ardelean, F. Marsili, C. Bruschini, and E. Charbon, "Massively parallel, real-time multispeckle diffuse correlation spectroscopy using a 500× 500 spad camera", Biomedical Optics Express **14**, 703–713 (2023).

[83] N. Ozana, A. I. Zavriyev, D. Mazumder, M. Robinson, K. Kaya, M. Blackwell, S. A. Carp, and M. A. Franceschini, "Superconducting nanowire single-photon sensing of cerebral blood flow", Neurophotonics **8**, 035006–035006 (2021).

[84] C.-S. Poon, D. S. Langri, B. Rinehart, T. M. Rambo, A. J. Miller, B. Foreman, and U. Sunar, "First-in-clinical application of a time-gated diffuse correlation spectroscopy system at 1064 nm using superconducting nanowire single photon detectors in a neuro intensive care unit", Biomedical Optics Express **13**, 1344–1356 (2022).

[85] V. Parfentyeva, L. Colombo, P. Lanka, M. Pagliazzi, A. Brodu, N. Noordzij, M. Kolarczik, A. Dalla Mora, R. Re, D. Contini, et al., "Fast time-domain diffuse correlation spectroscopy with superconducting nanowire single-photon detector: system validation and in vivo results", Scientific Reports **13**, 11982 (2023).

[86] W. Zhou, O. Kholiqov, S. P. Chong, and V. J. Srinivasan, "Highly parallel, interferometric diffusing wave spectroscopy for monitoring cerebral blood flow dynamics", Optica **5**, 518–527 (2018).

[87] W. Zhou, O. Kholiqov, J. Zhu, M. Zhao, L. L. Zimmermann, R. M. Martin, B. G. Lyeth, and V. J. Srinivasan, "Functional interferometric diffusing wave spectroscopy of the human brain", Science Advances **7**, eabe0150 (2021).

[88] M. Zhao, W. Zhou, S. Aparanji, D. Mazumder, and V. J. Srinivasan, "Interferometric diffusing wave spectroscopy imaging with an electronically variable time-of-flight filter", Optica **10**, 42–52 (2023).

[89] M. B. Robinson, M. Renna, N. Ozana, A. N. Martin, N. Otic, S. A. Carp, and M. A. Franceschini, "Portable, high speed blood flow measurements enabled by long wavelength, interferometric diffuse correlation spectroscopy (lw-idcs)", Scientific Reports **13**, 8803 (2023).

[90] J. Xu, A. K. Jahromi, J. Brake, J. E. Robinson, and C. Yang, "Interferometric speckle visibility spectroscopy (isvs) for human cerebral blood flow monitoring", Apl Photonics **5** (2020).

[91] J. Xu, A. K. Jahromi, and C. Yang, "Diffusing wave spectroscopy: a unified treatment on temporal sampling and speckle ensemble methods", Apl Photonics **6** (2021).

2

2

DUAL-COMB DIFFUSING-WAVE SPECTROSCOPY

In measuring cerebral blood flow non-invasively using optical techniques diffusing-wave spectroscopy (DWS) is often combined with near-infrared spectroscopy (NIRS) to obtain a reliable blood flow index. Measuring blood flow index at a determined depth with high specificity remains the ultimate goal. In this study, we present a simple approach using dual-comb lasers where we simultaneously measure the absorption coefficient (μ_a), the reduced scattering coefficient (μ_s'), and dynamic properties. This system can also effectively differentiate dynamics from various depths which is crucial for analyzing multi-layer dynamics. For cerebral blood flow measurements, this capability is particularly valuable as it helps to mitigate the influence of the scalp and skull, thereby enhancing the specificity of deep tissue.

Parts of this chapter have been published in *ACS Photonics* **11(10)**, 3972-3981 (2024).

2.1. INTRODUCTION

Cerebral blood flow (CBF) serves as a pivotal biomarker in the diagnosis of ischemic stroke[1, 2]. Although computed tomography (CT)[3, 4] and magnetic resonance imaging (MRI)[5, 6] are the gold standards for imaging-based diagnosis, they are hindered by disadvantages such as radiation exposure, high financial costs, and the necessity for patient transportation to medical facilities, thereby reducing valuable time for intervention.

Optical techniques to study human physiology have centered around acquiring insights into the propagation of light in diffuse media[7]. Promising techniques have emerged like near-infrared spectroscopy (NIRS), which leverages the low absorption of tissue in the NIR window to yield reduced scattering coefficients μ_s' and absorption coefficients μ_a by pulsed source (time domain NIRS, TD-NIRS)[8] or modulated source (frequency domain NIRS, FD-NIRS) [9], optical coherence tomography (OCT), which is an interferometric imaging technique[10], and diffusing wave spectroscopy (DWS, also called diffuse correlation spectroscopy (DCS) in literature) which use coherent light and study photon correlation to extract blood flow dynamics[11–13]. Due to the different absorption characteristics of oxyhemoglobin and deoxyhemoglobin, NIRS can infer blood oxygenation levels based on the measured absorption coefficient μ_a and, additionally, assess changes in blood flow. In contrast, OCT determines absolute blood flow using the Doppler effect[14] but is limited by a low penetration depth of 1 to 3 mm. This limitation arises because conventional OCT detects only single scattered photons, which restricts its ability to measure CBF non-invasively, although recent advancements in OCT that utilize multiple scattering have been shown to enhance image contrast[15].

On the other hand, DWS employs a separate source-detector configuration to capture multiple scattered photons, offering the advantage of a higher penetration depth of 1 to 3 cm. However, the accuracy of DWS is contingent on the tissue's optical properties like reduced scattering coefficient μ_s' and the absorption coefficient μ_a, which can vary across different tissues and patients[16]. These are then ascertained with multiple methodologies, including NIRS. Furthermore, these techniques have distinct equipment requirements: DWS necessitates a light source with a long coherence length, NIRS requires a pulsed source or an intensity-modulated source, and OCT requires a stable, broad-bandwidth source or a swept source. Consequently, many experimental setups with complex instrumentation have been developed to integrate aspects of these techniques, as they provide complementary information[17–20]. Extracting all necessary parameters from a single modality is thus extremely essential and an ongoing effort in the light tissue interaction community. For instance, long coherence length pulsed lasers to combine DWS and TD-NIRS[16, 21, 22] have been demonstrated. New interferometric techniques have also demonstrated experiments to extract parameters from a single modality[23–26].

Furthermore, in CBF measurement, the flow dynamics in the scalp, skull, and cortex are compounded together, affecting the accuracy of CBF assessment. Increasing the source-detector separation in DWS can enhance specificity to deep flow but results in low photon throughput[27–29]. An alternative approach involves time-of-flight (ToF)-resolved techniques to analyze photon fluctuations from deeper layers, thereby excluding influences from shallower layers[16, 25, 26].

The optical frequency comb (OFC)[30–32] emerges as a promising solution to these limitations. It functions as a pulsed laser in the time domain, making it suitable for TD-NIRS. In the frequency domain, the OFC consists of numerous discrete, equally spaced narrow lines, which provide a sufficiently long coherence length for DWS. Recently Roberto et al.[33] used an electro-optical (EO) dual-comb system to measure the frequency response of a turbid medium and reconstruct the distribution of ToF (DTOF) via inverse Fourier transform. However, the dynamic properties have not been fully explored. Besides, EO combs currently require various high-speed modulators and RF sources and have coherence properties limited by the RF oscillator noise[34]. In contrast, passively mode-locked lasers can achieve lower noise and do not require any active modulation schemes, making them an appealing alternative. In the context of dual-comb generation, these advantages can be emphasized by ensuring that the two combs share the same laser cavity[35]. As well as reducing complexity, such approaches reduce noise as well since most perturbations to the cavity influence both combs in the same way, leading to a high degree of correlation in the fluctuations of the comb line frequencies. Single-cavity dual-comb sources and applications have become a hot topic as reviewed recently[36]. Here we use a spatial multiplexing approach where an intracavity Fresnel biprism is used to generate both combs in the same diode-pumped solid-state laser cavity arrangement[37]. This approach enables low-noise dual-comb generation while benefiting from the high power and low fundamental noise properties of diode-pumped solid-state lasers. In recent work, we have shown that these dual combs are compatible with coherent averaging and can support repetition rates up to a gigahertz or more[38]. Leveraging these characteristics, we demonstrate a dual-comb DWS system that simultaneously measures static properties (μ_s' and μ_a) and depth-dependent dynamics of a homogeneous turbid medium. By combining an auxiliary arm, we correct the relative timing jitter and relative carrier-envelope phase (CEP) shift for the measurement arm in post-processing. This approach simplifies traditional dual-comb implementation by avoiding the complexity associated with measuring, controlling, or tracking the absolute optical frequencies of the combs[39]. Furthermore, we use an etalon to reduce the optical bandwidth in order to boost the signal-to-noise ratio (SNR)[40]. This enables the detection of subtle features and weak signals, which were previously challenging to observe, thereby significantly enhancing the performance of the measurement system, resulting in a temporal resolution of 39 ps. For the first time, as far as we know, we have integrated TD-NIRS and DWS into a single modality using a dual-comb technique. Contrary to the approach taken by [33], we measure DTOF directly in the time domain. Our study confirms that the noise of our laser is sufficiently low that we can compensate for its timing and phase fluctuations in post-processing. This represents an advantage compared to the system reported in [33], and is very beneficial for dynamic measurements. Additionally, we explore the trade-offs between resolution, measurement speed, and SNR, highlighting how low resolution can lead to distortions in the true DTOF. We also propose strategies to mitigate this limitation.

2.2. METHODS

2.2.1. DTOF MEASUREMENT

ToF measurements based on dual-comb lasers such as light detection and ranging (LiDAR) [41] or OCT [42, 43], use two frequency combs with a delay increment of $\Delta f_{rep}/(f_{r1} f_{r2})$ each pulse period, thus achieving equivalent time sampling (ETS), also referred to as asynchronous optical sampling (ASOPS), where Δf_{rep} is the repetition difference of two comb and f_{r1} and f_{r2} is the repetition rate of two combs respectively. The complex representation of the electric field of the frequency comb is given by:

$$E(t) = \sum_{m=1}^{M} \sqrt{P(m)} \exp[-j(2\pi f_m t + \phi_m)], \tag{2.1}$$

where $P(m)$ is the power of the mth mode of the comb, $f_m = f_{ceo} + m f_{rep}$ is the optical frequency of the mth comb mode, f_{ceo} is the carrier-envelope offset frequency, $f_{rep} = f_{r1}$ or f_{r2}, is the repetition frequency, and ϕ_m is the phase offset of comb mode m.

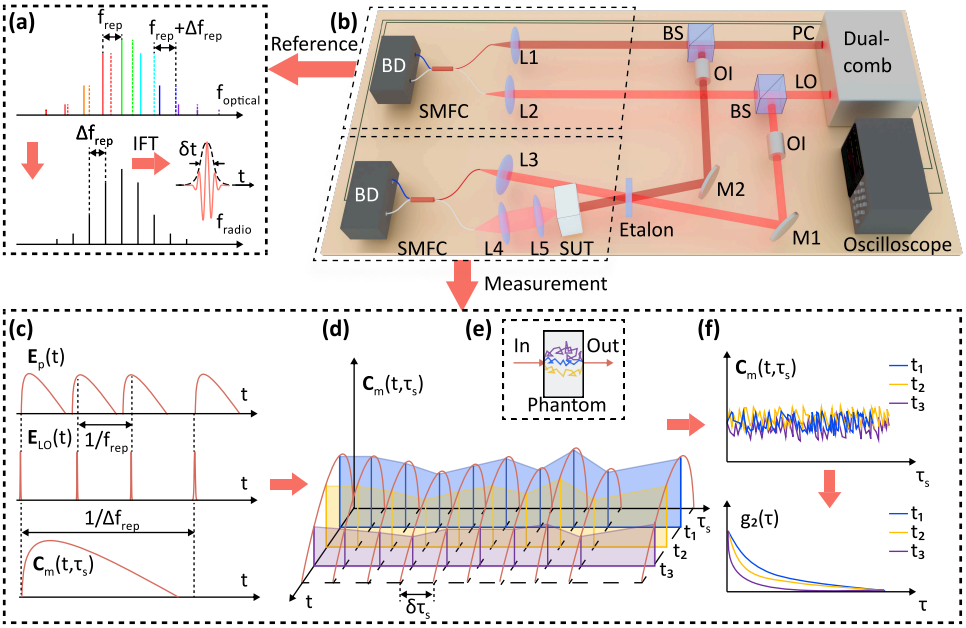

Figure 2.1: Schematic diagram of dual-comb diffuse correlation spectroscopy. (a) Dual-comb spectrum in the optical frequency domain and their interference spectrum in the radio frequency domain. (b) Two dual-comb Mach-Zehnder interferometers work as reference and measurement respectively; PC–probe comb, LO–local oscillator, BS–beam splitter, OI–optical isolator, L1-L5–lenses, M1-M2–mirror, SMFC–single mode fiber coupler, SUT–sample under test, BD–balanced detectors. (c) The ToFs of scattered photons obey a certain distribution (DTOF) which is a function of μ_s' and μ_a, and the LO scans them with step $\Delta f_{rep}/f_{r1} f_{r2}$ and finishes one cycle scanning in $1/\Delta f_{rep}$, $E_p(t)$ and $E_{LO}(t)$ is the electric field of probe comb and LO respectively. (d) The LO periodically scans the reemitted photons from each pulse at an interval $\delta_{\tau_s} = 1/\Delta f$. The interference signal fluctuates due to the dynamics of the scatterers. This rate of fluctuation varies for different ToFs. (e) Different scattering paths in the sample. (f) Trace the intensity of different ToFs and do auto-correlation, a longer ToF owns a higher decay rate. Note: all carrier oscillations are omitted in (c) and (d).

In the laser system used here (Figure 2.1(b)), both combs are emitted from the same spatially-multiplexed Yb:YAG dual-comb laser cavity and have central wavelengths of 1030 nm. The laser has a 247 MHz repetition rate and is similar in design to the one discussed in[44]. Cavity duplexing is achieved through the integration of a reflective biprism, enabling the delivery of two pulse trains directly from a single laser cavity. This configuration exhibits ultra-low relative noise properties and reaches an output power of 2 W.

After the beam splitters (BS), they are split into two arms. One arm serves as a reference where the probe comb and the local oscillator (LO) combine directly via a single-mode fiber coupler (SMFC) and are then detected by a balanced detector (BD) to monitor the status of the laser. The cross terms of comb modes belonging to the same comb, and that belonging to the other comb whose frequency difference is higher than $f_{\mathrm{rep}}/2$ disappear after applying bandpass filters. As a consequence, only the cross terms of adjacent comb modes belonging to two different combs are considered. The optical frequency is down-converted to $f_0 + m\Delta f_{\mathrm{rep}}$, thus generating a new comb in the radio frequency domain that the balanced detectors can detect (Figure 2.1(a)), where f_0 is an effective start frequency of the RF comb. Balanced detectors remove the DC component of the interferogram yielding:

$$C_{\mathrm{s}}(t) = 2\sum_{m=1}^{M}\sqrt{P_{\mathrm{p}}(m)P_{\mathrm{LO}}(m)}\cos[2\pi(f_0 + m\Delta f_{\mathrm{rep}})t + \varphi_{\mathrm{m}}] \tag{2.2}$$

where $P_{\mathrm{p}}(m)$ and $P_{\mathrm{LO}}(m)$ is the power of the mth mode of corresponding source, and φ_m is the phase offset for mth comb mode.

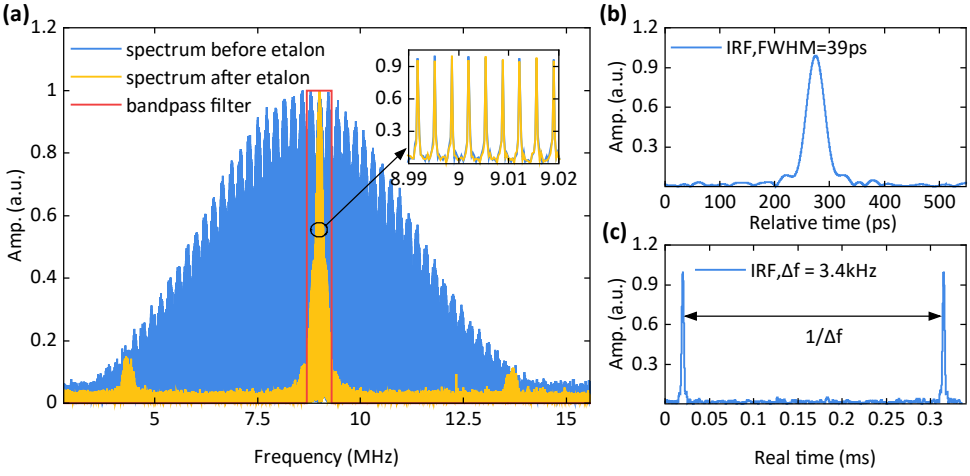

Figure 2.2: Laser spectrum, instrument response function, and the refresh rate. (a) The spectrum of the radio frequency comb, the blue line represents the spectrum before etalon, the yellow line represents the spectrum after etalon, and the red line represents the bandpass filter used for post-processing; the inset is the zoom-in of the central spectrum. (b) The envelope of interference signal in the reference arm is the instrument response function (IRF) here. (c) The adjacent pulses in the time domain, the refresh rate indicates the measurement speed. Note: $t_{\mathrm{r}} = t/(f_{\mathrm{rep}}/\Delta f_{\mathrm{rep}})$, where t is the real time and t_{r} is the relative time between two combs.

In the measurement arm, an etalon is placed before the sample to decrease the illumination power. By doing so, we keep the average power of individual comb modes as high as possible and reduce the detection bandwidth, thus raising SNR[40], and the detailed description is shown in section 3. C. Two side peaks owing to the short etalon free spectral (around 1.5 nm) are filtered out by a digital bandpass filter in post-processing (Figure 2.2(a)). After the etalon and bandpass filter, the optical power of the probe comb is around 100 mW. In [45] a maximum permissible exposure (MPE) of 103 mW was reported with a 1-mm-diameter beam and 1064-nm light. Our configuration closely corresponds to this MPE (100 mW average power and 1030 nm wavelength). On the other hand, the power of the LO is set to 3 mW, which is significantly higher than the power of the diffused photons collected. By leveraging the heterodyne gain, such weak signals can be detected, and achieve shot-noise-limited SNR. In the end, 23.27 GHz FWHM optical bandwidth is utilized to give 39 ps characteristic temporal resolution (Figure 2.2(b)), and the repetition difference ($1/\Delta f_{\mathrm{rep}}$) is set to 3.4 kHz, thus resulting in $1/\Delta f_{\mathrm{rep}} = 294\ \mu$s decay resolution (Figure 2.2(c)).

Photons emitted from the probe comb undergo multiple scattering events within the sample, following various paths as depicted in Figure 2.1(e). This process leads to a distribution of ToF for the photons, known as the distribution of time-of-flight (DTOF). The DTOF of photons in a turbid slab is described in [46], where the pulse laser is modeled as a delta function, and the intensity of their ToFs is derived. Because of a slight repetition frequency difference between the probe comb and the LO, the LO interferes with different portions of scattered photons each period with step $\Delta f_{\mathrm{rep}}/f_{\mathrm{r1}}f_{\mathrm{r2}}$, and after $1/\Delta f_{\mathrm{rep}}$, LO and PC have a maximum delay difference of $1/f_{r1}$ and thus overlapping at the start of the next cycle, as shown in Figure 2.1 (c). The cross term of two combs in the measurement arm is given by:

$$C_{\mathrm{m}}(t,\tau_{\mathrm{s}}) = C_{\mathrm{s}}(t,\tau_{\mathrm{s}}) \otimes P(\rho,d,t,\tau_{\mathrm{s}}),\ t \in [0, 1/\Delta f_{\mathrm{rep}}] \tag{2.3}$$

where τ_{s} is a slow timescale representing the interferogram period, and it therefore has discrete values of $n/\Delta f_{\mathrm{rep}}$, t is the absolute time and can be transformed to relative time t_{r} by $t_{\mathrm{r}} = t/(f_{\mathrm{rep}}/\Delta f_{\mathrm{rep}})$, $P(\rho,d,t,\tau_{\mathrm{s}})$ is the DTOF of photons, ρ is the horizontal distance between source and detector, d is the thickness of the sample, and $\otimes$ denotes convolution.

Direct deconvolution of C_{m} and C_{s} cannot accurately yield $P(\rho,d,t,\tau_{\mathrm{s}})$ due to the presence of high noise. In addition, transforming C_{m} to the frequency domain and doing demultiplication is not effective either, as the noise overwhelms the comb modes. However, we have discovered that by averaging the envelope of C_{m}, it is possible to successfully reconstruct $P(\rho,d,t)$.

To show how envelope averaging constructs DTOF, a simulation is conducted. We consider scattering photons with different ToFs as being reflected from a distribution of virtual mirrors located at different depths in the sample (Figure 2.3 (a)). The reflected signal is obtained by the convolution of $C_{\mathrm{s}}(t)$ and $P(\rho,d,t,\tau_{\mathrm{s}})$, where we set $\rho = 0$, $d =$ 10 mm. To mimic dynamics, the ToF distribution is reinitialized with a different set of virtual mirror positions following the same statistical distribution. The FWHM of $C_{\mathrm{s}}(t)$ is 39 ps (relative time).

Initially, when δt (the separation of reflected photons) ranges between 50-100 ps, as

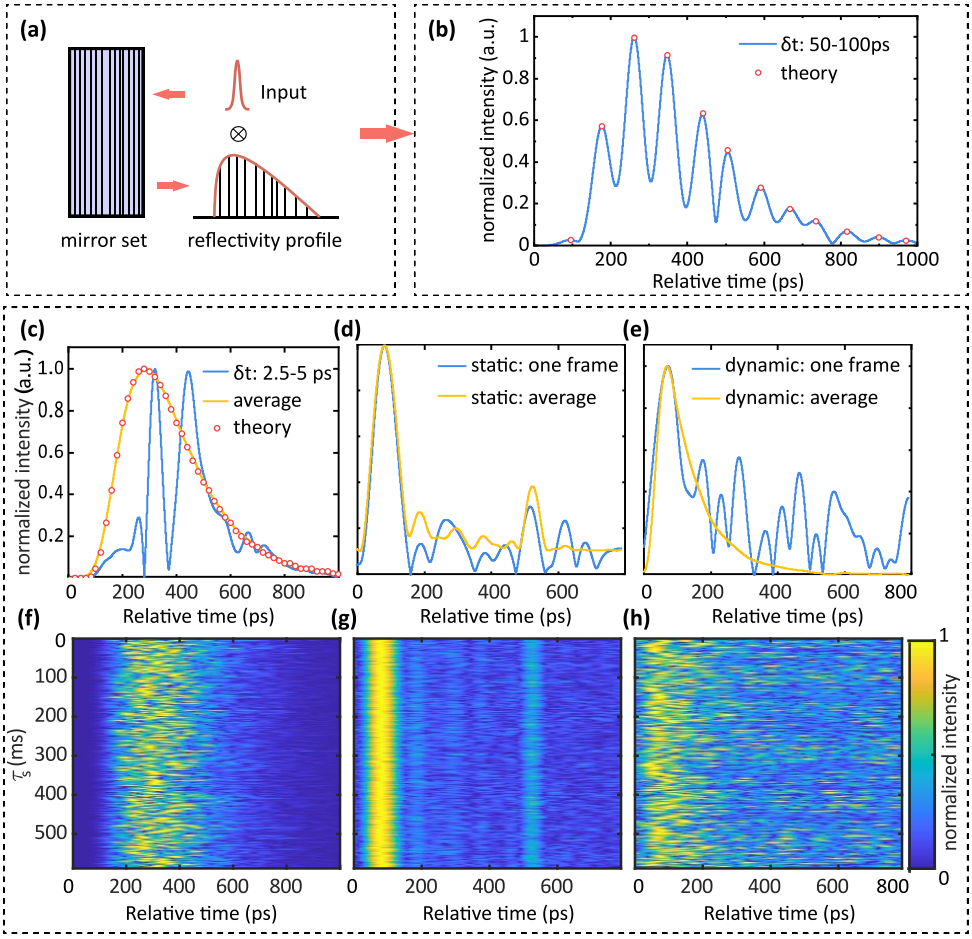

Figure 2.3: The influence of low resolution: a simulation, static sample measurement and dynamic sample measurement. (a) Schematic diagram of simulation. The scattering sample is modeled as a mirror set with a reflectivity profile. (b),(c) 39 ps-FWHM IRF convolved with reflectivity profile with 50-100 ps and 2.5-5 ps ToF separation respectively, and the red dot represents mirror reflectivity. (d),(e) One interferogram envelope of a static and a dynamic sample and 2000 interferogram averaging results. (f)-(h) The interferogram envelope over 2000 frames of the simulation, static sample, and dynamic sample. The horizontal axis represents ToF, the vertical axis represents the time lag of different measurement periods, and colorbar represents normalized intensity.

shown in Figure 2.3 (b), the resolution of the dual-comb system is sufficiently high to differentiate between the reflections from the different mirrors. The peaks of the envelope of $C_m(t)$ align well with theoretical predictions. Subsequently, when δt is reduced to 2.5-5 ps (Figure 2.3 (c)), the mirrors can no longer be resolved by the dual-comb system. This setup differs from a typical low-coherence pulsed laser system, as photons reflected from adjacent mirrors are coherent and thus interfere with each other, leading to artifacts (illustrated by the blue line in Figure 2.3 (c)). However, by averaging 2000 ran-

domly generated interferogram envelopes (Figure 2.3 (f)), these interference effects can be mitigated. The result (shown by the yellow line in Figure 2.3 (c)) aligns closely with the predefined set $P(\rho, d, t, \tau_s)$.

We also show the result of a static sample with 9.5 cm^{-1} $\mu_s^{'}$ and 0.05 cm^{-1} μ_a, which is made of glass spheres and polydimethylsiloxane and cured at 75 °C[47]. Since the scatterers remain stationary, the ToF separation remains unchanged, and the interferogram of each frame remains stable except for some white noise (Figure 2.3 (g)). Consequently, the averaged results show no significant difference compared with a single frame (Figure 2.3 (d)). Conversely, for a dynamic sample (Intralipid phantom), the moving scatters cause ToF separation to keep changing thus the interferogram of each frame is different. By averaging, the true DTOF can be constructed (Figure 2.3 (e)), which is compared with the diffusion theory in section 3. A. The small peak around 500 ps in Figure 2.3 (d) and (g) comes from spurious reflection in the setup or inside the laser. In the dynamic phantom measurement, we included an additional fiber to introduce a delay such that this peak is temporally separated from the signal of interest near relative time = 0.

2.2.2. DYNAMICS MEASUREMENT

To start the measurement of the dynamic sample, the CEP shift in the measurement arm must be clarified. The dynamics of particles inside the sample cause a phase shift of each scattering path, as a result, the interferogram of the two combs fluctuates. In biological tissue, red blood cells (RBCs) from different layers have different velocities, and in the homogenous turbid medium, the scattering event number varies at different ToFs, thus the phase shift velocity varies. This can be distinguished by tracing the fluctuation at different ToFs and applying autocorrelation to them, as shown in Figure 2.1 (d) and (f). However, because the laser is in free-running mode it exhibits small but timing jitter and optical phase fluctuations of the dual-comb interferograms, which are mainly from mechanical/acoustic noise and pump diode fluctuations. By accounting for these fluctuations via a reference channel, much more information can be obtained in the dynamic measurement. In dual-comb spectroscopy phase and timing errors can be corrected digitally to obtain coherently averaged signals[48]. Usually, those errors are easier to correct for high repetition difference as the higher repetition difference corresponds to a higher tracking speed. In this work, by using a mechanically robust prototype implementation of spatial multiplexing, we are able to satisfy the condition for coherent averaging at <1 kHz Δf_{rep} [38]. To compensate for the relative timing jitter and relative phase shift in the measurement arm, we build a reference arm to monitor those parameters and then correct them for the measurement arm. After this, the path-dependent intensity auto-correlation is calculated by:

$$g_2(s,\tau) = \frac{< C_m(s,\tau_s) C_m(s,\tau_s+\tau) >}{< C_m(s,\tau_s) >^2} \tag{2.4}$$

Where $s = n_m c t$ is the path length of scattering photons, n_m is the refractive index of the medium, and c is the light speed in vacuum. Furthermore, the intensity auto-correlation is related to field auto-correlation by Siegert relation: $g_2(\tau) = 1+\beta|g_1(\tau)|^2$, where β ranges from 0 to 1 and accounts for the measured speckle number. According to diffusing wave spectroscopy (DWS)[49], the path-dependent normalized field autocorrelation function

is denoted by:

$$g_1(\tau, s) = \exp\left(-2k_0^2 \mu_s' s D_B \tau\right), \tag{2.5}$$

where D_B is the Brownian motion coefficient, $\mu_s^{'}$ is the reduced scattering coefficient of turbid medium and k_0 is the wavenumber of the light in the medium. In biological tissue, photons are scattered by RBCs in different vessels. Although RBCs exhibit laminar flow within a single vessel, their dynamics resemble Brownian motion when measured using DWS[50]. Combined with the blood volume fraction (denoted as α), the blood flow index αD_B can be calculated.

2.2.3. SNR

In a dual-comb interferometer, the peak value of the interference signal is given by:

$$i_s = 2\sqrt{P_p P_{LO}}\eta \tag{2.6}$$

where i_s (A) is the current after the balanced detector, η (A/W) is the responsivity of the balanced detector, P_p (W) and P_{LO} (W) is the average power of transmitted probe comb and LO respectively. The laser intensity noise is neglected due to the ultra-low noise of the laser utilized here and the balanced detection canceling out common noise, therefore only shot noise and detector noise are considered here:

$$i_n^2 = i_{sn}^2 + i_{dn}^2 \tag{2.7}$$

where shot noise $i_{sn}^2 = 2qB\bar{i} = 2qB(P_p + P_{LO})\eta = 2qBP_{LO}\eta$ ($P_p << P_{LO}$), B is the detection bandwidth, and q is the electron charge. The detector noise $i_{dn}^2 = (NEP\sqrt{B}\eta)^2$, $NEP(W/\sqrt{Hz})$ is the noise-equivalent power of the detector. When increasing the power of the LO, $i_{sn}^2 >> i_{dn}^2$, thus the shot-noise limited SNR can be achieved:

$$\mathrm{SNR}_{sl} = \frac{i_s^2}{i_n^2} = \frac{2\eta P_p}{qB} \tag{2.8}$$

For a given power of probe comb, SNR_{sl} is limited by detection bandwidth, which is related to temporal resolution by $\delta(\mathrm{ToF}) \sim \lambda^2/\Delta\lambda$, and λ is the central wavelength and $\Delta\lambda$ is the optical bandwidth and is mapped into the radio frequency domain in dual-comb measurement. The detection bandwidth is given by $B = N\Delta f_{\mathrm{rep}}$, and P_p can further be written by $P_p = NP_m$, where P_m is the power of a single comb mode and N is the number of modes after the bandpass filter (rectangular spectrum is assumed here), then:

$$\mathrm{SNR}_{sl} = \frac{2\eta P_m}{q\Delta f_{\mathrm{rep}}} \tag{2.9}$$

For a given measurement speed (Δf_{rep}), P_m determines the shot-noise limited SNR and is limited by maximum permissible exposure (MPE).

In general, there is a trade-off in dual-comb DWS between temporal resolution, measurement speed, and SNR. This trade-off should be considered carefully when analyzing dynamics in deep tissue since stronger scattering leads to a reduced wavefront overlap

of the scattered photons with the local oscillator comb photons. Here, the repetition difference of the dual-comb laser is set to 3.4 kHz (Δf_{rep} can be adjusted to an arbitrary value, and the maximum Δf_{rep} depends on the internal optical configuration inside the cavity and can be tens of kHz), and an etalon is employed to narrow down the optical bandwidth, meanwhile, a digital bandpass filter is applied to the RF comb spectrum. By doing so, there are several benefits: 1) The SNR is proportional to the measurement time, so by reducing Δf_{rep} we obtain a large SNR from a single period, without the need to coherently average multiple periods. 2) The etalon filters other comb modes and reduces the power of the PC and the LO. The power reduction of PC makes sure that it is lower than MPE and meanwhile keeps the power of individual comb modes as high as possible, which gives us high SNR (as shown in equation (9)). 3) The bandpass filter fits the RF comb spectrum and enables us to remove noise in the absence of the signal, which increases shot-noise limited SNR (as shown in equation (8)).

2.3. RESULTS

2.3.1. STATIC PROPERTIES

To validate the ability of DTOF measurement of the dual-comb system, we build a set of 10 mm thickness homogeneous samples, which consist of 6 ml pure water and 0.2-2 ml 20% Intralipid emulsion (Sigma Aldrich, 0.2 ml per step), and place them in the measurement arm.

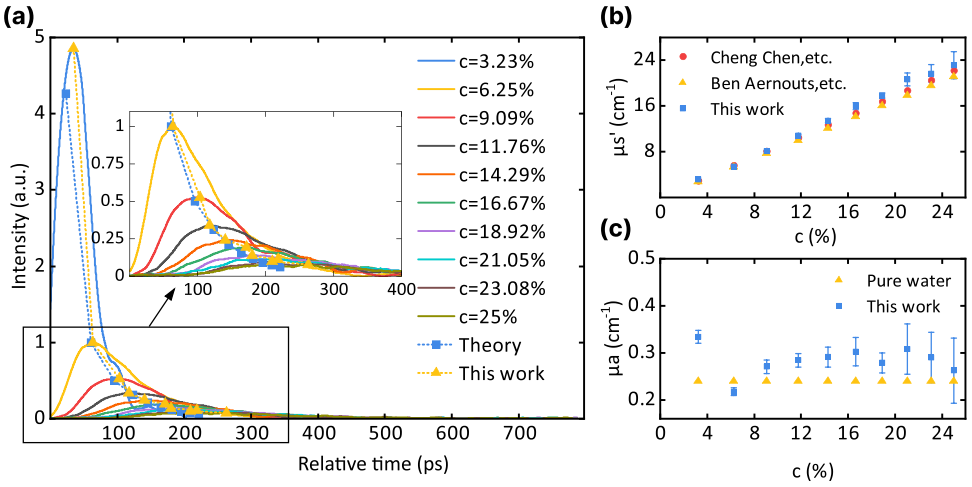

Figure 2.4: Measured DTOF, reduced scattering coefficient (μ_s') and absorption coefficient (μ_a) of samples with different Intralipid concentrations. (a) Measured DTOF curves of the sample with different concentrations. The peak points and their arrival times are compared with that of diffusion theory. (b) DTOF curves are fitted to extract the reduced scattering coefficient, compared with the value in the literature[51, 52]. (c) Compare the extracted absorption coefficient with pure water[53].

During the measurement, we removed the sample at first to obtain the peak position of the interferogram. Then we calculated back to determine the start point of DTOF using the thickness of the sample. The DTOF is acquired by averaging the envelope of the

interferogram and deconvolved with IRF. Figure 2.4 (a) shows the DTOF of 10 samples (10 measurements per sample) and their intensities are normalized by the c = 6.25% sample. As the concentration increases, the intensity decreases due to scattering, and the arrival time of peaks is delayed. To compare with the diffusion theory, the theoretical $\mu_s^{'}$ of 20% Intralipid[52] and μ_a of pure water[53] at 1030 nm (μ_a of Intralipid is smaller than water) are referred. For samples with different concentrations, the reduced scattering coefficient is calculated by $\mu(c)_s^{'} = c\mu_s^{'}$, and μ_a remains the same. By substituting those values into $P(\rho, d, t, \tau_s)$[46], the peak value and arrival time of different samples are predicted, and compared with this work (Figure 2.4 (a)). Except for the case where c = 3.23%, which does not align with diffusion theory due to low scattering, the other cases largely conform to diffusion theory. Furthermore, we fit the DTOF curve and extract $\mu_s^{'}$ (Figure 2.4 (b)) and μ_a (Figure 2.4 (c)) by $P(\rho, d, t)$. The measured $\mu_s^{'}$ show high alignment with the results in [51] and [52]. μ_a shows a discrepancy in the first sample but close to the result in [53] when concentration rises.

2.3.2. DYNAMIC PROPERTIES

Although the single cavity dual comb owns the merits of ultralow noise, environmental disturbances such as vibrations lead to jitter in the timing and CEP of the interferograms. In the measurement arm, the phase shifts that come from the dynamics of the sample are compounded with the laser itself. Therefore, it is necessary to compensate for those relative phase shifts that come from the laser first.

Owing to the high SNR in the reference arm, the relative timing jitter and the relative CEP shift can easily be extracted and compensated by using the method [38] described earlier. Figure 2.5 (a) shows the relative timing jitter of the pulses before compensation in the reference arm, which is the main reason for the relative CEP shift (Figure 2.5 (b)). The unwrapped relative phase shift before compensation grows quadratically (blue line in Figure 2.5 (b)) while it is flat (equals 0, red line in Figure 2.5 (b)) after compensation in the reference arm. After compensating them to the measurement arm where the sample is removed, the relative CEP is much lower than 2π (yellow line in Figure 2.5 (b)). Moreover, we also show the compensation result of a static sample (yellow line in Figure 2.5 (c)) and dynamic sample (blue line in Figure 2.5 (c)), the former is close to 0 but the latter bounds between $-\pi$ and π, which reveals that only movement of scatters induces phase shift after compensation. After tracing the peak point of the interferogram in air, and certain ToF in the static and dynamic sample, the second-order auto-correlation (g_2) is calculated (Figure 2. 5 (d)). For air and static samples, g_2 is expected to be flat; however, in our observations, it drops to zero immediately before and after compensation. This phenomenon occurs because the standard auto-correlation function employed here first subtracts the mean value of the signal, leaving only white noise (comprising shot noise and electronic noise). Since white noise does not exhibit any correlation, we see a drop. For dynamic samples, the drop observed before compensation is similar and can be attributed to laser noise. After compensation, we first notice a drop due to white noise, followed by a decay curve. This curve provides dynamic information about the sample, i.e. Brownian motion coefficient of the sample.

To reduce the Brownian motion speed that can be measured by this system's refresh rate, we mixed 18 ml 20% Intralipid emulsion with 10 ml glycerin, whose viscosity is

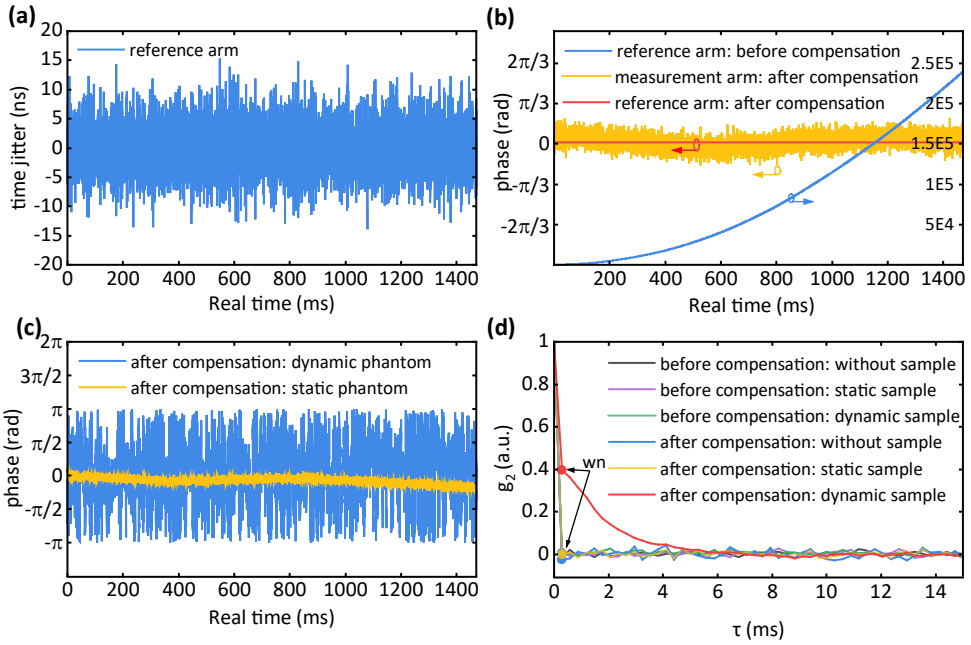

Figure 2.5: Measurement of the timing and phase noise properties of the interferograms and their correction. (a) Relative timing jitter between the two combs (equivalently, timing jitter of the interferograms scaled down to the optical domain by the factor $\Delta f_{\mathrm{rep}}/f_{\mathrm{rep}}$). (b) The unwrapped relative CEP shifts before and after compensation in the reference arm, and that of the measurement arm after compensation without a sample. (c) The CEP shifts of the interferogram after compensation in the measurement arm with the static and dynamic sample. (d) Comparison of the second-order auto-correlation before and after compensation with air, static sample, dynamic sample, and wn represents white noise drop.

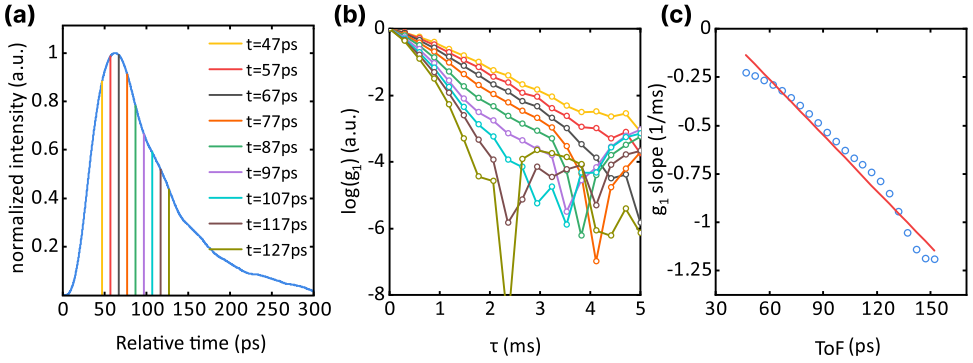

Figure 2.6: Traced intensity fluctuation of different ToFs, and the first-order auto-correlation used to extract the Browian coefficient. (a) DTOF curve of Intralipid sample. (b) g_1 of the different decay rates at different ToFs. (c) The decay rate increases linearly with ToFs.

higher than pure water. After the relative timing jitter and relative phase shift are compensated, the movement of scatters is the only cause of the intensity fluctuation. μ_s'

is measured by using the method described in Section 2. A to be 5.6 cm^{-1} (Figure 2.6 (a)) for a homogenous Intralipid sample where only Brownian motion exists. Figure 2.6 (a) shows how the ToF is distributed in the Intralipid sample. The vertical lines indicate specific relative times, and in Figure 2.6 (b) we show the autocorrelation function $g_1(\tau)$ for these relative times. As expected, components with a larger ToF (i.e. a larger relative time in Figure 2.6 (a)) exhibit a faster decay of $g_1(\tau)$ with respect to real-time τ. From equation (5), the decay slope is proportional to the ToF t according to $d[\ln(g_1(\tau))]/d\tau = -2k_0^2\mu_s' s D_B = -2k_0^2\mu_s' D_B v t$. To quantify this dependence, in Figure 2.6 (c) we show the decay rate as a function of ToF. The figure confirms the linear relation, and we can infer a Brownian motion coefficient $D_B = 0.27\times10^{-12}\ m^2/s$.

2.4. CONCLUSION AND DISCUSSION

Dual-comb technology, known for its ultra-stable frequency and broadened bandwidth, has been widely utilized in absorption spectroscopy and precise metrology. However, its practical application has been limited due to high system complexity. We have demonstrated a dual-comb system with a simpler configuration specifically for medical applications, offering three significant advantages.

Firstly, the laser's novel structure enables high power output and low relative intensity noise (RIN) without the need for a laser amplifier, thereby avoiding the amplified spontaneous emission (ASE) noise typically associated with such amplifiers. The single-cavity design produces two independent pulse trains with significant noise correlations, eliminating the locking electronics requirement as mutual coherence is obtained passively. Additionally, the 250 MHz repetition rate laser is rather simple and compact and can avoid DTOF overlap for clinic requirements. Furthermore, the combination of high power and an etalon significantly enhances the SNR. The ultra-low noise level allows for the measurement of sample dynamics using a coherent averaging algorithm at a repetition rate difference as low as 3.4 kHz.

Secondly, our dual-comb DWS system can simultaneously measure the absorption coefficient (μ_a), the reduced scattering coefficient (μ_s'), and dynamic properties. While averaging is necessary to obtain the DTOF, μ_a and μ_s' typically do not fluctuate rapidly over time. In our experience, averaging over approximately 2000 frames (0.59 seconds) is sufficient to construct DTOF, although this may vary depending on the μ_s' and μ_a of the sample. Additionally, our findings offer insights for dual-comb OCT, particularly that a sufficiently high laser bandwidth is crucial to avoid artifacts caused by interference between adjacent layers. Further research using an appropriate frequency comb laser with an emission spectrum spanning an isobestic point of blood, will allow the distinct absorption characteristics of oxyhemoglobin and deoxyhemoglobin to be measured. This will enable the quantification of blood oxygenation from μ_a. Moreover, by combining this with blood flow measurements, we can also determine blood metabolism in the future.

Lastly, This system effectively differentiates dynamics from various paths (or TOFs), crucial for analyzing multi-layer dynamics as photons that traverse deeper layers exhibit longer ToFs. For CBF measurements, this capability is precious as it helps to mitigate the influence of the scalp and skull, thereby enhancing the specificity to deep tissue and im-

proving the accuracy of thrombus localization for ischemic stroke. However, the specificity to deeper layers is also dependent on the SNR. Given the low duty cycle of pulsed lasers, optimizing bandwidth, measurement speed, and illumination power is essential to achieve performance comparable to that of continuous lasers. Enhancing the signal-to-noise ratio (SNR) will be a primary focus of our future work. We also see that the use of a broadband coherent pulsed source will remove the need for many light sources or spectral scanning needed to access optical properties in biological media.

2.5. FUNDING SOURCES

This work was partially supported by a BRIDGE Discovery Project Nr. 40B2 – 0_180933 a joint research program of the Swiss National Science Foundation (SNSF) and Innosuisse – the Swiss Innovation Agency. The authors, Binbin Zhang, Esteban Venialgo Araujo, Sophinese Iskander-Rizk, and Nandini Bhattacharya would like to acknowledge the PME department for funding this work.

2.6. ACKNOWLEDGEMENT

We sincerely thank Ruben Guis for his insights on ASOPS measurements, Merle Losch, Hamed Abbasi and Xiliang Yang for their assistance with the phantom measurements, and Weiwei Kang for her work on drawing Figure 1 (b) and (d).

BIBLIOGRAPHY

[1] E. Bandera, M. Botteri, C. Minelli, A. Sutton, K. R. Abrams, and N. Latronico, "Cerebral blood flow threshold of ischemic penumbra and infarct core in acute ischemic stroke: a systematic review", Stroke **37**, 1334–1339 (2006).

[2] V. V. Olavarría, H. Arima, C. S. Anderson, A. M. Brunser, P. Muñoz-Venturelli, S. Heritier, and P. M. Lavados, "Head position and cerebral blood flow velocity in acute ischemic stroke: a systematic review and meta-analysis", Cerebrovasc. Dis. **37**, 401–408 (2014).

[3] B. F. Tomandl, E. Klotz, R. Handschu, B. Stemper, F. Reinhardt, W. J. Huk, K. Eberhardt, and S. Fateh-Moghadam, "Comprehensive imaging of ischemic stroke with multisection ct", Radiographics **23**, 565–592 (2003).

[4] P. Vilela and H. A. Rowley, "Brain ischemia: ct and mri techniques in acute ischemic stroke", Eur. J. Radiol. **96**, 162–172 (2017).

[5] R. G. González, "Clinical mri of acute ischemic stroke", J. Magn. Reson. Imaging **36**, 259–271 (2012).

[6] B. J. Kim, H. G. Kang, H.-J. Kim, S.-H. Ahn, N. Y. Kim, S. Warach, and D.-W. Kang, "Magnetic resonance imaging in acute ischemic stroke treatment", J. Stroke **16**, 131 (2014).

[7] T. Durduran, R. Choe, W. B. Baker, and A. G. Yodh, "Diffuse optics for tissue monitoring and tomography", Reports on progress in physics **73**, 076701 (2010).

[8] A. Torricelli, D. Contini, A. Pifferi, M. Caffini, R. Re, L. Zucchelli, and L. Spinelli, "Time domain functional nirs imaging for human brain mapping", Neuroimage **85**, 28–50 (2014).

[9] S. Fantini and A. Sassaroli, "Frequency-domain techniques for cerebral and functional near-infrared spectroscopy", Front. Neurosci. **14**, 300 (2020).

[10] D. Huang, E. A. Swanson, C. P. Lin, J. S. Schuman, W. G. Stinson, W. Chang, M. R. Hee, T. Flotte, K. Gregory, C. A. Puliafito, and J. G. Fujimoto, "Optical coherence tomography", science **254**, 1178–1181 (1991).

[11] T. Durduran and A. G. Yodh, "Diffuse correlation spectroscopy for non-invasive, microvascular cerebral blood flow measurement", Neuroimage **85**, 51–63 (2014).

[12] E. M. Buckley, A. B. Parthasarathy, P. E. Grant, A. G. Yodh, and M. A. Franceschini, "Diffuse correlation spectroscopy for measurement of cerebral blood flow: future prospects", Neurophotonics **1**, 011009–011009 (2014).

[13] H. Ayaz, W. B. Baker, G. Blaney, D. A. Boas, H. Bortfeld, K. Brady, J. Brake, S. Brigadoi, E. M. Buckley, S. A. Carp, et al., "Optical imaging and spectroscopy for the study of the human brain: status report", Neurophotonics **9**, S24001 (2022).

[14] A. M. Rollins, S. Yazdanfar, J. K. Barton, and J. A. Izatt, "Real-time in vivo color doppler optical coherence tomography", J. Biomed. Opt. **7**, 123–129 (2002).

[15] G. R. Untracht, M. Chen, P. Wijesinghe, J. Mas, H. T. Yura, D. Marti, P. E. Andersen, and K. Dholakia, "Spatially offset optical coherence tomography: leveraging multiple scattering for high-contrast imaging at depth in turbid media", Sci. Adv. **9**, eadh5435 (2023).

[16] J. Sutin, B. Zimmerman, D. Tyulmankov, D. Tamborini, K. C. Wu, J. Selb, A. Gulinatti, I. Rech, A. Tosi, D. A. Boas, et al., "Time-domain diffuse correlation spectroscopy", Optica **3**, 1006–1013 (2016).

[17] J. Schmitt, A. Knüttel, and R. Bonner, "Measurement of optical properties of biological tissues by low-coherence reflectometry", Appl. Opt. **32**, 6032–6042 (1993).

[18] A. Yodh, P. Kaplan, and D. Pine, "Pulsed diffusing-wave spectroscopy: high resolution through nonlinear optical gating", Phys. Rev. B **42**, 4744 (1990).

[19] M. N. Kim, T. Durduran, S. Frangos, B. L. Edlow, E. M. Buckley, H. E. Moss, C. Zhou, G. Yu, R. Choe, E. Maloney-Wilensky, L. W. Ronald, M. S. Grady, H. G. Joel, M. L. Joshua, A. G. Yodh, A. D. John, and K. W. Andrew, "Noninvasive measurement of cerebral blood flow and blood oxygenation using near-infrared and diffuse correlation spectroscopies in critically brain-injured adults", Neurocrit. Care **12**, 173–180 (2010).

[20] K. Verdecchia, M. Diop, T.-Y. Lee, and K. St. Lawrence, "Quantifying the cerebral metabolic rate of oxygen by combining diffuse correlation spectroscopy and time-resolved near-infrared spectroscopy", J. Biomed. Opt. **18**, 027007–027007 (2013).

[21] M. Pagliazzi, S. K. V. Sekar, L. Colombo, E. Martinenghi, J. Minnema, R. Erdmann, D. Contini, A. D. Mora, A. Torricelli, A. Pifferi, et al., "Time domain diffuse correlation spectroscopy with a high coherence pulsed source: in vivo and phantom results", Biomedical optics express **8**, 5311–5325 (2017).

[22] L. Colombo, S. Samaei, P. Lanka, D. Ancora, M. Pagliazzi, T. Durduran, P. Sawosz, A. Liebert, and A. Pifferi, "Coherent fluctuations in time-domain diffuse optics", APL Photonics **5** (2020).

[23] L. Mei, G. Somesfalean, and S. Svanberg, "Frequency-modulated light scattering interferometry employed for optical properties and dynamics studies of turbid media", Biomedical Optics Express **5**, 2810–2822 (2014).

[24] O. Kholiqov, W. Zhou, T. Zhang, V. Du Le, and V. J. Srinivasan, "Time-of-flight resolved light field fluctuations reveal deep human tissue physiology", Nature communications **11**, 391 (2020).

[25] D. Borycki, O. Kholiqov, S. P. Chong, and V. J. Srinivasan, "Interferometric near-infrared spectroscopy (inirs) for determination of optical and dynamical properties of turbid media", Optics express **24**, 329–354 (2016).

[26] M. Zhao, W. Zhou, S. Aparanji, D. Mazumder, and V. J. Srinivasan, "Interferometric diffusing wave spectroscopy imaging with an electronically variable time-of-flight filter", Optica **10**, 42–52 (2023).

[27] M. B. Robinson, D. A. Boas, S. Sakadzic, M. A. Franceschini, and S. A. Carp, "Interferometric diffuse correlation spectroscopy improves measurements at long source–detector separation and low photon count rate", J. Biomed. Opt. **25**, 097004–097004 (2020).

[28] W. Zhou, O. Kholiqov, S. P. Chong, and V. J. Srinivasan, "Highly parallel, interferometric diffusing wave spectroscopy for monitoring cerebral blood flow dynamics", Optica **5**, 518–527 (2018).

[29]H. Zhao and E. M. Buckley, "Influence of source–detector separation on diffuse correlation spectroscopy measurements of cerebral blood flow with a multilayered analytical model", Neurophotonics **9**, 035002–035002 (2022).

[30]H. R. Telle, G. Steinmeyer, A. E. Dunlop, J. Stenger, D. H. Sutter, and U. Keller, "Carrier-envelope offset phase control: a novel concept for absolute optical frequency measurement and ultrashort pulse generation", Appl. Phys. B **69**, 327–332 (1999).

[31]S. A. Diddams, D. J. Jones, J. Ye, S. T. Cundiff, J. L. Hall, J. K. Ranka, R. S. Windeler, R. Holzwarth, T. Udem, and T. W. Hänsch, "Direct link between microwave and optical frequencies with a 300 thz femtosecond laser comb", Phys. Rev. Lett. **84**, 5102 (2000).

[32]A. Schliesser, N. Picqué, and T. W. Hänsch, "Mid-infrared frequency combs", Nat. Photonics **6**, 440–449 (2012).

[33]R. Barreiro, F. Sanabria-Macías, J. Posada, P. Martín-Mateos, and C. de Dios, "Experimental demonstration of a new near-infrared spectroscopy technique based on optical dual-comb: dc-nirs", Sci. Rep. **13**, 10924 (2023).

[34]A. Parriaux, K. Hammani, and G. Millot, "Electro-optic frequency combs", Adv. Opt. Photonics **12**, 223–287 (2020).

[35]S. M. Link, A. Klenner, M. Mangold, C. A. Zaugg, M. Golling, B. W. Tilma, and U. Keller, "Dual-comb modelocked laser", Opt. Express **23**, 5521–5531 (2015).

[36]R. Liao, H. Tian, W. Liu, R. Li, Y. Song, and M. Hu, "Dual-comb generation from a single laser source: principles and spectroscopic applications towards mid-ir—a review", J. Phys. Photo. **2**, 042006 (2020).

[37]J. Pupeikis, B. Willenberg, S. L. Camenzind, A. Benayad, P. Camy, C. R. Phillips, and U. Keller, "Spatially multiplexed single-cavity dual-comb laser", Optica **9**, 713–716 (2022).

[38]C. R. Phillips, B. Willenberg, A. Nussbaum-Lapping, F. Callegari, S. L. Camenzind, J. Pupeikis, and U. Keller, "Coherently averaged dual-comb spectroscopy with a low-noise and high-power free-running gigahertz dual-comb laser", Opt. Express **31**, 7103–7119 (2023).

[39]D. J. Jones, S. A. Diddams, J. K. Ranka, A. Stentz, R. S. Windeler, J. L. Hall, and S. T. Cundiff, "Carrier-envelope phase control of femtosecond mode-locked lasers and direct optical frequency synthesis", Science **288**, 635–639 (2000).

[40]N. R. Newbury, I. Coddington, and W. Swann, "Sensitivity of coherent dual-comb spectroscopy", Opt. Express **18**, 7929–7945 (2010).

[41]Z. Zhu and G. Wu, "Dual-comb ranging", Engineering **4**, 772–778 (2018).

[42]S.-J. Lee, B. Widiyatmoko, M. Kourogi, and M. Ohtsu, "Ultrahigh scanning speed optical coherence tomography using optical frequency comb generators", Jpn. J. Appl. Phys. **40**, L878 (2001).

[43]S. Kray, F. Spöler, M. Först, and H. Kurz, "Dual femtosecond laser multiheterodyne optical coherence tomography", Opt. Lett. **33**, 2092–2094 (2008).

[44] J. Pupeikis, B. Willenberg, C. P. Bauer, S. L. Camenzind, A. Nussbaum-Lapping, C. R. Phillips, and U. Keller, "Single-cavity dual-comb yb: yag laser operating at 250 mhz with ultra-low noise", in Conference on lasers and electro-optics/europe (cleo) and european quantum electronics conference (eqec) (2023), pp. 1–1.

[45] S. A. Carp, D. Tamborini, D. Mazumder, K.-C. Wu, M. B. Robinson, K. A. Stephens, O. Shatrovoy, N. Lue, N. Ozana, M. H. Blackwell, and M. A. Franceschini, "Diffuse correlation spectroscopy measurements of blood flow using 1064 nm light", J. Biomed. Opt. **25**, 097003–097003 (2020).

[46] D. Contini, F. Martelli, and G. Zaccanti, "Photon migration through a turbid slab described by a model based on diffusion approximation. i. theory", Applied optics **36**, 4587–4599 (1997).

[47] A. M. Goldfain, P. Lemaillet, D. W. Allen, K. A. Briggman, and J. Hwang, "Polydimethylsiloxane tissue-mimicking phantoms with tunable optical properties", J. Biomed. Opt. **27**, 074706–074706 (2022).

[48] N. B. Hébert, V. Michaud-Belleau, J.-D. Deschênes, and J. Genest, "Self-correction limits in dual-comb interferometry", IEEE J. Quantum Electron. **55**, 1–11 (2019).

[49] D. J. Pine, D. A. Weitz, P. M. Chaikin, and E. Herbolzheimer, "Diffusing wave spectroscopy", Phys. Rev. Lett. **60**, 1134 (1988).

[50] D. A. Boas, S. Sakadžić, J. Selb, P. Farzam, M. A. Franceschini, and S. A. Carp, "Establishing the diffuse correlation spectroscopy signal relationship with blood flow", Neurophotonics **3**, 031412–031412 (2016).

[51] B. Aernouts, E. Zamora-Rojas, R. Van Beers, R. Watté, L. Wang, M. Tsuta, J. Lammertyn, and W. Saeys, "Supercontinuum laser based optical characterization of intralipid® phantoms in the 500-2250 nm range", Opt. Express **21**, 32450–32467 (2013).

[52] C. Chen, J. Q. Lu, H. Ding, K. M. Jacobs, Y. Du, and X.-H. Hu, "A primary method for determination of optical parameters of turbid samples and application to intralipid between 550 and 1630nm", Opt. Express **14**, 7420–7435 (2006).

[53] G. M. Hale and M. R. Querry, "Optical constants of water in the 200-nm to 200-μm wavelength region", Appl. Opt. **12**, 555–563 (1973).

3

3

FREQUENCY-MODULATED SCATTERING HOLOGRAPHY DETERMINES OPTICAL PROPERTIES OF TURBID MEDIA

Speckle-based flow (SBF) techniques are widely used for non-invasive monitoring of cerebral blood flow, yet their accuracy is often limited by the need for independent measurement of tissue optical properties. While time-domain near-infrared spectroscopy (TD-NIRS) can provide these optical parameters, integration with SBF systems typically results in low signal-to-noise ratio (SNR) due to inefficient speckle collection. To overcome this limitation, we introduce frequency-modulated scattering holography (FMSH) capable of quantifying the optical properties of turbid media. FMSH utilizes a highly parallel, interferometric detection architecture with photon-counting sensitivity, enabling robust measurement of absorption and scattering coefficients. This approach provides a compact and integrated solution that addresses the limitations of conventional systems, offering a pathway to improved tissue characterization in neurophotonics and related biomedical imaging applications.

Parts of this chapter have been published in https://doi.org/10.1364/opticaopen.30576617

3.1. INTRODUCTION

Optical detection with photon-counting sensitivity is indispensable for a broad spectrum of applications, ranging from ultra-long-distance imaging[1–3] and non-line-of-sight imaging[4–6] to quantum computation[7–9] and diverse bioimaging modalities, including fluorescence microscopy[10, 11], single-molecule spectroscopy[12, 13], and speckle-based blood flow (SBF) measurements. In SBF, coherent laser illumination of biological tissue generates scattered photons that interfere, forming a random interference pattern known as speckle[14]. Laser speckle contrast imaging (LSCI)[15–18] leverages low-frame-rate cameras to observe speckle blurring caused by dynamic scatterers. However, its sensitivity is limited to superficial layers due to photon backscattering. To probe deeper, increasing the source-detector (SD) distance allows access to deeper tissue, with specificity at approximately half the SD distance[19]. Techniques like speckle contrast optical spectroscopy (SCOS)[20, 21], diffuse correlation spectroscopy (DCS)[19, 22], and laser Doppler perfusion monitoring (LDPM)[23, 24] rely on large SD separations, leading to low photon throughput and requiring expensive detectors such as SPADs[25, 26] and SNSPDs[27, 28].

Time-of-flight (ToF)-dependent methods like time-domain DCS[29–31] and interferometric diffuse optics (iDO)[32–35] improve depth sensitivity without large SD separations. In particular, single-speckle iDO, including iNIRS[32] and DC-DWS[35], achieves ToF-resolved measurements by using heterodyne detection with swept sources or dual-comb lasers. These systems can extract depth-dependent optical properties such as absorption (μ_a) and reduced scattering (μ_s') coefficients. However, single-speckle iDOs suffer from limited signal-to-noise ratio (SNR), even when operating at the shot-noise limit (see Appendix 3.5.2). Multiple-speckle iDO addresses this limitation by harnessing numerous pixels to enhance photon throughput. In SBF measurements, the speckle size corresponds to the maximum coherence area over which photons coherently interfere. Previous work[33] have demonstrated that collecting multiple speckles onto a single detector increases the collected power but simultaneously reduces the mutual coherence factor, ultimately failing to improve the SNR. A similar phenomenon occurs in frequency-modulated light scattering interferometry (FMLSI)[36, 37]. This limitation can be mitigated by employing a detector array to spatially separate individual speckles. By averaging across N independent detection channels, the SNR is improved by a factor of $\sqrt{N}$. Interferometric diffusing wave spectroscopy (iDWS)[33, 38] implements this concept by collecting multiple speckles through a multimode fiber and projecting them onto a high-speed (> 100 kHz) line camera, where each pixel functions as an independent DWS channel. This parallelized detection scheme provides higher SNR while maintaining cost efficiency by using CMOS cameras. Another approach, interferometric speckle visibility spectroscopy (iSVS)[34, 39, 40], also employs multimode fiber collection but operates at a lower frame rate (100 Hz). Although this frame rate is slower than the typical decorrelation times of scattered electric fields, the speckle visibility factor enables the extraction of electric-field decorrelation dynamics. However, both iDWS and iSVS typically rely on large SD separations, which limit spatial resolution and reduce their ability to effectively measure DTOF compared to iNIRS or DC-DWS. Nevertheless, iDWS represents a cost-effective method for implementing multi-channel diffuse correlation spectroscopy (DCS) without requiring an extensive array of single-photon detec-

tors[41].

In principle, merging iNIRS-like approaches with camera-based detection could combine the advantages of time-resolved measurements and multi-speckle parallelization. However, the high detection bandwidth required poses a significant challenge[42]. For example, if one considers the beat frequency

$$f_{\text{beat}} = \frac{2B\tau}{T} \tag{3.1}$$

where a triangular modulation is assumed, with B the modulated optical bandwidth, τ the time-of-flight (ToF) difference between reference and sample arm and T the modulation period. A modest modulation speed ($1/T = 100\ kHz$) combined with a gigahertz-scale optical bandwidth ($B = 20\ GHz$) and nanosecond-scale T ($= 2\ ns$) can yield a beat frequency ($f_{\text{beat}} = 8\ MHz$) beyond current camera detection limits.

More recently, a tunable ToF gate has been introduced into iDWS by employing a tunable laser[43, 44], allowing photons within a certain coherence range to interfere, while out-of-range photons manifest as background noise. This technique selectively enhances sensitivity to deeper layers, but fails to reconstruct the full DTOF. To overcome these limitations, we propose a new technique termed frequency-modulated scattering holography (FMSH). FMSH employs a Mach-Zehnder interferometer using a frequency-modulated external cavity diode laser (ECDL) and a CMOS camera. By drastically reducing the modulation frequency (e.g., 200 Hz), the beat frequency for nanosecond-scale ToF differences (e.g., 2 ns) falls within a detectable kilohertz range (e.g., 16 kHz), enabling ToF-resolved measurement using affordable, fast CMOS cameras.

This setup allows each pixel to record the interferogram between the reference beam and multiply scattered light. In the frequency domain, the signal encodes a Doppler-broadened distribution of time-of-flight (DB-DTOF) for dynamic media, where spectral components are naturally separated by ToF, or pure DTOF for static media. As such, FMSH allows for recovery of the full DTOF, enabling extraction of optical properties without large SD separations and at high spatial resolution. Compared to existing ToF techniques, FMSH offers a simplified, high-throughput, and cost-effective platform for non-invasive tissue characterization.

3.2. METHODS

3.2.1. FMSH INSTRUMENTATION

Figure 3.1 illustrates the experimental setup for frequency-modulated holography used to measure optical properties of turbid media. The system employs an external cavity laser diode (ECDL, New Focus Velocity 6300) with a central wavelength of 633 nm, modulated by a waveform generator producing a waveform with a 200 Hz ramp. The 5 mW output beam passes through an optical isolator (OI) and is then split by a variable beam splitter (VBS). The reflection from the first surface of the VBS is collimated to form a fiber Mach-Zehnder interferometer with a 2 m fiber delay, which is used to determine the modulation optical bandwidth (19.8 GHz in this work). The reflection from the second surface is directed by two mirrors (M1 and M2) and expanded by a Powell lens (PL) to illuminate a rectangular pixel area. The transmitted beam, with 3 mW power, illuminates the turbid media, and the diffused light passes through a pinhole before interfering

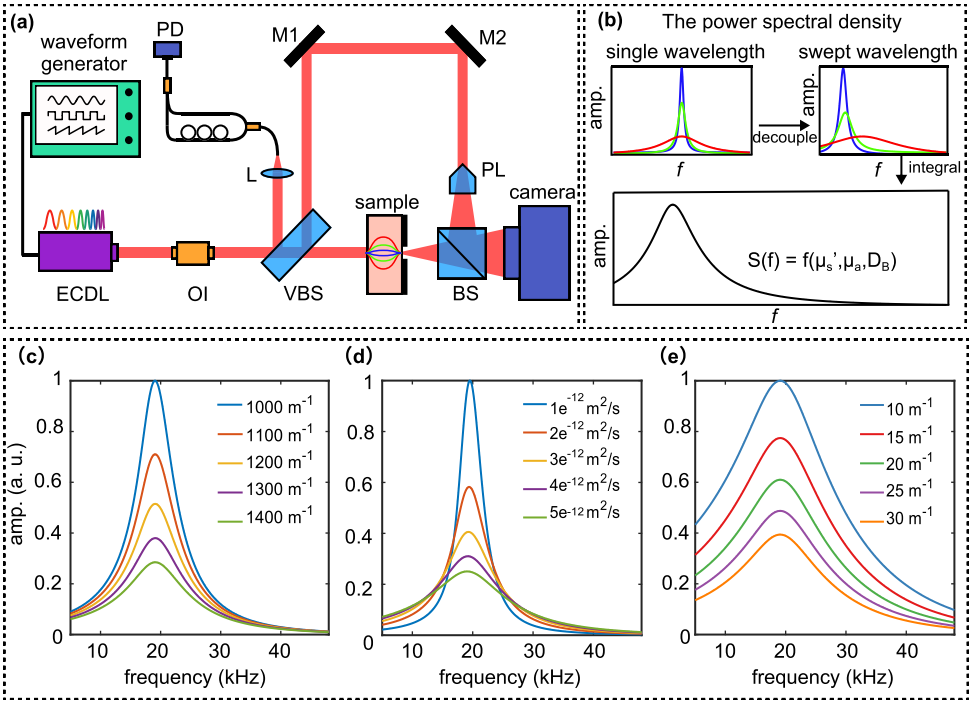

Figure 3.1: Schematic diagram elaborating on the concept of frequency-modulated holography. (a) Two frequency-modulated interferometers work as reference and measurement respectively. ECDL–external cavity diode laser, OI–optical isolator, VBS–variable beam splitter, M1, M2–mirror, L–lens, PL–Powell lens, BS–beam splitter, SFC–single-mode fiber coupler, PD–photodetector; (b) Frequency-modulated source decouples the path-length dependent Doppler spectrum according to their times-of-flight (beat frequency f); (c) FMSH signals at different values of the reduced scattering coefficient (μ_s' = 1000–1400 m^{-1}, in steps of 100 m^{-1}) for fixed absorption coefficient (μ_a = 50 m^{-1}) and Brownian coefficient ($D_B = 5\times10^{-12} m^2/s$); (d) FMSH signals at different values of Brownian coefficient (D_B = 1 - $5\times10^{-12} m^2/s$, in steps of $1\times10^{-12} m^2/s$) for fixed absorption coefficient (μ_a = 50 m^{-1}) and reduced scattering coefficient(μ_s' = 1600 m^{-1}); (e) FMSH signals at different values of the absorption coefficient (μ_a = 10–50 m^{-1}, in steps of 5 m^{-1}) for fixed scattering coefficient (μ_s' = 1600 m^{-1}) and Brownian coefficient ($D_B = 5\times10^{-12} m^2/s$).

with the reference beam on a high-speed camera (Photron Fastcam SA3) operating at a 100 kHz frame rate for a 16 × 256 pixel region.

3.2.2. THE DTOF OF STATIC MEDIA

To derive the DTOF, we begin by considering a single scattering path. For an individual pixel of the camera, the temporal interferogram (IGM) count level is given by:

$$
\begin{aligned}
N(s,t) &= \frac{\gamma \delta t}{e_{\mathrm{ph}}}\{P_{\mathrm{LO}}(t) + P_{\mathrm{s}}(s,t) + 2\kappa\sqrt{P_{\mathrm{LO}}(t)P_{\mathrm{s}}(s,t)}\cos[2\pi f_{\mathrm{s}} t + \varphi_{\mathrm{s}}(t)] \\
&= N_{\mathrm{LO}}(t) + N_{\mathrm{s}}(s,t) + 2\kappa\sqrt{N_{\mathrm{LO}}(t)N_{\mathrm{s}}(s,t)}\cos[2\pi f_{\mathrm{s}} t + \varphi_{\mathrm{s}}(t)] \\
&= N_{\mathrm{dc}}(t) + N_{\mathrm{ac}}(s,t)
\end{aligned} \tag{3.2}
$$

where $P_{\mathrm{LO}}(t)$ and $P_{\mathrm{s}}(s,t)$ correspond to the power from the local oscillator (LO) and the scattering path s of the sample respectively. $N_{\mathrm{dc}}(t) = N_{\mathrm{LO}}(t) + N_{\mathrm{s}}(s,t)$ is the direct current (DC) component, $N_{\mathrm{LO}}(t) = \gamma P_{\mathrm{LO}}(t)\delta t / e_{\mathrm{ph}}$ is the count level from the LO, $N_{\mathrm{s}}(s,t) = \gamma P_{\mathrm{s}}(s,t)\delta t / e_{\mathrm{ph}}$ is the count level from scattering path s of the sample, and is below one count in the extremely short camera exposure time so can be neglected here. $N_{\mathrm{ac}}(s,t)$ denotes the alternating current (AC) component. The term κ and γ represent the mutual coherence and the quantum efficiency of the camera respectively, δt is the exposure time of the camera, and e_{ph} denotes the energy of a single photon. In addition, f_{s} represents the beat frequency, and $\varphi_{\mathrm{s}}(t)$ is the phase difference between the LO and the scattering path.

For static media, the scatters remain still and do not introduce phase shift during a long measurement time (i.e. φ_{s} is constant over measurement time). After subtracting the DC component and performing the Fourier transform, the positive frequency band is expressed as

$$
\begin{aligned}
\mathscr{F}^{+}\{N_{\mathrm{ac}}(s,t)\} &= \mathscr{F}\{\kappa\sqrt{N_{\mathrm{LO}}(t)N_{\mathrm{s}}(s,t)}\exp[2\pi f_{\mathrm{s}} t + \varphi_{\mathrm{s}}(t)]\} \\
&= \kappa^2 N_{\mathrm{LO}}(t)N_{\mathrm{s}}(s,t)\delta(f - f_{\mathrm{s}})
\end{aligned} \tag{3.3}
$$

where $N_{\mathrm{s}}(s,t)$ is given by photon diffusion theory in transmission or reflectance geometry[45].

3.2.3. THE DOPPLER-BROADENED DTOF OF DYNAMIC MEDIA

For dynamic media, in an iNIRS system, the wavelength modulation speed is significantly higher than the characteristic timescales of scatterer dynamics, effectively rendering the scatterers "frozen" during each modulation cycle. Consequently, the phase difference $\varphi_{\mathrm{s}}(t)$ between the two arms remains constant, leading to the emergence of a sharp delta peak in the Fourier domain. In contrast, in the present study, the modulation speed is considerably lower than the characteristic scatterer dynamics, necessitating explicit consideration of phase variations. The difference in Doppler effect between iNIRS and this work can also be explained in the perspective of frequency resolution (see Appendix 3.5.1). The power spectrum of the positive frequency band is expressed as:

$$
\begin{aligned}
S(s,f^{+}) &= |\mathscr{F}^{+}\{N_{\mathrm{ac}}(s,t)\}|^2 \\
&= |\mathscr{F}\{\kappa\sqrt{N_{\mathrm{LO}}(t)N_{\mathrm{s}}(s,t)}\exp[2\pi f_{\mathrm{s}} t + \varphi_{\mathrm{s}}(t)]\}|^2 \\
&= \kappa^2 N_{\mathrm{LO}}(t)N_{\mathrm{s}}(s,t)\delta(f - f_{\mathrm{s}}) \otimes D(s,f)
\end{aligned} \tag{3.4}
$$

where $D(s,f) = |\mathscr{F}\{\exp[\varphi_{\mathrm{s}}(t)]\}|^2$ represents the Doppler spectrum of the scattering path s where the particles undergo Brownian motion. Equation (3) shows that the Doppler

spectrum is shifted by the beat frequency f_s:

$$S(s, f^+) = \kappa^2 N_{LO}(t) N_s(s, t) D(s, f - f_s) \tag{3.5}$$

Following the framework of DWS, and because autocorrelation and PSD are connected by the Wiener–Khinchin theorem, the Doppler power spectral density from the scattering path s is defined as:

$$D(s, f) = |\mathscr{F}[g_1(s, \tau)]| = \frac{2C_s}{C_s^2 + (2\pi f)^2} \tag{3.6}$$

where the parameter C_s is given by:

$$C_s = 2k_0^2 \mu_s' D_B s \tag{3.7}$$

As a result, in comparison to iNIRS, the delta peak is broadened by the Doppler spectrum, and relative to iDWS, the Doppler spectrum of different scattering path undergoes a frequency shift corresponding to the beat frequency f_s, which represents the ToF of scattered photons. Note that despite the relatively low modulation speed, the camera frame rate is sufficiently high to capture both the beat frequency and the Doppler spectrum. The complete broadened DTOF is given by:

$$S(f^+) = \int_0^{+\infty} S(s, f^+) ds = \int_0^{+\infty} \frac{2\kappa^2 N_{LO}(t) N_s(s, t) C_s}{C_s^2 + [2\pi(f - f_s)]^2} ds \tag{3.8}$$

Equation 3.8 demonstrates that the final broadened DTOF is influenced by three key optical and dynamical parameters: the reduced scattering coefficient (μ_s'), the absorption coefficient (μ_a), and the Brownian diffusion coefficient (D_B). Figure 3.1 (c)-(e) illustrates the effects of each parameter on the FMSH signals. Specifically, both the reduced scattering coefficient and the Brownian coefficient contribute to temporal broadening of the DTOF profile. This overlap in their influence leads to a challenge in decoupling and independently quantifying μ_s' and D_B from the measured signals, as discussed in detail in Appendix 3.5.2. In contrast, the absorption coefficient primarily affects the amplitude of the DTOF by attenuating the overall signal intensity, without significantly altering the shape of the temporal profile compared with μ_s'.

3.3. RESULTS

To validate the FMSH model, we conducted controlled experiments using both static and dynamic tissue-mimicking phantoms. The static phantom was fabricated from polydimethylsiloxane (PDMS) mixed with titanium dioxide (TiO_2) as the scattering agent and carbon powder (CP) as the absorber, following established formulations for tuning the optical properties [46]. The dynamic phantom was prepared by diluting a 20 % Intralipid emulsion with deionized water to generate a suspension of lipid particles undergoing Brownian motion, thereby simulating moving scatterers in biological tissue. Both phantoms has a uniform thickness of 10 mm and mounted in the optical path for measurements in a transmission geometry, with illumination and detection positioned on opposite sides of the sample (zero source-detection separation, as shown in Figure 3.1 (a)).

3.3.1. STATIC PHANTOM

For static phantom measurements, the DTOF curves were obtained by first computing the Fourier transform of the temporal intensity signal at each pixel, followed by averaging the resulting amplitudes across all pixels to enhance the signal-to-noise ratio and mitigates the impact of non-ergodicity in static samples [35, 47], owing to the advantages of multi-speckle detection [48]. A reference measurement, acquired without sample, was used to determine the instrument response function (IRF), which exhibited a full width at half maximum (FWHM) of 231 ps and defined the temporal resolution of the system (Figure 3.2 (a)). This resolution could be further improved by correcting frequency modulation non-linearity if necessary. In the experiment, two sets of static samples were used: the first consisted of PDMS mixed with varying fractions of TiO_2 to adjust the reduced scattering coefficient, while the second consisted of PDMS with a fixed concentration of TiO_2 and varying amounts of CP to adjust the absorption coefficient. The measured DTOFs are presented in Figures 3.2(b) and 3.2(c) and were fitted using Equation (3.3) convolved with the measured IRF. The μ_s' and μ_a values extracted from the measurements show good agreement with those reported in [46] (Figures 3.2(e) and 3.2(f)).

3.3.2. DYNAMIC PHANTOM

For the dynamic phantom, the measured distribution of time-of-flight (DTOF) curve was obtained by averaging the power spectral density over all pixel time traces. The power spectral density was calculated from the amplitude square of the Fourier transform of each pixel's temporal signal. Before squaring, noise correction was essential to prevent the distortion of the spectral shape by the cross-terms between the optical signal and noise. In our measurements, the shot noise level was significantly higher than the camera noise (including readout and quantization components). To correct for this, we first recorded the reference beam without the sample, measured the noise floor for each pixel, and subtracted it from the corresponding signal before computing the spectra (Figure 3.2 (g)).

The corrected DTOF data were fitted using the theoretical Doppler-broadened DTOF convolved with the experimentally determined IRF (more details see Appendix 3.5.4). As discussed in Section 3.2.3, the Brownian diffusion coefficient D_B and the reduced scattering coefficient μ_s' could not be independently determined from the fits; we therefore extracted D_B using a fixed, independently measured μ_s', and conversely extracted μ_s' using a fixed D_B . The results, shown in Figure 3.2 (h), reveal that D_B decreases with increasing Intralipid concentration, which we attribute to the corresponding increase in viscosity. The fitted D_B values are consistent with those reported in previous studies (4–6.8 $\times e^{-12}$ m2/s) [36], and the measured μ_s' values are in good agreement with prior work [49] (Figure 3.4 (i)).

3.4. CONCLUSION AND DISCUSSION

In this chapter, we introduced Frequency-Modulated Scattering Holography (FMSH), a novel interferometric technique for characterizing the optical properties of turbid media with high spatial resolution and sensitivity. FMSH employs frequency-modulated

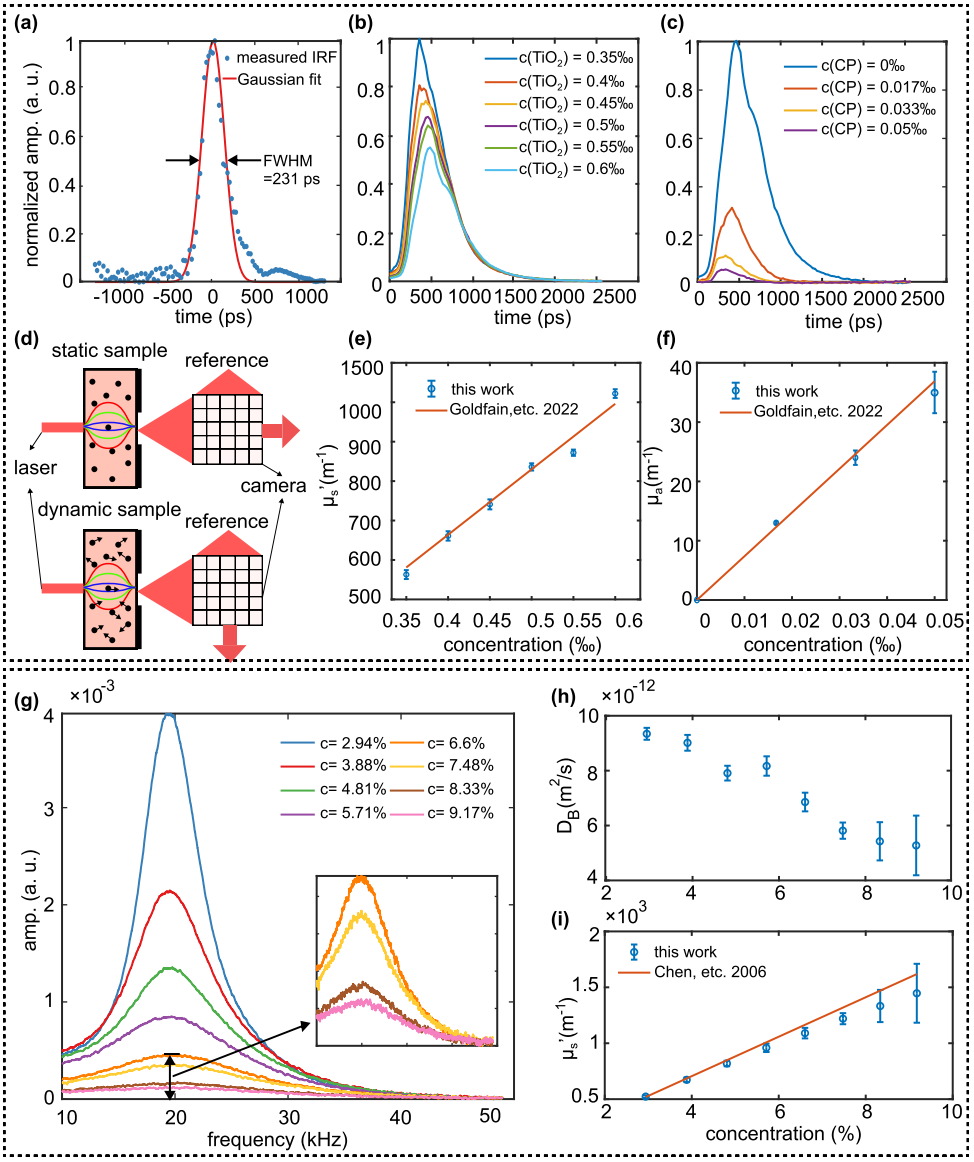

Figure 3.2: Measurement results for static and dynamic samples. (a) Measured instrument response function (IRF) and corresponding Gaussian fit; (b) DTOF curves for varying TiO_2 concentrations; (c) DTOF curves for varying carbon powder (CP) concentrations; (d) Schematic diagram of the static and dynamic sample configurations; (e–f) Fitted results compared with values reported in [46]; (g) Processed data for different Intralipid concentrations; (h) Fitting of the Brownian diffusion coefficient D_B using known reduced scattering coefficients μ_s'; D_B decreases with increasing Intralipid concentration; (i) Fitting of μ_s' using known D_B; results are consistent with previous studies.

laser illumination and multi-speckle interferometric detection to retrieve both the distributed of time-of-flight (DTOF) and its Doppler-broadened counterpart (DB-DTOF). By substantially reducing the modulation frequency compared with conventional iNIRS systems, FMSH shifts the beat frequency into a range detectable by fast CMOS cameras, enabling low-cost and scalable implementations.

We demonstrated that FMSH can extract the reduced scattering coefficient (μ_s') and absorption coefficient (μ_a) from static scattering media, as well as μ_s' and the Brownian diffusion coefficient (D_B) from dynamic media when one parameter is known. Simulations revealed that μ_s' and D_B affect the DTOF in a similar manner, producing a characteristic "banana-shaped" region in the fitting error map. While the global minimum can be identified under noise-free conditions, realistic noise significantly limits the simultaneous determination of both parameters, underscoring a fundamental constraint of the method.

A detailed signal-to-noise ratio (SNR) analysis compared FMSH with other interferometric diffuse optics techniques, including DC-DWS, iNIRS, and photon-counting approaches. Theoretical modeling indicated that FMSH achieves shot-noise-limited performance superior to photon-counting methods; however, in practice, its sensitivity is constrained by the photon-detection threshold of the CMOS camera. The analysis further suggests that employing more sensitive cameras—with lower full-well capacity or higher analog gain—could bring FMSH closer to its theoretical SNR limit. The modular architecture of FMSH also permits straightforward extension to time-gated measurements and depth-resolved functional imaging, offering strong potential for compact and portable diffuse optical tomography systems.

Several challenges remain. The inability to reliably separate μ_s' and D_B under noisy conditions may be addressed through multi-wavelength measurements, exploiting the wavelength dependence of μ_s' and the wavelength independence of D_B. Furthermore, the high frame rates and large-scale parallel detection generate substantial data throughput, posing challenges for real-time processing. Finally, the clinical translation of FMSH will require the development of miniaturized, motion-tolerant implementations, which remains an active area of research.

In summary, FMSH represents a promising direction for high-sensitivity, high-resolution, and cost-effective diffuse optical measurements. By integrating interferometric precision with parallel speckle detection and frequency-domain encoding, it offers a pathway toward bridging the gap between photon-efficient interferometric diffuse optics and practical, scalable spatially-resolved implementations.

3.5. APPENDIX

3.5.1. THE DOPPLER EFFECT COMPARISON

In iNIRS and FMSH, the influence of the Doppler effect manifests differently in the frequency domain, owing to their distinct temporal resolutions. The Doppler spectrum corresponding to each scattering path s is described by the Lorentzian function:

$$D(s,f) = \frac{2C_s}{C_s^2 + [2\pi(f - f_s)]^2} \tag{3.9}$$

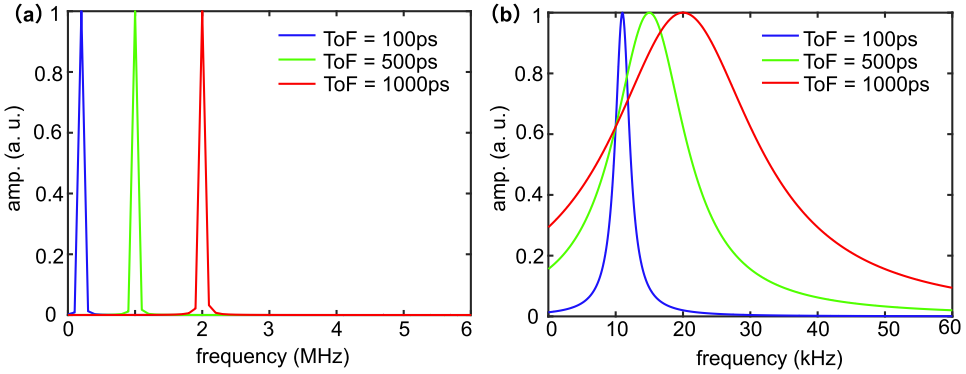

Figure 3.3: The normalized Doppler spectrum of 100 ps, 500 ps and 1000 ps in iNIRS and FMSH according to equation (3.9). $\mu_s = 1000m^{-1}$, $D_B = 1 \times 10^{-12} m^2/s$, $f_0 = 10$ kHz. **(a)** The short data acquisition time results in low frequency resolution and eliminates the Doppler effect in iNIRS. (b)The longer data acquisition time results in higher frequency resolution, which shows Doppler broadening effects in FMSH.

where $f_s = f_0 + \beta s$, and the frequency shift coefficient β is given by $\beta = \frac{2nBs}{Tc}$. Here, f_0 arises from the path-length difference between the reference and sample arms, B is the modulation bandwidth, T is the frequency ramp modulation period, and c is the speed of light in vacuum. The scattering path length s is related to ToF via $s = c \cdot ToF/n$, with the refractive index n taken to be 1.37. The spectral broadening parameter C_s, reflecting the Doppler width, is expressed as $C_s = 2k_0^2 \mu_s' D_B s$, where $k_0 = \frac{2\pi}{633nm}$, μ_s' is the reduced scattering coefficient and D_B is the diffusion coefficient of particles. Since the particles undergo Brownian motion, the Doppler spectra for forward and backward frequency sweeps are symmetric, and the data acquisition time is set equal to frequency modulation period T.

In the case of iNIRS, the modulation period is $T_{iNIRS} = 1/(100 \times 10^3)$ seconds, resulting in a frequency resolution of $\delta f_{iNIRS} = 1/T_{iNIRS} = 100$ kHz. This resolution is significantly larger than the typical Doppler spectral width C_s, rendering the Doppler-induced broadening effectively unresolvable in the frequency domain. Consequently, the Doppler effect does not manifest visibly in the iNIRS spectrum, as shown in Figure 3.3 (a).

Conversely, in FMSH, the modulation period is extended to $T_{iNIRS} = 1/500$ seconds, yielding a much finer frequency resolution of $\delta f_{FMSH} = 1/T_{FMSH} = 500$ Hz. Since this resolution is substantially smaller than C_s, the Doppler spectrum is clearly resolved in the frequency domain, as illustrated in Figure 3.3 (b).

3.5.2. THE FITTING ERROR MAP OF μ_s' AND D_B

The similar broadening effects caused by the reduced scattering coefficient (μ_s') and the Brownian diffusion coefficient (D_B) pose a significant challenge for accurately separating these parameters through curve fitting. To illustrate this, we performed a simulation to generate a FMSH signal using ground-truth values of $D_B = 5 \times 10^{-12} \mathrm{m}^2/\mathrm{s}$, $\mu_s' = 1000 \mathrm{m}^{-1}$, and $\mu_a = 10\ \mathrm{m}^{-1}$, as shown in Figure 3.4(b). By fixing μ_a, we constructed a fitting error map across a grid of D_B and μ_s' values. The result reveals a characteristic 'banana-shaped' low-error region, within which the errors are similar, although a clear

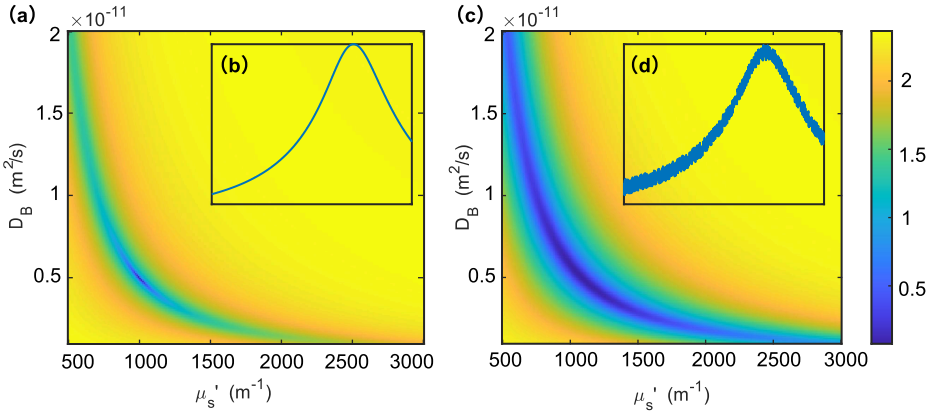

Figure 3.4: Fitting error map of the Doppler-broadened DTOF with fixed absorption coefficient (μ_a). (a) Ideal noise-free data shows a global minimum in the error surface, though the error values remain low across the "banana-shaped" region; (b) The fitting data for simulated data with $D_B = 5e^{-12} m^2/s$, $\mu_s^{'} = 1000 m^{-1}$ and $\mu_a = 10 m^{-1}$; (c) When random noise is added to the ideal data, the error surface becomes flatter within the banana region, making it difficult to distinguish between $\mu_s^{'}$ and D_B. (d) The fit data with 10% added noise.

global minimum remains identifiable at the true parameter values.

However, when 10% random noise is added to the simulated signal, as shown in Figure 3.4(d), the distinction in error values across the banana region becomes negligible. This loss of contrast in the error surface obscures the global minimum, making it difficult to recover the correct D_B and $\mu_s^{'}$ through fitting. This highlights a fundamental limitation in the accurate determination of these parameters under realistic noise conditions.

3.5.3. SIGNAL-TO-NOISE RATIO COMPARISON

In interferometric diffuse optics (iDO), the signal-to-noise ratio (SNR) is the bottleneck that limits its clinical application. Here, we compare the SNR of dual-comb diffusing-wave spectroscopy (DC-DWS)[35], interferometric near-infrared spectroscopy (iNIRS)[50], and photon-counting approaches[51].

DUAL-COMB INTERFEROMETER

In DC-DWS, the local oscillator scans the photon distribution of time-of-flight (DTOF) thereby recording the interferogram (IGM) in the time domain. For a mirror object, the peak current of the IGM is given by:

$$i_p = 2\kappa\eta\sqrt{P_{LO}P_s} \tag{3.10}$$

where κ is the mutual coherence between the sample and the local oscillator (LO), η is represents the response (A/W) of the photo detector, P_{LO} is the power of the LO power and P_s is the power reflected from the object. The noise comes from the photo detector and the quantum limitation of optical measurement

$$\sigma_{noise}{}^2 = \sigma_d^2 + \sigma_{sn}^2 = NEP^2 \cdot B + 2qBi \tag{3.11}$$

where σ_d^2 is the photodetector noise, σ_{sn}^2 is the shot noise, NEP is the noise-equivalent power of the photodetector, B is the detection bandwidth, q is the electron charge, $i = \eta(P_{LO} + P_s + 2\sqrt{P_{LO}P_s})$ is the current. Increasing the power of LO, $P_{LO} \gg 2\sqrt{P_{LO}P_s} \gg P_s$, and $\sigma_{sn}^2 \gg \sigma_d^2$, therefore, the shot-noise-limited SNR is given by:

$$SNR_{DC-DWS} = \frac{i_p^2}{{\sigma_{noise}}^2} = \frac{2\kappa^2\eta P_s}{qB} = \frac{2\kappa^2\eta P_{cl}}{q\Delta f_{rep}} \tag{3.12}$$

where $P_s = mP_{cl}$, $B = m\Delta f_{rep}$, m is the comb line number,P_{cl} is the power of single comb line, and Δf_{rep} is the difference in the repetition frequency between the two comb lasers. The measurement time can be regarded as $1/\Delta f_{rep}$, therefore for the dual-comb interferometer, the final shot-noise-limited SNR is decided by the collected power $(P_{cl}/\Delta f_{rep})$ from a single comb line rather than the whole comb spectrum. Let m = 100, $\eta = 0.9$, $\kappa = 1/\sqrt{2}$, $\Delta f_{rep} = 100$ kHz (typical speed to measure blood flow), and $SNR = 2$, then we have minimal detectable power

$$(P_s)_{min} = m(P_{cl})_{min} = m\frac{q\Delta f_{rep}}{\kappa^2\eta} = 3.56 \times 10^{-12} W \tag{3.13}$$

If the wavelength is 780nm, the photon flux is 13.96 Mph/s.

FREQUENCY-MODULATED INTERFEROMETER

Similarly, in iNIRS, the LO interferes with photons with different ToFs. The amplitude of sinusoidal oscillation of IGM from a mirror object is given by equation (3.14), and the noise is given by equation (3.15). The difference is that for iNIRS, the signal is presented in the frequency domain. Assuming data acquisition time T is long enough, the signal is coherently integrated and after the Fourier transform it is given by

$$\begin{aligned} |S(f)| &= |\mathscr{F}^+\{i_p(t)\}|^2 \\ &= \kappa^2\eta^2 P_{LO}P_s\delta^2(f - f_0) + \kappa^2\eta^2 P_{LO}P_s\delta^2(f + f_0) \end{aligned} \tag{3.14}$$

where $i_p(t) = 2\eta T\sqrt{P_{LO}P_s}\cos(2\pi f_0 t)$ is the beat signal. The power of shot noise is separated for each frequency component (double sideband spectrum $2B$) and is given by

$$\sigma_{sn}^2(f) = 2qBi \times \frac{\delta f}{2B} = \frac{qi}{T} \tag{3.15}$$

The shot-noise-limited SNR of iNIRS is given by

$$SNR_{iNIRS} = \frac{\kappa^2\eta^2 P_{LO}P_s}{qi/t_a} = \frac{\kappa^2\eta P_s T}{q} \tag{3.16}$$

Equation (3.16) shows that the shot-noise-limited SNR of iNIRS depends on collected energy $(P_s t)$ during measurement time T. For a same measurement time $(1/\delta f_{rep} = T)$ responsivity of photodetector, (η), and collected power from sample (P), $\frac{SNR_{iNIRS}}{SNR_{DC-DWS}} = m/2$, the minimal detected power is

$$(P_s)_{min} = \frac{2q}{\kappa^2\eta t_a} = 7.12 \times 10^{-14} W \tag{3.17}$$

If the wavelength is 780nm, the photon flux is 279 kph/s. As a result, iNIRS has a 17 dB SNR advantage over DC-DWS.

PHOTON-COUNTING APPROACHES

In photon-counting approaches we consider a pulsed laser illuminating a mirror like object and a photon-counting detector being used to detect the faint signals. For dark count $DCR = 250$, and a 0.2 quantum efficiency (PDM, Micro Photon Devices), the minimum detectable photon flux is $2DCR/\eta = 2500$ ph/s.

FREQUENCY-MODULATED HOLOGRAPHY

For frequency-modulated holography, the beat signal is given by

$$\begin{aligned} N_{\mathrm{ac}}(t) &= \frac{2\kappa\gamma\sqrt{P_{\mathrm{s}}P_{\mathrm{LO}}}\delta t}{e_{\mathrm{ph}}}\cos(2\pi f_0 t) \\ &= 2\kappa\sqrt{N_{\mathrm{s}}N_{\mathrm{LO}}}\cos(2\pi f_0 t) \end{aligned} \tag{3.18}$$

where γ is the quantum efficiency of the camera, κ is the mutual coherence between LO and photons reflected from the sample, $\delta t = 1/f_{\mathrm{s}}$ is the exposure time, f_{s} is the frame rate, and e_{ph} is the energy of single photon. $N_{\mathrm{LO}} = \gamma P_{\mathrm{s}}\delta t/e_{\mathrm{ph}}$, $N_{\mathrm{s}} = \gamma P_{\mathrm{s}}\delta t/e_{\mathrm{ph}}$ is the electron charge of pixel from LO and reflected photons respectively. This can be further converted to the digital count of pixels

$$C_{\mathrm{ac}}(t) = \frac{2\kappa\sqrt{N_{\mathrm{s}}N_{\mathrm{LO}}}}{\mathrm{CF}}\cos(2\pi f_0 t) \tag{3.19}$$

where CF = full well capacity/$2^{\text{bit depth}}$ is the coversion factor of the camera. The shot noise in analog-to-digital unit (ADU) is given by:

$$\sigma_{\mathrm{sn}}^2 = \frac{N_{\mathrm{dc}}}{\mathrm{CF}^2} = \frac{N_{\mathrm{LO}}}{\mathrm{CF}^2} \tag{3.20}$$

The total camera noise consists of readout noise and quantization noise. The readout noise, originating from the camera electronics, has a variance of σ_{r}^2 in units of electrons, and $\sigma_{\mathrm{r}}^2/\mathrm{CF}^2$ in ADU. The quantization noise has a variance of σ_{q}^2 =1/12 in ADU[52]. In this work, With a high camera CF, increasing the reference power near saturation ensures $\sigma_{\mathrm{sn}}^2 \gg \sigma_{\mathrm{r}}^2 + \sigma_{\mathrm{q}}^2$, achieving shot-noise-limited operation.

After Fourier transform, the squared positive peak is given by $|S(f^+)| = \kappa^2 N_{\mathrm{s}} N_{\mathrm{LO}}/\mathrm{CF}^2$, and the shot noise of each bin is $\sigma_{sn}(f)^2 = \frac{N_{\mathrm{LO}}}{\mathrm{CF}^2} \times \frac{\delta f}{2B}$, where $2B = 1/\delta t$ and $\delta f = 1/T$, T is the measurement time. Then the final SNR is given by

$$\begin{aligned} SNR_{\mathrm{FMH}} &= \sqrt{n}\frac{|S(f^+)|}{\sigma_{sn}(f)^2} = \sqrt{n}\frac{\kappa^2 N_{\mathrm{s}} T}{\delta t} \\ &= \sqrt{n}\frac{\kappa^2 T}{\delta t} \times \frac{\gamma P_{\mathrm{s}}\delta t}{e_{\mathrm{ph}}} \\ &= \sqrt{n}\kappa^2 N_{\mathrm{s}}^{\mathrm{T}} \end{aligned} \tag{3.21}$$

where n is the pixel number and $N_{\mathrm{s}}^{\mathrm{T}}$ is the electron charge from sample during the measurement time T. In this work, 4096 pixels are used, and T =1/200 s, κ^2 =1/2, γ = 0.36 for 633 nm, then let SNR=2, minimal photon flux is 34.7 ph/s.

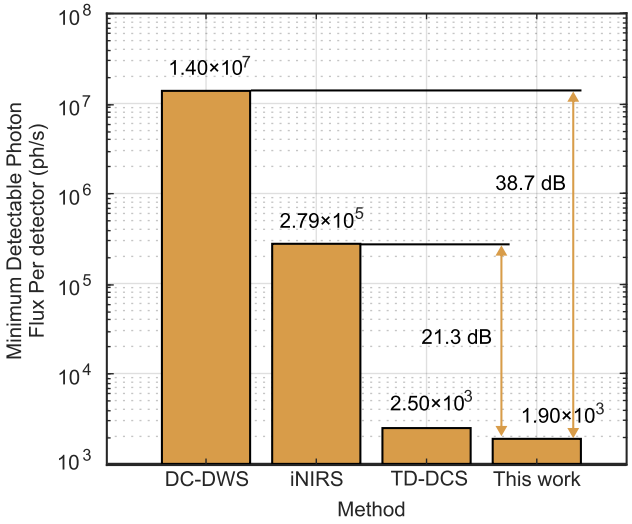

Figure 3.5: The minimum detectable photon flux per detector comparison of different methods: dual-comb interferometer in DC-DWS, frequency-modulated interferometer in iNIRS, photon-counting approach in TD-DCS, and frequency-modulated holography in this work.

On the other hand, the minimum photon flux is also limited by the photon sensitivity threshold of the camera. To detect the beat signal, the amplitude of the AC component should be larger than at least 2 counts in grey level. Then

$$\frac{2\kappa\sqrt{N_s N_{LO}}}{\mathrm{CF}} = 2\kappa\sqrt{\frac{N_s}{\mathrm{CF}}C_{LO}} > 2 \tag{3.22}$$

where $C_{LO} = N_s/\mathrm{CF}$ is the mean gray level of LO at camera and we also get

$$\Phi_{\min} = \frac{N_s}{\gamma\delta t} > \frac{\mathrm{CF}}{\gamma\kappa^2 C_{LO}\delta t} \tag{3.23}$$

For the camera used here full well capacity = $42000e^-$ and the bit depth is 12, and let $\mathrm{Count}_{LO} = 3000$, $\delta t = 1/(100\times10^3)s$, then the minimum detectable photon flux per pixel is 1898 ph/s (0.6 fW in power). The difference between equations (3.21) and (3.23) arises primarily from the use of different effective exposure times: T for the shot-noise-limited SNR, and δt for the camera threshold. Then we choose 1898 ph/s as the minimum detectable photon flux per detector, which is comparable to the photon-counting approach. Therefore, current SNR is limited by the photon sensitivity threshold of camera rather than shot noise. From equation (3.23) we know that choosing a more sensitive camera (e. g. lower CF) will help to arrive at shot-noise-limited SNR.

3.5.4. THE DOPPLER-BROADEND DTOF FITTING

The acquisition time for each measurement was 1 s, during which 100 k frames per pixel were recorded for both the interferogram and the reference arm. For each pixel's tempo-

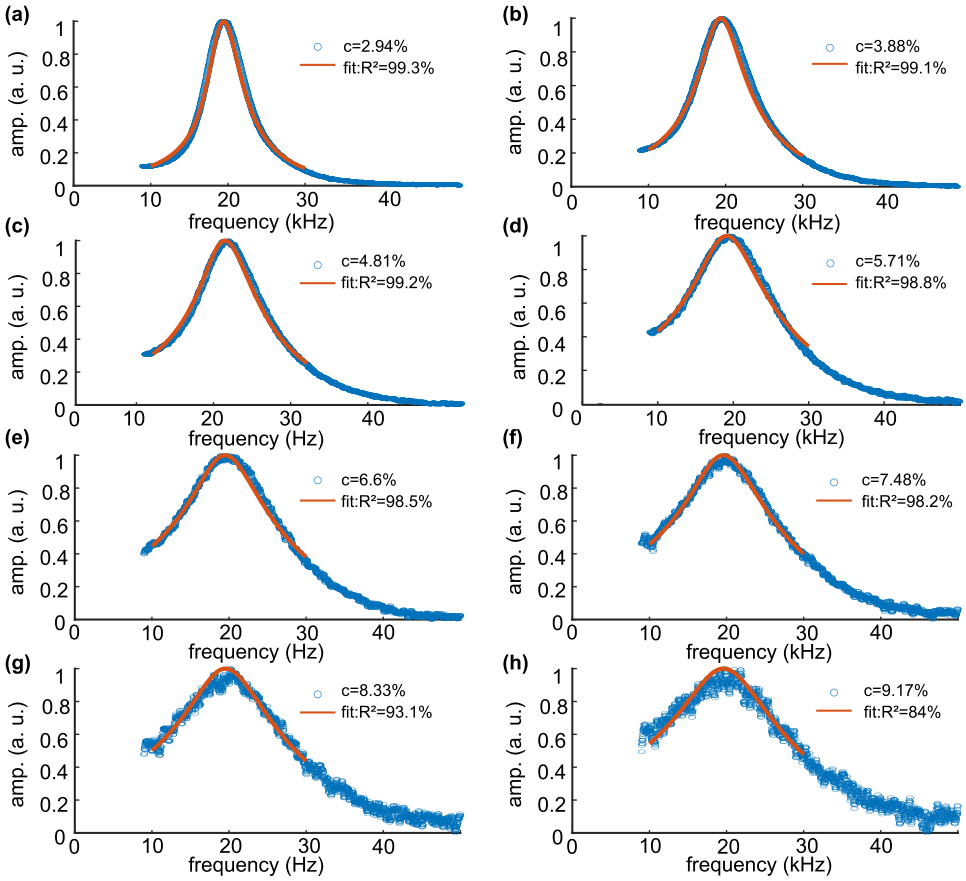

Figure 3.6: Processed power density spectra and corresponding model fits for samples with Intralipid concentrations ranging from 2.94% to 9.17% (a–h). The measured spectra (dots) agree well with the theoretical model (solid lines), demonstrating how increasing particle concentration broadens the spectral width and raises the initial amplitude.

ral signal, a Fourier transform was applied to obtain its spectral components. The corresponding shot noise limited spectrum was determined from the reference arm measurement, and then subtracted from the measured signal spectrum to remove noise contributions prior to squaring. The squared amplitudes yielded the power density spectra. Peaks arising from the periodic frequency modulation of the laser were subsequently removed by spectral filtering, and the resulting spectra were normalized to obtain the measured power density spectra (dots in Figure 3.7(a)–(h)). The experimental data were fitted using the theoretical model, convolved with the instrument response function (IRF), applied to 50 % of the spectral range. As the Intralipid concentration increased, the coefficient of determination (R^2) for the fits systematically decreased, reflecting the reduced signal-to-noise ratio (SNR) at higher scattering levels.

BIBLIOGRAPHY

[1] A. McCarthy, N. J. Krichel, N. R. Gemmell, X. Ren, M. G. Tanner, S. N. Dorenbos, V. Zwiller, R. H. Hadfield, and G. S. Buller, "Kilometer-range, high resolution depth imaging via 1560 nm wavelength single-photon detection", Optics express **21**, 8904–8915 (2013).

[2] J. Tachella, Y. Altmann, N. Mellado, A. McCarthy, R. Tobin, G. S. Buller, J.-Y. Tourneret, and S. McLaughlin, "Real-time 3d reconstruction from single-photon lidar data using plug-and-play point cloud denoisers", Nature communications **10**, 4984 (2019).

[3] Z.-P. Li, J.-T. Ye, X. Huang, P.-Y. Jiang, Y. Cao, Y. Hong, C. Yu, J. Zhang, Q. Zhang, C.-Z. Peng, et al., "Single-photon imaging over 200 km", Optica **8**, 344–349 (2021).

[4] D. Faccio, A. Velten, and G. Wetzstein, "Non-line-of-sight imaging", Nature Reviews Physics **2**, 318–327 (2020).

[5] C. Wu, J. Liu, X. Huang, Z.-P. Li, C. Yu, J.-T. Ye, J. Zhang, Q. Zhang, X. Dou, V. K. Goyal, et al., "Non–line-of-sight imaging over 1.43 km", Proceedings of the National Academy of Sciences **118**, e2024468118 (2021).

[6] X. Huang, R. Ye, W. Li, J.-W. Zeng, Y.-C. Lu, H. Hu, Y. Zhou, L. Hou, Z.-P. Li, H.-F. Jiang, et al., "Non-line-of-sight imaging and vibrometry using a comb-calibrated coherent sensor", Physical Review Letters **132**, 233802 (2024).

[7] H.-S. Zhong, H. Wang, Y.-H. Deng, M.-C. Chen, L.-C. Peng, Y.-H. Luo, J. Qin, D. Wu, X. Ding, Y. Hu, et al., "Quantum computational advantage using photons", Science **370**, 1460–1463 (2020).

[8] C. Couteau, S. Barz, T. Durt, T. Gerrits, J. Huwer, R. Prevedel, J. Rarity, A. Shields, and G. Weihs, "Applications of single photons to quantum communication and computing", Nature Reviews Physics **5**, 326–338 (2023).

[9] N. Maring, A. Fyrillas, M. Pont, E. Ivanov, P. Stepanov, N. Margaria, W. Hease, A. Pishchagin, A. Lemaitre, I. Sagnes, et al., "A versatile single-photon-based quantum computing platform", Nature Photonics **18**, 603–609 (2024).

[10] W. Denk, J. H. Strickler, and W. W. Webb, "Two-photon laser scanning fluorescence microscopy", Science **248**, 73–76 (1990).

[11] M. Y. Berezin and S. Achilefu, "Fluorescence lifetime measurements and biological imaging", Chemical reviews **110**, 2641–2684 (2010).

[12] W. E. Moerner, "Single-molecule spectroscopy, imaging, and photocontrol: foundations for super-resolution microscopy (nobel lecture)", Angewandte Chemie International Edition **54**, 8067–8093 (2015).

[13] L.-M. Needham, C. Saavedra, J. K. Rasch, D. Sole-Barber, B. S. Schweitzer, A. J. Fairhall, C. H. Vollbrecht, S. Wan, Y. Podorova, A. J. Bergsten, et al., "Label-free detection and profiling of individual solution-phase molecules", Nature **629**, 1062–1068 (2024).

[14] J. W. Goodman, *Speckle phenomena in optics: theory and applications* (Roberts and Company Publishers, 2007).

[15] P. Li, S. Ni, L. Zhang, S. Zeng, and Q. Luo, "Imaging cerebral blood flow through the intact rat skull with temporal laser speckle imaging", Optics letters **31**, 1824–1826 (2006).

[16]D. A. Boas and A. K. Dunn, "Laser speckle contrast imaging in biomedical optics", Journal of biomedical optics **15**, 011109–011109 (2010).

[17]A. K. Dunn, "Laser speckle contrast imaging of cerebral blood flow", Annals of biomedical engineering **40**, 367–377 (2012).

[18]J. Senarathna, A. Rege, N. Li, and N. V. Thakor, "Laser speckle contrast imaging: theory, instrumentation and applications", IEEE reviews in biomedical engineering **6**, 99–110 (2013).

[19]T. Durduran, R. Choe, W. B. Baker, and A. G. Yodh, "Diffuse optics for tissue monitoring and tomography", Reports on progress in physics **73**, 076701 (2010).

[20]R. Bandyopadhyay, A. Gittings, S. Suh, P. Dixon, and D. J. Durian, "Speckle-visibility spectroscopy: a tool to study time-varying dynamics", Review of scientific instruments **76** (2005).

[21]C. P. Valdes, H. M. Varma, A. K. Kristoffersen, T. Dragojevic, J. P. Culver, and T. Durduran, "Speckle contrast optical spectroscopy, a non-invasive, diffuse optical method for measuring microvascular blood flow in tissue", Biomedical optics express **5**, 2769–2784 (2014).

[22]T. Durduran and A. G. Yodh, "Diffuse correlation spectroscopy for non-invasive, microvascular cerebral blood flow measurement", Neuroimage **85**, 51–63 (2014).

[23]R. Lohwasser and G. Soelkner, "Experimental and theoretical laser-doppler frequency spectra of a tissuelike model of a human head with capillaries", Applied optics **38**, 2128–2137 (1999).

[24]A. Humeau, W. Steenbergen, H. Nilsson, and T. Strömberg, "Laser doppler perfusion monitoring and imaging: novel approaches", Medical & biological engineering & computing **45**, 421–435 (2007).

[25]E. J. Sie, H. Chen, E.-F. Saung, R. Catoen, T. Tiecke, M. A. Chevillet, and F. Marsili, "High-sensitivity multispeckle diffuse correlation spectroscopy", Neurophotonics **7**, 035010–035010 (2020).

[26]W. Liu, R. Qian, S. Xu, P. Chandra Konda, J. Jönsson, M. Harfouche, D. Borycki, C. Cooke, E. Berrocal, Q. Dai, et al., "Fast and sensitive diffuse correlation spectroscopy with highly parallelized single photon detection", APL Photonics **6** (2021).

[27]N. Ozana, A. I. Zavriyev, D. Mazumder, M. Robinson, K. Kaya, M. Blackwell, S. A. Carp, and M. A. Franceschini, "Superconducting nanowire single-photon sensing of cerebral blood flow", Neurophotonics **8**, 035006–035006 (2021).

[28]V. Parfentyeva, L. Colombo, P. Lanka, M. Pagliazzi, A. Brodu, N. Noordzij, M. Kolarczik, A. Dalla Mora, R. Re, D. Contini, et al., "Fast time-domain diffuse correlation spectroscopy with superconducting nanowire single-photon detector: system validation and in vivo results", Scientific Reports **13**, 11982 (2023).

[29]J. Sutin, B. Zimmerman, D. Tyulmankov, D. Tamborini, K. C. Wu, J. Selb, A. Gulinatti, I. Rech, A. Tosi, D. A. Boas, et al., "Time-domain diffuse correlation spectroscopy", Optica **3**, 1006–1013 (2016).

[30]M. Pagliazzi, S. K. V. Sekar, L. Colombo, E. Martinenghi, J. Minnema, R. Erdmann, D. Contini, A. D. Mora, A. Torricelli, A. Pifferi, et al., "Time domain diffuse correlation spectroscopy with a high coherence pulsed source: in vivo and phantom results", Biomedical optics express **8**, 5311–5325 (2017).

[31]D. Tamborini, K. A. Stephens, M. M. Wu, P. Farzam, A. M. Siegel, O. Shatrovoy, M. Blackwell, D. A. Boas, S. A. Carp, and M. A. Franceschini, "Portable system for time-domain diffuse correlation spectroscopy", IEEE Transactions on Biomedical Engineering **66**, 3014–3025 (2019).

[32]D. Borycki, O. Kholiqov, S. P. Chong, and V. J. Srinivasan, "Interferometric near-infrared spectroscopy (inirs) for determination of optical and dynamical properties of turbid media", Optics express **24**, 329–354 (2016).

[33]W. Zhou, O. Kholiqov, S. P. Chong, and V. J. Srinivasan, "Highly parallel, interferometric diffusing wave spectroscopy for monitoring cerebral blood flow dynamics", Optica **5**, 518–527 (2018).

[34]J. Xu, A. K. Jahromi, J. Brake, J. E. Robinson, and C. Yang, "Interferometric speckle visibility spectroscopy (isvs) for human cerebral blood flow monitoring", Apl Photonics **5** (2020).

[35]B. Zhang, C. Phillips, E. Venialgo Araujo, S. Iskander-Rizk, J. Pupeikis, B. Willenberg, U. Keller, and N. Bhattacharya, "Study of time-resolved dynamics in turbid medium using a single-cavity dual-comb laser", ACS Photonics (2024).

[36]L. Mei, S. Svanberg, and G. Somesfalean, "Frequency-modulated light scattering in colloidal suspensions", Applied Physics Letters **102** (2013).

[37]L. Mei, G. Somesfalean, and S. Svanberg, "Frequency-modulated light scattering interferometry employed for optical properties and dynamics studies of turbid media", Biomedical Optics Express **5**, 2810–2822 (2014).

[38]W. Zhou, O. Kholiqov, J. Zhu, M. Zhao, L. L. Zimmermann, R. M. Martin, B. G. Lyeth, and V. J. Srinivasan, "Functional interferometric diffusing wave spectroscopy of the human brain", Science Advances **7**, eabe0150 (2021).

[39]J. Xu, A. K. Jahromi, and C. Yang, "Diffusing wave spectroscopy: a unified treatment on temporal sampling and speckle ensemble methods", Apl Photonics **6** (2021).

[40]Y. X. Huang, S. Mahler, J. Mertz, and C. Yang, "Interferometric speckle visibility spectroscopy (isvs) for measuring decorrelation time and dynamics of moving samples with enhanced signal-to-noise ratio and relaxed reference requirements", Optics Express **31**, 31253–31266 (2023).

[41]G. Dietsche, M. Ninck, C. Ortolf, J. Li, F. Jaillon, and T. Gisler, "Fiber-based multispeckle detection for time-resolved diffusing-wave spectroscopy: characterization and application to blood flow detection in deep tissue", Applied optics **46**, 8506–8514 (2007).

[42]S. Samaei, K. Nowacka, A. Gerega, Ż. Pastuszak, and D. Borycki, "Continuous-wave parallel interferometric near-infrared spectroscopy (cw π nirs) with a fast two-dimensional camera", Biomedical Optics Express **13**, 5753–5774 (2022).

[43] M. Zhao, W. Zhou, S. Aparanji, D. Mazumder, and V. J. Srinivasan, "Interferometric diffusing wave spectroscopy imaging with an electronically variable time-of-flight filter", Optica **10**, 42–52 (2023).

[44] M. Zhao, L. Dickstein, A. S. Nadig, W. Zhou, S. Aparanji, H. G. Estrada, S.-J. Liu, T. Zhou, W. Yang, A. Lord, et al., "Comprehensive optimization of interferometric diffusing wave spectroscopy (idws)", IEEE Journal of Selected Topics in Quantum Electronics (2025).

[45] D. Contini, F. Martelli, and G. Zaccanti, "Photon migration through a turbid slab described by a model based on diffusion approximation. i. theory", Applied optics **36**, 4587–4599 (1997).

[46] A. M. Goldfain, P. Lemaillet, D. W. Allen, K. A. Briggman, and J. Hwang, "Polydimethylsiloxane tissue-mimicking phantoms with tunable optical properties", J. Biomed. Opt. **27**, 074706–074706 (2022).

[47] R. Samanta, D. Mazumder, O. Kholiqov, and V. J. Srinivasan, "Dynamic speckle-modulated interferometric near-infrared spectroscopy of non-ergodic samples", in Optics and the brain (Optica Publishing Group, 2025), BW1B–2.

[48] J. Guzman-Sepulveda, R. Argueta-Morales, W. DeCampli, and A. Dogariu, "Real-time intraoperative monitoring of blood coagulability via coherence-gated light scattering", Nature Biomedical Engineering **1**, 0028 (2017).

[49] C. Chen, J. Q. Lu, H. Ding, K. M. Jacobs, Y. Du, and X.-H. Hu, "A primary method for determination of optical parameters of turbid samples and application to intralipid between 550 and 1630nm", Opt. Express **14**, 7420–7435 (2006).

[50] D. Borycki, O. Kholiqov, S. P. Chong, and V. J. Srinivasan, "Interferometric near-infrared spectroscopy (inirs) for determination of optical and dynamical properties of turbid media", Optics express **24**, 329–354 (2016).

[51] J. Sutin, B. Zimmerman, D. Tyulmankov, D. Tamborini, K. C. Wu, J. Selb, A. Gulinatti, I. Rech, A. Tosi, D. A. Boas, et al., "Time-domain diffuse correlation spectroscopy", Optica **3**, 1006–1013 (2016).

[52] W. F. Sheppard, "On the calculation of the most probable values of frequency-constants, for data arranged according to equidistant division of a scale", Proceedings of the London Mathematical Society **1**, 353–380 (1897).

4

4

FREQUENCY-MODULATED SCATTERING HOLOGRAPHY DETERMINES DYNAMIC PROPERTIES OF TURBID MEDIA

Accurate quantification of cerebral blood flow requires highly sensitive detection of dynamic light scattering in turbid biological tissue. Conventional speckle-based flow (SBF) methods suffer from low signal-to-noise ratio (SNR) due to limited speckle collection, while high-parallel detection architectures improve SNR but rely on long source–detector separations, which reduce spatial resolution and photon throughput. Here, we introduce frequency-modulated scattering holography (FMSH), a technique that overcomes these trade-offs by enabling depth-resolved measurement of dynamic scattering with photon-counting sensitivity. By integrating frequency-domain modulation with massively parallel detection, FMSH achieves sensitive and high-resolution characterization of dynamics in complex scattering environments. This approach opens new avenues for high-resolution and high-sensitivity, non-invasive imaging of cerebral hemodynamics.

Parts of this chapter have been published in https://doi.org/10.1364/opticaopen.30576617

4.1. INTRODUCTION

The characterization of tissue dynamics—especially blood flow—is crucial for neuroscience[1, 2], oncology[3, 4], dermatology[5, 6] and surgery[7, 8]. Conventional techniques for dynamic measurement, such as speckle contrast optical spectroscopy (SCOS) [9, 10], diffuse correlation spectroscopy (DCS)[11], and laser Dopper perfusion (LDP)[12, 13] analyze speckle blurring, intensity autocorrelation, or power spectral density to infer motion of scatterers. However, to measure dynamics in deep tissue, such as cerebral blood flow (CBF), these techniques require a long source–detector (SD) separation to reduce the influence of shallow layers. This, in turn, limits spatial resolution, and photon throughput decreases exponentially with increasing SD separation.

Interferometric diffuse optics (iDO) have introduced new possibilities. In single-speckle implementations, interferometric near-infrared spectrosocpy (iNIRS)[14] and dual-comb diffusing-wave spectroscopy (DC-DWS) [15] provide access to field autocorrelation decay rates and photon distribution of time-of-flight (DTOF) via time-resolved detection, allowing estimation of the blood flow index (BFi) and optical properties. However, their SNR is limited due to single-channel detection. Multiple-speckle iDO, such as iDWS[16] and iSVS[17], improves SNR through spatial multiplexing, with iDWS operating at >100 kHz for electric-field autocorrelation and iSVS enabling dynamic readout via speckle visibility contrast at 100 Hz.

Recent enhancements to iDWS include coherence gating with tunable laser sources [18], which selectively improves sensitivity to specific time-of-flight (ToF) ranges and thus to deeper flows. However, this approach requires careful optimization of the optical path difference (OPD) and the laser's swept optical bandwidth [19], limiting its flexibility.

To address these limitations, this chapter introduces frequency-modulated scattering holography (FMSH). Using low-speed modulation of an external cavity diode laser (ECDL, 200 Hz), FMSH generates beat signals in the kHz range that encode nanosecond-scale ToF differences. Each pixel records a temporal interferogram whose frequency-domain representation contains Doppler power spectra broadened by scatterer dynamics along each optical path and shifted according to their respective ToFs. By integrating the power spectral density (PSD) across pixels, a heterodyne speckle hologram is reconstructed. Applying band-pass filters to the PSD yields ToF-resolved speckle contrasts, effectively functioning as coherence gates. This enables separation of dynamic components by depth, allowing depth-resolved flow measurements even at small source–detector separations. Unlike approaches that require ultrafast electronics or photon-counting detectors, FMSH achieves photon-counting sensitivity with high-parallel detection using low-cost, camera-based hardware.

4.2. METHODS

4.2.1. INSTRUMENTATION

The instrumentation used is identical to that described in chapter 3.2.1. In this chapter, we demonstrate the concept using a reflectance geometry. The sample consists of a two-layer turbid medium: the top layer is made of polydimethylsiloxane (PDMS) mixed with carbon powder and titanium dioxide, mimicking the optical properties of human tissue[20] ($\mu_s' = 1022 m^{-1}$, $\mu_a = 24 m^{-1}$) and has a 5 mm thickness; the bottom layer is

a solution of Intralipid mixed with water (10 mm thickness, $\mu_s^{'} = 1090m^{-1}$). A syringe pump is used to modulate the flow rate at 0.5 Hz (Figure 4.1 (a)).

4.2.2. ToF-DEPENDENT SPECKLE CONTRAST

In iDWS and parallel iNIRS[21], the high measurement speed allows direct capture of the field autocorrelation to infer dynamics. In contrast, FMSH operates at a measurement rate slower than the scatterers' decorrelation time. However, its use of parallel detection with a camera not only boosts photon throughput but also provides an additional advantage—it enables the calculation of speckle contrast, which is related to dynamics.

The integral of the full PSD (equation (3.8)) yields a quantity proportional to the signal energy, reflecting intensity fluctuations over the measurement window T

$$\begin{aligned} I(T) &= \int_{f_{\text{down}}}^{f_{\text{up}}} \int_0^{+\infty} \frac{2\kappa^2 < N_{\text{LO}}(t) N_s(s,t) >_T C_s}{C_s^2 + [2\pi(f - f_s)]^2} ds df \\ &= \int_0^{+\infty} \kappa^2 < N_{\text{LO}}(t) N_s(s,t) >_T \int_{f_{\text{down}}}^{f_{\text{up}}} \frac{2C_s}{C_s^2 + [2\pi(f - f_s)]^2} df ds \\ &= \kappa^2 < N_{\text{LO}}(t) >_T \int_0^{+\infty} < N_s(s,t) >_T ds = \kappa^2 < N_{\text{LO}}(t) >_T < N_s(t) >_T \end{aligned} \tag{4.1}$$

Here f_{up} and f_{down} denote the frequency bounds encompassing the full Doppler spectrum, and $< N_{\text{LO}}(t) >_T$, $< N_s(s,t) >_T$ represent the time-averaged counts from the local oscillator and each scattering path s over the acquisition window. $< N_s(t) >_T$ is the time-averaged counts from all paths. Assuming that the LO power remains constant during T, we have

$$\begin{aligned} I(T) &= \kappa^2 N_{\text{LO}}(t) < N_s(t) >_T \\ &= \frac{\kappa^2 N_{\text{LO}}(t)}{T} \int_0^T N_s(t) dt \end{aligned} \tag{4.2}$$

The contrast computed from this integrated intensity yields the same result as that obtained by conventional SCOS methods[9]

$$\begin{aligned} K^2(T) &= \frac{< [I(T) - < I(T) >]^2 >}{< I(T) >^2} \\ &= \frac{\{\int_0^T [N_s(t) - < N_s(t) >] dt\}^2}{< \int_0^T N_s(t) dt >^2} \\ &= \frac{2\beta}{T} \int_0^T (1 - \frac{\tau}{T}) g_1^2(\tau) d\tau \end{aligned} \tag{4.3}$$

where $g_1(\tau)$ denotes the field autocorrelation function, and β is a coherence factor that accounts for the spatial and temporal coherence properties of the detection system. Here, the measurement window T is equivalent to the exposure time in SCOS.

Differing from conventional SCOS, the swept source and the high frame rate of the camera decouples the Doppler spectrum of each scattering path according to its own ToF. This provides the opportunity to measure the dynamics at different depths. Specifically, by integrating over a selected frequency band, the system effectively implements

a band-pass filter (BF) that acts as a ToF gate, selectively capturing photon energies associated with specific path lengths. The ToF-dependent speckle contrast can be written as

$$K^2_{\mathrm{BF}}(T) = \frac{< [I_{\mathrm{BF}}(T) - < I_{\mathrm{BF}}(T) >]^2 >}{< I_{\mathrm{BF}}(T) >^2} = \frac{\sigma^2_{\mathrm{BF}}(T)}{< I_{\mathrm{BF}}(T) >^2} \tag{4.4}$$

where $I_{\mathrm{BF}}(T)$ denotes the integrated intensity after applying a BP filter to the PSD. This approach exploits the fact that photons with short ToF primarily contribute to the low-frequency region of the PSD (Figure 4.1(b)). In contrast, photons with longer ToFs generate broader Doppler spectra because of the larger number of scattering encounters. By selecting the higher-frequency components, contributions from shallow dynamics can be effectively suppressed. Consequently, the specificity to deep flow scales with the ratio of the partial path length (PPL) in the deep layer (layer 2) relative to that in the superficial layer (layer 1)

$$\mathrm{spec(BF)} = \frac{\alpha_2 D_{\mathrm{B2}} \mu_{s2}^{'} \overline{l_2(\mathrm{BF})}}{\alpha_1 D_{\mathrm{B1}} \mu_{s1}^{'} \overline{l_1(\mathrm{BF})}} \tag{4.5}$$

where α_1 and α_2 is the dynamic scattering ratio in layer 1 and layer 2; D_{B1} and D_{B2} is the diffusion coefficient in layer 1 and layer 2; $\mu_{s1}^{'}$ and $\mu_{s2}^{'}$ is the reduced scattering coefficient of layer 1 and layer 2; l_1 and l_2 is the partial path length in layer 1 and layer 2. The longer ToF has a higher partial path length ratio in deep layer (see Appendix 4.5.1 for more details), therefore this ToF-gated speckle contrast provides a higher specificity to deep flow.

4.2.3. DATA PROCESSING

The camera operates at a frame rate much higher than the optical frequency modulation, so within each modulation period each pixel records a temporal interferogram (IGM, Figure 4.1(b)). Frequency modulation also introduces intensity modulation, which is removed by normalizing with its envelope (Figure 4.1(c)). First the interferogram is Fourier transformed, then the shot noise from the reference arm is subtracted and the the power spectral density (PSD) is extracted after squaring. In the temporal–frequency domain, the DC component $N_{\mathrm{LO}}(t) + N_{\mathrm{s}}(t)$ and the AC component are separated, analogous to spatial–frequency domain in off-axis holography where the DC and AC terms are also separate. The time-of-flight (ToF) information is encoded across the entire PSD. Integrating the AC component of the PSD for each pixel reconstructs a speckle hologram, similar to SCOS but in a heterodyne form. To suppress shallow-layer contributions and enhance specificity to deeper layers, a bandpass filter is applied (Figure 4.1(d)), yielding a ToF-resolved speckle hologram from which ToF-dependent speckle contrast can be calculated (Figure 4.1(e)). The full processing pipeline is summarized in Figure 4.1(f).

4.3. RESULTS

The two-layer phantom consisted of a 5-mm-thick static layer (μ_s' = 1000 m^{-1}, μ_a = 50 m^{-1}) and a 10-mm-thick dynamic Intralipid layer (μ_s' = 2000 m^{-1}). The speckle contrast can be determined from the DB-DTOF. This approach was experimentally validated

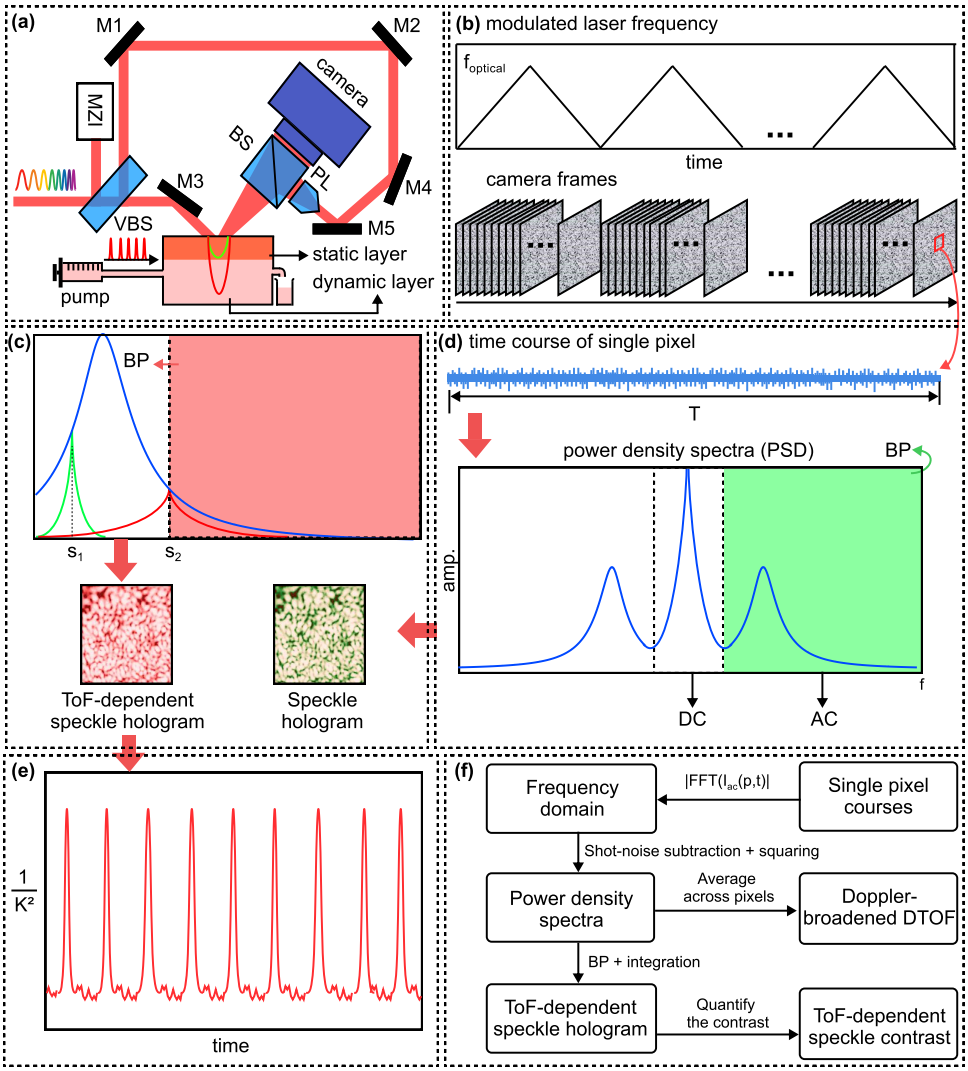

Figure 4.1: Schematic diagram for determining the dynamic properties of turbid media using FMSH. (a) The external cavity diode laser (ECDL) output is split into a reference arm and a measurement arm. In the measurement arm, the laser illuminates the sample, and the backscattered photons are collected directly in free space by the camera pixels. The source-detector separation is set to 0 cm. A syringe pump is used to modulate the flow rate of the Intralipid-water mixture in the second layer of the sample. MZI-Mach-Zehnder-interferometer, M1-M4-mirror, VBS-variable beam splitter, BS-beam splitter, PL-Powell lens; (b) The optical frequency of the ECDL is modulated by a ramp waveform at 100–200 Hz. With the camera operating at a frame rate of 120 kHz, each modulation period yields 600–1000 frames. (c) Each pixel records a time series over the acquisition period T. After applying a Fourier transform and squaring the result, the power density spectrum (PDS) is obtained, allowing separation of DC and AC components. (d) By applying a bandpass (BP) filter to either the full PDS or the PDS corresponding to photons with longer time-of-flight (ToF), speckle holography for all scattered photons or depth-resolved speckle holography can be obtained. (e) By calculating the ensemble speckle contrast over time, the flow modulation driven by the syringe pump can be reconstructed. (f) A diagram of the FMSH data processing procedure is shown.

using both a homogeneous Intralipid phantom with configuration shown in Fig. 3.1 (a) and the two-layer tissue-mimicking phantom with configuration shown in Fig. 4.1 (a).

For the homogeneous phantom measured in the transmission geometry, the averaged DB-DTOF is shown in Fig. 4.2(a). A series of band-pass filters (BPFs) was applied to the DB-DTOF of each pixel, where the upper cutoff frequency (f_{up}) was held constant, while the lower cutoff frequency (f_{lower}) was progressively increased starting from the frequency corresponding to zero time-of-flight (ToF) lag. The zero ToF lag was calibrated by removing the sample to measure the optical path-length difference between the reference and sample arms. The speckle contrast (K^2) was then calculated according to Eq. (4.3), and is shown in Fig. 4.2(c).

The mean K^2 decreases with increasing f_{lower} in the range between f_{l1} and f_{l2}. This behavior can be attributed to the homogeneous dynamic phantom, in which the increase of the dynamic scattering events is approximately linear with the photon ToF, leading to faster temporal decorrelation and consequently lower speckle contrast. For $f_{\text{lower}} > f_{l2}$, K^2 increases due to the reduced signal-to-noise ratio between the dynamic signal and shot noise.

For the two-layer phantom measured, in reflectance geometry, the first layer consists of static scatterers, while the second layer consists of dynamic scatterers driven by a syringe pump, simulating pulsatile flow. By averaging the PSD over all camera pixels, a DB-DTOF was obtained, as shown in Fig. 4.2(b). A similar BPF strategy was applied to the DB-DTOF of each pixel, with a fixed f_{up} and an increasing f_{lower} starting from zero ToF lag.

As shown in Fig. 4.2(d), in contrast to the homogeneous dynamic phantom, the mean K^2 initially increases with increasing f_{lower} until reaching f_{l1}. This behavior indicates that Doppler spectrum leakage from the deeper dynamic layer vanishes below f_{l1}: interference signal measured within this frequency range does not carry dynamic information or the SNR is too low to be detected. Consequently, the filtered intensity variance $\sigma^2_{\text{BF}}(T)$ remains approximately constant, while the mean intensity $\langle I_{\text{BF}}(T)\rangle$ decreases due to the narrowing filter bandwidth, as described by Eq. (4.4).

Between f_{l1} and f_{l2}, the detected signal consists of contributions from purely static scattering paths as well as photons leaking from the dynamic layer due to Doppler broadening. In this regime, the mean K^2 decreases rapidly. For $f_{l2} < f_{\text{lower}} < f_{l3}$, photons with longer ToF accumulate a larger fraction of their partial path length in the deeper dynamic layer, resulting in faster temporal decorrelation and a further reduction in K^2. For $f_{\text{lower}} > f_{l3}$, K^2 increases again due to the degradation of SNR, similar to the static case.

The temporal evolution of $1/K^2$ under different BPF settings was also evaluated for the two-layer phantom, as shown in Fig. 4.2(e). All BPF configurations consistently captured the periodic modulation induced by the syringe pump (Fig. 4.2(f)), although narrower BPFs exhibited reduced SNR. This can be seen from Fig. 4.2(f) upper panel with lower SNR and lower panel with higher SNR showing that the sensitivity to depth can be increased by choice of the BPF. The Fourier transforms of $1/K^2$, in both cases successfully recovered the pump modulation frequency of 0.5 Hz, as shown in Fig. 4.2(g) and Fig. 4.2(h).

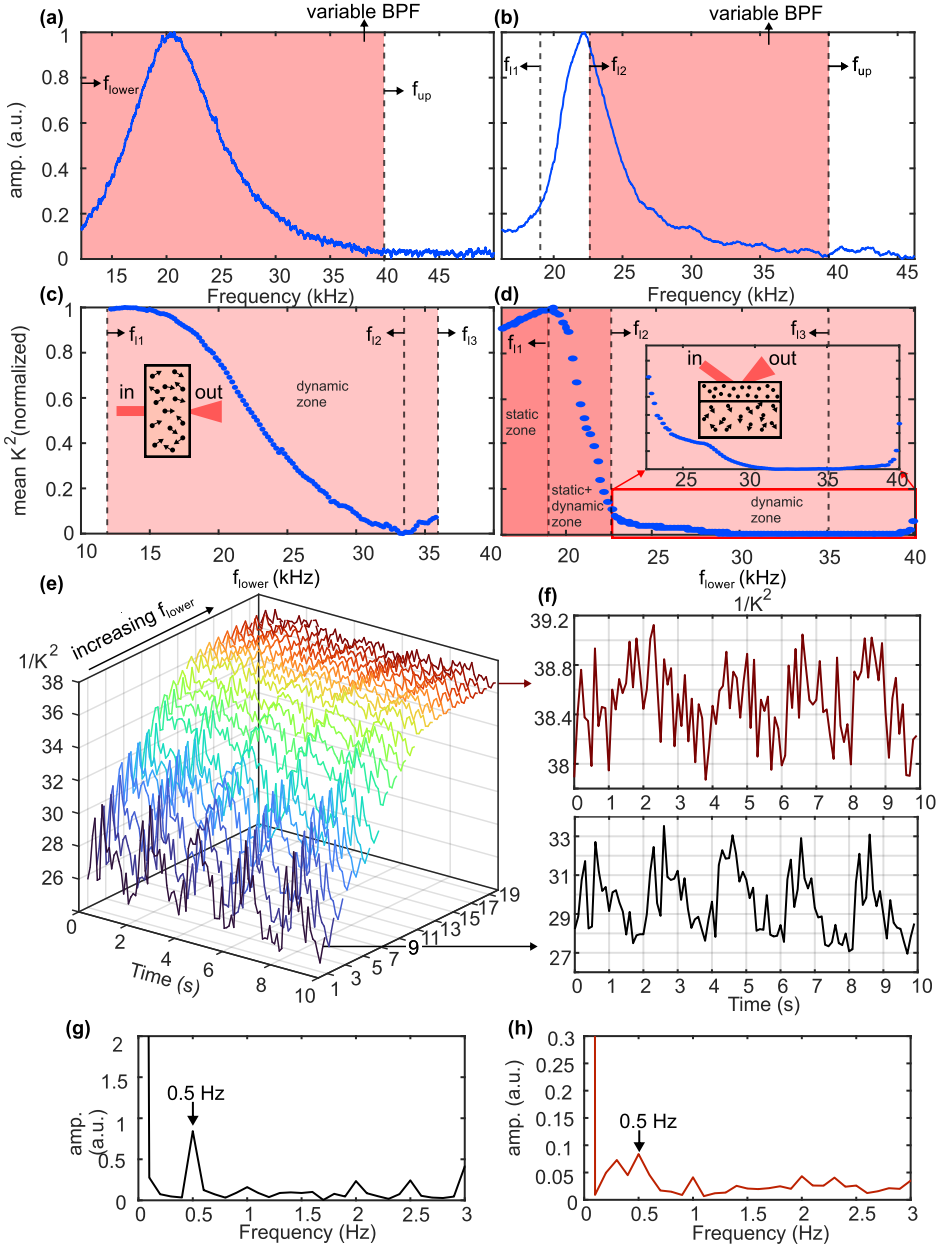

Figure 4.2: Measurement results for the two configurations of dynamic samples, first the homogeneous Intralipid solution and the second the multi layer sample. The averaged power spectral density (PSD) yields the Doppler-broadened photon distribution of time-of-flight (DTOF) for %7.48 (a) Intralipd emulsion in the transmission geometry and (b) two-layer phantom in the reflectance geometry ; (c-d) A series of band-pass (BP) filters is applied to the PSD of each pixel; the lower cutoff frequency f_{lower} is incremented in 200 Hz steps while the upper (f_{up}) cutoff remains fixed; (e) Speckle contrast after each BP filter, displayed with relative offsets from their respective means; (f) Temporal fluctuation of speckle contrast for f_{lower} = 22.5 kHz (lower panel) and f_{lower} = 25.2 kHz (upper panel); (g–h) Fourier transforms of the signals in (d): (g) corresponds to f_{lower} = 22.5 kHz and (h) to f_{lower} = 25.2 kHz. Both spectra clearly reveal the 0.5 Hz flow modulation imposed by the syringe pump.

4.4. CONCLUSION AND DISCUSSION

In this chapter, we introduced frequency-modulated scattering holography (FMSH) as a new approach for depth-resolved measurement of dynamics in turbid media. By combining low-frequency laser modulation with massively parallel camera detection, FMSH achieves photon-counting sensitivity while preserving the ability to separate dynamic scattering contributions by photons different ToFs. Unlike conventional SBF methods that require long source–detector separations to suppress superficial signals, the ToF gate ability of FMSH enable it high-resolution measurements at short separations with improved photon throughput.

The concept was experimentally validated in a two-layer phantom consisting of a static superficial layer and a dynamic deeper layer. The results demonstrated that photons with longer ToF contributed a greater fraction of their partial path length to the deeper layer and exhibited faster decorrelation. By applying BP filters to the PSD, we successfully isolated depth-dependent speckle contrasts. Higher-frequency bands emphasized contributions from longer ToFs and produced lower speckle contrast values, consistent with the expected dynamics of the deeper layer. Importantly, both shallow- and deep-weighted contrasts retained sensitivity to the periodic flow modulation introduced by the syringe pump, confirming that FMSH can resolve dynamic signatures across depths with temporal resolution of 10 Hz.

These findings highlight several important advantages of FMSH. First, its reliance on camera-based parallel detection provides a substantial SNR gain over single-channel iDO approaches such as iNIRS, while avoiding the exponential photon loss associated with long source–detector separations in DCS and SCOS. Second, the intrinsic ToF encoding introduced by frequency modulation enables post-processing "virtual gating," analogous to coherence gating in the previous system[18] but without requiring precise control of optical path length or laser bandwidth. This flexibility simplifies experimental implementation and makes FMSH compatible with low-cost hardware.

At the same time, several limitations should be noted. The present implementation relies on relatively slow modulation frequencies and moderate camera frame rates, which constrain the achievable temporal resolution compared to ultrafast iDO methods such as iNIRS and DC-DWS. Moreover, while the two-layer phantom experiments demonstrate depth specificity, translation to in vivo measurements will require careful consideration of tissue heterogeneity, motion artifacts, and physiological noise. Finally, quantitative recovery of flow indices (e.g., blood flow index, BFi) will depend on robust modeling of ToF-dependent speckle contrast, which may necessitate integration with photon migration models or Monte Carlo simulations.

In summary, FMSH provides a powerful new framework for probing dynamic light scattering in complex media. By uniting frequency modulation, heterodyne detection, and parallel speckle analysis, this method achieves depth-specific sensitivity without sacrificing photon efficiency. These capabilities position FMSH as a promising tool for advancing noninvasive, high-sensitivity imaging of cerebral hemodynamics and other applications where resolving flow at different depths is essential.

4.5. APPENDIX

4.5.1. DEEP-TO-SHALLOW FLOW SPECIFICITY

SPECKLE SPECIFICITY

Previous works[22–24] have demonstrated the brain-to-scalp specificity in diffuse correlation spectroscopy. Based on[24, 25], we derive the specificity to deep flow in a two-layer sample for speckle contrast optical spectroscopy (SCOS). The speckle contrast without ToF-gate is given by

$$K^2 = \frac{2\beta}{T}\int_0^T (1-\frac{\tau}{T}) g_1(\tau)^2 d\tau \tag{4.6}$$

where β accounts for the spatial and temporal coherence factors of setup and $g_1(\tau)$ is the field correlation[24]

$$g_1(\tau) =< \exp[-2k_0^2\alpha_1 D_{B1}\mu_{s1}^{'} l_1 \tau]\exp[-2k_0^2\alpha_2 D_{B2}\mu_{s2}^{'} l_2 \tau] > . \tag{4.7}$$

Here α_1 and α_2 are the dynamic scattering ratio in layer 1 and layer 2; D_{B1} and D_{B2} are the diffusion coefficient in layer 1 and layer 2; $\mu_{s1}^{'}$ and $\mu_{s2}^{'}$ are the reduced scattering coefficient of layer 1 and layer 2; l_1 and l_2 are the partial path length in layer 1 and layer 2. Because the integration time T is much higher than the decorrelation time of g_1, we have

$$\begin{aligned} K^2 &= \frac{2\beta}{T}\int_0^T |g_1(\tau)|^2 d\tau \\ &= \frac{2\beta}{T}\int_0^T < \exp[-4k_0^2(\alpha_1 D_{B1}\mu_{s1}^{'} l_1 + \alpha_2 D_{B2}\mu_{s2}^{'} l_2)\tau] > d\tau \\ &\approx \frac{-2\beta}{4k_0^2 T(\alpha_1 D_{B1}\mu_{s1}^{'}\overline{l_1} + \alpha_2 D_{B2}\mu_{s2}^{'}\overline{l_2})} \\ &\times < \exp[-4k_0^2(\alpha_1 D_{B1}\mu_{s1}^{'} l_1 + \alpha_2 D_{B2}\mu_{s2}^{'} l_2)\tau] > |_0^T \\ &\approx \frac{\beta}{2k_0^2 T(\alpha_1 D_{B1}\mu_{s1}^{'}\overline{l_1} + \alpha_2 D_{B2}\mu_{s2}^{'}\overline{l_2})} \end{aligned} \tag{4.8}$$

Then the blood flow changes in the first layer introduce speckle contrast variation

$$\partial(1/K^2)/\partial(\alpha_1 D_{B1}) = \frac{2k_0^2 T}{\beta}\mu_{s1}^{'}\overline{l_1}. \tag{4.9}$$

Thus, the deep-to-shallow flow specificity with ToF filter is given by

$$\begin{aligned} &[(\alpha_2 D_{B2})\partial(1/K^2)/\partial(\alpha_2 D_{B2})]/[(\alpha_1 D_{B1})\partial(1/K^2)/\partial(\alpha_1 D_{B1})] \\ &= \frac{\alpha_2 D_{B2}\mu_{s2}^{'}\overline{l_2}}{\alpha_1 D_{B1}\mu_{s1}^{'}\overline{l_1}} \end{aligned} \tag{4.10}$$

After applying the bandpass filter (BF), the selected photons have longer time-of-flight and its specificity is:

$$\text{spec(BF)} = \frac{\alpha_2 D_{B2}\mu_{s2}^{'}\overline{l_2(\text{BF})}}{\alpha_1 D_{B1}\mu_{s1}^{'}\overline{l_1(\text{BF})}} \tag{4.11}$$

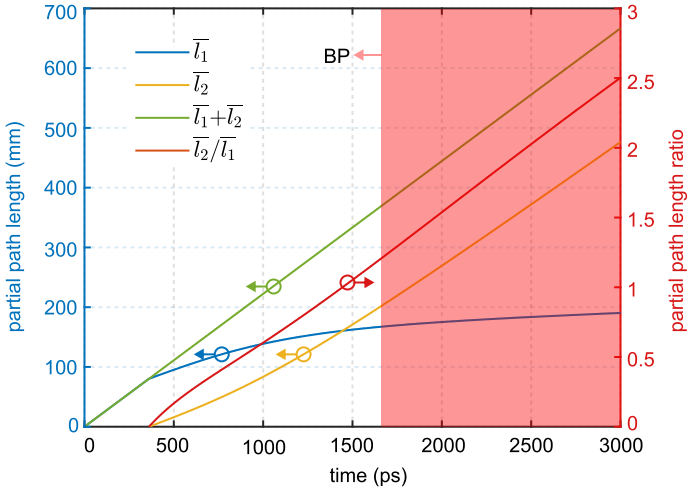

Figure 4.3: The average partial path length in layer 1 and layer 2 ($\overline{l_1}$ and $\overline{l_2}$) and their ratio $\overline{l_2}/\overline{l_1}$. The partial path length ratio increases with time-of-flight, therefore, selecting photons with higher time-of-flight by the bandpass filter (BP) increases the deep-to-shallow specificity.

PARTIAL PATH LENGTH *vs* TIME-OF-FLIGHT

For a two-layer sample, the time-resolved reflectance is given by

$$R(t) = R_{\mu_a=0}(t) \int_0^\infty \int_0^\infty g(l_1(t), l_2(t), t) \exp(-\mu_{a1} l_1(t)) \exp(-\mu_{a2} l_2(t)) d l_1(t) l_2(t) \quad (4.12)$$

where $R_{\mu_a=0}(t)$ denotes the time-resolved reflectance when the sample has a zero absorption, $g(l_1(t), l_2(t), t)$ is the probability density function for the partial path length of scattered photons in the layer 1 ($l_1(t)$) and layer 2 ($l_2(t)$) with a time-of-flight t. The thickness of the sample is $l_1(t) + l_2(t) = vt$ where v is the velocity of light in the medium. The average partial path length in layer 1 with time-of-flight t is expressed by:

$$\begin{aligned} \overline{l_1(t)} &= \frac{\int_0^\infty \int_0^\infty l_1(t) g(l_1(t), l_2(t), t) \exp(-\mu_{a1} l_1(t)) \exp(-\mu_{a2} l_2(t)) d l_1(t) l_2(t)}{\int_0^\infty \int_0^\infty g(l_1(t), l_2(t), t) \exp(-\mu_{a1} l_1(t)) \exp(-\mu_{a2} l_2(t)) d l_1(t) l_2(t)} \\ &= -\frac{\partial R(t)/\partial \mu_{a1}}{R(t)} \end{aligned} \quad (4.13)$$

From equation (4.13), the average partial path length in layer 2 with time-of-flight t is $\overline{l_2(t)} = vt - \overline{l_1(t)}$. The time-resolved reflectance has been given in [26] for the two layers with different absorption coefficient. For $\mu_{a1} = 100\ m^{-1}$, $\mu_{a2} = 200\ m^{-1}$ and $\mu_s' = 1000\ m^{-1}$, the first layer has a thickness 5 mm, and the total thickness is set to 100 mm, from equation (4.13), the partial path length $\overline{l_1(t)}$ and $\overline{l_2(t)}$ is calculated as shown in Figure, and this is independent of the source-detector separation. Therefore, for a longer time-of-flight, the ratio between $\overline{l_2(t)}$ and $\overline{l_1(t)}$ is higher, which means that the time-of-flight gate increases the deep-to-shallow specificity.

BIBLIOGRAPHY

[1] K. Kisler, A. R. Nelson, A. Montagne, and B. V. Zlokovic, "Cerebral blood flow regulation and neurovascular dysfunction in alzheimer disease", Nature Reviews Neuroscience **18**, 419–434 (2017).

[2] E. A. Neuwelt, B. Bauer, C. Fahlke, G. Fricker, C. Iadecola, D. Janigro, L. Leybaert, Z. Molnár, M. E. O'donnell, J. T. Povlishock, et al., "Engaging neuroscience to advance translational research in brain barrier biology", Nature Reviews Neuroscience **12**, 169–182 (2011).

[3] M. A. Lodge, R. E. Carson, J. A. Carrasquillo, M. Whatley, S. K. Libutti, and S. L. Bacharach, "Parametric images of blood flow in oncology pet studies using [15o] water", Journal of Nuclear Medicine **41**, 1784–1792 (2000).

[4] Y. Makari, T. Yasuda, Y. Doki, H. Miyata, Y. Fujiwara, S. Takiguchi, J. Matsuyama, M. Yamasaki, T. Hirao, M. K. Koyama, et al., "Correlation between tumor blood flow assessed by perfusion ct and effect of neoadjuvant therapy in advanced esophageal cancers", Journal of Surgical Oncology **96**, 220–229 (2007).

[5] S. Schuh, J. Holmes, M. Ulrich, L. Themstrup, G. B. Jemec, N. De Carvalho, G. Pellacani, and J. Welzel, "Imaging blood vessel morphology in skin: dynamic optical coherence tomography as a novel potential diagnostic tool in dermatology", Dermatology and therapy **7**, 187–202 (2017).

[6] C.-S. Wu, H.-S. Yu, H.-R. Chang, C.-L. Yu, C.-L. Yu, and B.-N. Wu, "Cutaneous blood flow and adrenoceptor response increase in segmental-type vitiligo lesions", Journal of dermatological science **23**, 53–62 (2000).

[7] M. Yamamoto, S. Sasaguri, and T. Sato, "Assessing intraoperative blood flow in cardiovascular surgery", Surgery today **41**, 1467–1474 (2011).

[8] S. I. Gelman, "Disturbances in hepatic blood flow during anesthesia and surgery", Archives of Surgery **111**, 881–883 (1976).

[9] R. Bandyopadhyay, A. Gittings, S. Suh, P. Dixon, and D. J. Durian, "Speckle-visibility spectroscopy: a tool to study time-varying dynamics", Review of scientific instruments **76** (2005).

[10] C. P. Valdes, H. M. Varma, A. K. Kristoffersen, T. Dragojevic, J. P. Culver, and T. Durduran, "Speckle contrast optical spectroscopy, a non-invasive, diffuse optical method for measuring microvascular blood flow in tissue", Biomedical optics express **5**, 2769–2784 (2014).

[11] T. Durduran, R. Choe, W. B. Baker, and A. G. Yodh, "Diffuse optics for tissue monitoring and tomography", Reports on progress in physics **73**, 076701 (2010).

[12] R. Lohwasser and G. Soelkner, "Experimental and theoretical laser-doppler frequency spectra of a tissuelike model of a human head with capillaries", Applied optics **38**, 2128–2137 (1999).

[13] A. Humeau, W. Steenbergen, H. Nilsson, and T. Strömberg, "Laser doppler perfusion monitoring and imaging: novel approaches", Medical & biological engineering & computing **45**, 421–435 (2007).

[14]D. Borycki, O. Kholiqov, S. P. Chong, and V. J. Srinivasan, "Interferometric near-infrared spectroscopy (inirs) for determination of optical and dynamical properties of turbid media", Optics express **24**, 329–354 (2016).

[15]B. Zhang, C. Phillips, E. Venialgo Araujo, S. Iskander-Rizk, J. Pupeikis, B. Willenberg, U. Keller, and N. Bhattacharya, "Study of time-resolved dynamics in turbid medium using a single-cavity dual-comb laser", ACS Photonics (2024).

[16]W. Zhou, O. Kholiqov, S. P. Chong, and V. J. Srinivasan, "Highly parallel, interferometric diffusing wave spectroscopy for monitoring cerebral blood flow dynamics", Optica **5**, 518–527 (2018).

[17]J. Xu, A. K. Jahromi, J. Brake, J. E. Robinson, and C. Yang, "Interferometric speckle visibility spectroscopy (isvs) for human cerebral blood flow monitoring", Apl Photonics **5** (2020).

[18]M. Zhao, W. Zhou, S. Aparanji, D. Mazumder, and V. J. Srinivasan, "Interferometric diffusing wave spectroscopy imaging with an electronically variable time-of-flight filter", Optica **10**, 42–52 (2023).

[19]M. Zhao, L. Dickstein, A. S. Nadig, W. Zhou, S. Aparanji, H. G. Estrada, S.-J. Liu, T. Zhou, W. Yang, A. Lord, et al., "Comprehensive optimization of interferometric diffusing wave spectroscopy (idws)", IEEE Journal of Selected Topics in Quantum Electronics (2025).

[20]A. M. Goldfain, P. Lemaillet, D. W. Allen, K. A. Briggman, and J. Hwang, "Polydimethylsiloxane tissue-mimicking phantoms with tunable optical properties", J. Biomed. Opt. **27**, 074706–074706 (2022).

[21]S. Samaei, K. Nowacka, A. Gerega, Ż. Pastuszak, and D. Borycki, "Continuous-wave parallel interferometric near-infrared spectroscopy (cw π nirs) with a fast two-dimensional camera", Biomedical Optics Express **13**, 5753–5774 (2022).

[22]J. Selb, D. A. Boas, S.-T. Chan, K. C. Evans, E. M. Buckley, and S. A. Carp, "Sensitivity of near-infrared spectroscopy and diffuse correlation spectroscopy to brain hemodynamics: simulations and experimental findings during hypercapnia", Neurophotonics **1**, 015005–015005 (2014).

[23]W. B. Baker, A. B. Parthasarathy, D. R. Busch, R. C. Mesquita, J. H. Greenberg, and A. Yodh, "Modified beer-lambert law for blood flow", Biomedical optics express **5**, 4053–4075 (2014).

[24]W. Zhou, O. Kholiqov, J. Zhu, M. Zhao, L. L. Zimmermann, R. M. Martin, B. G. Lyeth, and V. J. Srinivasan, "Functional interferometric diffusing wave spectroscopy of the human brain", Science Advances **7**, eabe0150 (2021).

[25]S. Del Bianco, F. Martelli, and G. Zaccanti, "Penetration depth of light re-emitted by a diffusive medium: theoretical and experimental investigation", Physics in Medicine & Biology **47**, 4131 (2002).

[26]F. Martelli, A. Sassaroli, Y. Yamada, and G. Zaccanti, "Analytical approximate solutions of the time-domain diffusion equation in layered slabs", Journal of the Optical Society of America A **19**, 71–80 (2002).

5

5

COHERENCE-GATED INTERFEROMETRIC SPECKLE VISIBILITY SPECTROSCOPY

Speckle-based flow (SBF) measurement techniques offer non-invasive, portable, and sensitive solutions for cerebral blood flow (CBF) monitoring. Among these, speckle visibility spectroscopy (SVS) and its interferometric variant (iSVS) stand out for their high photon throughput and low cost. However, to enhance sensitivity to CBF, both SVS and iSVS typically rely on large source-detector (SD) separations, which significantly reduce photon flux and spatial resolution. In this work, we present a novel coherence-gated iSVS approach that leverages a low-coherence laser diode to selectively filter out photons from superficial layers—eliminating the need for long SD separations. This strategy dramatically improves light throughput and spatial resolution while reducing system cost. Our method offers a practical and scalable solution for high-resolution, depth-sensitive CBF imaging.

Parts of this chapter have been done as a manuscript and will be submitted to an academic journal.

5.1. INTRODUCTION

Disruptions in cerebral blood flow (CBF) are closely linked to a variety of serious neurological conditions, including stroke [1], cognitive decline [2], and neurodegenerative diseases such as Alzheimer's disease [3]. Accurate and continuous monitoring of CBF is therefore of significant clinical value. An ideal CBF monitoring modality would be non-invasive, portable, cost-effective, and suitable for frequent or bedside use. Existing clinical techniques each suffer from key limitations. Transcranial ultrasound [4] is non-invasive but highly operator-dependent and lacks sensitivity to microvascular flow. X-ray computed tomography (CT) [5], long considered a standard for perfusion imaging, involves ionizing radiation and is unsuitable for repeated measurements. Magnetic resonance imaging (MRI) [6, 7] avoids radiation and offers high-resolution data, but remains expensive and logistically constrained to advanced clinical facilities.

Given these limitations, optical methods have emerged as promising alternatives, particularly those leveraging the low absorption of biological tissue in the near-infrared (NIR) window [8–14]. Among these, speckle-based flow (SBF) measurement techniques are especially attractive due to their non-invasiveness, portability, and sensitivity to microvascular hemodynamics, offering a practical path toward accessible CBF monitoring tools.

In SBF, coherent laser light illuminates biological tissue, and the resulting multiply scattered photons interfere to form a dynamic speckle pattern [15]. Diffuse correlation spectroscopy (DCS), a prominent SBF technique [11, 16], detects one or a few speckles using photon-counting detectors and analyzes the temporal intensity autocorrelation function (g_2) to quantify the blood flow index (BFi). To achieve high signal-to-noise ratio (SNR), DCS requires a highly coherent light source and single-mode fiber (SMF) collection, which significantly limits photon throughput. To increase throughput, multi-channel DCS systems collect multiple speckles using bundles of SMFs connected to multiple photon-counting detectors[17]. However, these systems are limited by their complexity and high cost. The emergence of single-photon avalanche diode (SPAD) cameras [18] addresses these limitations by enabling massively parallel detection with tens of thousands of channels, significantly reducing system complexity [19–21].

Unlike DCS, which rapidly detects the decorrelation time of scattered light, speckle contrast optical spectroscopy (SCOS) [13, 14] provides an alternative approach by using a slow-frame-rate camera to collect many speckles simultaneously. The ensemble speckle contrast of the entire speckle pattern yields an integrated measure of intensity decorrelation time. This approach enables high photon throughput by leveraging the large number of pixels in imaging sensors, while also reducing system cost.

Recently, interferometric diffuse optical (iDO) techniques [22–25] have been developed to enhance the signal-to-noise ratio (SNR) in SBF measurements through heterodyne amplification. Among these, interferometric speckle visibility spectroscopy (iSVS) [24, 26, 27] integrates interferometric detection into the SCOS framework to improve sensitivity. However, to increase the specificity to deep tissue flow, both SCOS and iSVS typically use large source–detector (SD) separations [28], which reduces spatial resolution and photon throughput due to the exponential attenuation of photon flux with increasing SD separation [29].

An alternative strategy for enhancing specificity to deep flow is to reject photons with

short time-of-flights (ToFs), which predominantly originate from superficial layers. This ToF-gating approach has been widely adopted in DCS, implemented via either electronic gating [30] or coherence gating [22, 25, 31]. A recent study [32] introduced electronic ToF gating into speckle contrast imaging, but this method is limited by system complexity and cost.

In this work, we present a coherence-gated iSVS system that incorporates a coherence-based ToF gate. By rapidly modulating the power of a single-mode 1064-nm distributed-feedback (DFB) laser during the camera exposure period, a stable coherence gate is established [31]. Building upon the methodology described in [31], the current architecture utilizes a low-frame-rate camera in place of a high-speed sensor. This modification significantly reduces both the system cost and the data throughput requirements. By tuning the optical path length difference (OPD) between the sample and reference arms, we selectively interfere photons with specific ToFs. This enables operation at short SD separations, thereby improving spatial resolution and photon throughput while maintaining sensitivity to deep flow. The resulting system offers a cost-effective and practical solution for high-resolution, depth-sensitive cerebral blood flow (CBF) monitoring.

5.2. METHOD

5.2.1. INSTRUMENTATION

Figure 5.1 (a) illustrates the experimental setup for CG-iSVS used to measure dynamics in turbid media. An 1064 nm central wavelength single-mode DFB laser diode (1064LD, Aerodiode) is employed, driven by a laser diode driver (LDC205C, Thorlabs) and stabilized using a temperature controller (TED200C, Thorlabs). To facilitate the coherence gating, the injection current is modulated by a waveform generator (WG) in 50 kHz with 0.5V amplitude. The laser beam is split into two paths by a beam splitter (BS). In the measurement arm, the beam is directed to the sample by a mirror (M1) with a power of 80 mW. Scattered photons are collected by a multimode fiber (MMF, FG1000LEA, Thorlabs) with 3 mm seperation, collimated and projected onto a camera (DMK 42AU03). In the reference arm, the beam is delayed using a retroreflector (Retro) and attenuated by a variable optical attenuator (VOA) to prevent camera saturation. The reference beam is directed by two mirror (M2 and M3), and is tilted by a small angle. The camera operates at a frame rate of 25 frames per second with an exposure time of 1/50 s. The exposure duration serves as the integration period, encompassing multiple modulation cycles driven by the WG. The camera has a resolution of 1280×960 pixels.

The sample consists of two layers. The first layer is composed of polydimethylsiloxane (PDMS), carbon powder, and titanium dioxide (TiO_2), formulated to mimic the optical properties of human tissue. The second layer is a mixture of 20% Intralipid and water, which is pumped by a syringe pump to control the flow rate.

5.2.2. COHERENCE-GATED HETERODYNE SPECKLE VISIBILITY FACTOR

The CG-iSVS works in an off-axis holography configuration, where the direct current (DC) component can be removed easily in spatial-frequency domain. The attenuated local oscillator (LO) interferes with the speckle pattern collimated from sample and the

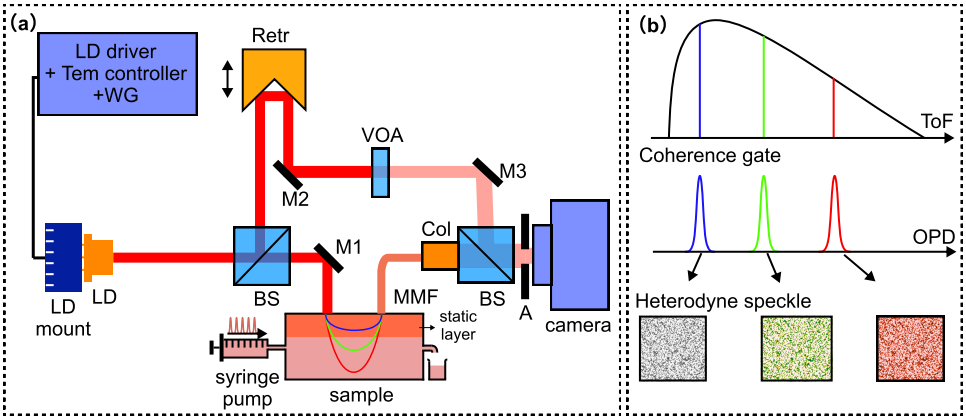

Figure 5.1: The schematic diagram of the CG-iSVS setup and its operating principle. (a) The off-axis holographic configuration of CG-iSVS. Components: LD – laser diode; Temp Controller – temperature controller; WG-waveform generator; Retro – retroreflector; BS – beam splitter; VOA – variable optical attenuator; M1, M2, M3 – mirrors; MMF – multimode fiber; Col – collimator; A - aperture. (b) The retroreflector adjusts the optical path difference (OPD) between the reference and measurement arms, enabling interference of photons with a specific time of flight (ToF), thereby generating heterodyne speckles corresponding to different photon path lengths.

5

intensity at the pixel p is given by

$$I_{\mathrm{p}}(s,t) = \int_0^T |\mathbf{E}^{\mathrm{p}}_{\mathrm{LO}}(t)|^2 + |\mathbf{E}^{\mathrm{p}}_{\mathrm{sam}}(t)|^2 + 2\,\mathrm{Re}\left\{\gamma^2 \mathbf{E}^{\mathrm{p}}_{\mathrm{LO}}(t)\,\mathbf{E}^{\mathrm{p}*}_{\mathrm{sam}}(s,t)\,e^{i[k_0 x\sin\theta+\varphi_s^p(t)]}\right\} dt \quad (5.1)$$

where T is the camera exposure time, $\mathbf{E}^{\mathrm{p}}_{\mathrm{LO}}(t)$ denotes the LO electric field at pixel p, and $\mathbf{E}^{\mathrm{p}}_{\mathrm{sam}}(s,t)$ denotes the sample field associated with scattering path length s at pixel p. γ^2 is the mutual coherence factor between the LO and the sample. The terms $k_0 x\sin\theta$ and $\varphi^{\mathrm{p}}_s(t)$ are the spatial carrier and the temporal phase difference between the two beams, respectively. By translating the retroreflector, the path length s is adjusted (Figure 5.1 (b)). In the raw hologram, the sample speckle term $|\mathbf{E}^{\mathrm{p}}_{\mathrm{sam}}(t)|^2$ overlaps with the heterodyne speckle term $\mathrm{Re}\left\{\gamma^2 \mathbf{E}^{\mathrm{p}}_{\mathrm{LO}}(t)\,\mathbf{E}^{\mathrm{p}*}_{\mathrm{sam}}(s,t)\,e^{i[k_0 x\sin\theta+\varphi_s^p(t)]}\right\}$, where the former is not depth-selective and should be rejected. After a spatial Fourier transform, the LO and the sample speckle (the DC components) remain near the origin due to the pinhole's effective spatial low-pass filtering, while the heterodyne term is shifted to higher spatial frequencies (Figure 5.2 (c)). Removing the DC component, selecting the positive first-order sideband, and assuming a spatially uniform LO across the sensor $\mathbf{E}^{p}_{\mathrm{LO}}(t) = \mathbf{E}_{\mathrm{LO}}(t)$, the interferometric intensity at pixel p is given by

$$I^{\mathrm{p}}_{\mathrm{ac}}(s,t) = \int_0^T \gamma^2 |\mathbf{E}_{\mathrm{LO}}(t)|\,|\mathbf{E}^{\mathrm{p}}_{\mathrm{sam}}(s,t)|\cos\varphi^{p}_s(t)\,dt \quad (5.2)$$

According to [24], the second moment of $I_{\mathrm{ac}}(s,t)$ across all pixels is

$$<|I^{\mathrm{p}}_{\mathrm{ac}}(s,t)|^2> = \gamma^2 I_{\mathrm{LO}} \langle I_{\mathrm{sam}}(s)\rangle T \int_0^T 2(1-\frac{t}{T}) g_1(s,t)\,dt \quad (5.3)$$

here $I_{LO} = |\mathbf{E}_{LO}(t)|^2$, $\langle I_{sam}(s)\rangle = \langle|\mathbf{E}^{p}_{sam}(s,t)|^2\rangle$ and $g_1(s,t)$ is the field autocorrelation function of photons with scattering path s. After calibrating the I_{LO} and $\langle I_{sam}\rangle$, the path-dependent visibility factor is

$$F(s) = \frac{<|I^{p}_{ac}(s,t)|^2>}{I_{LO}\langle I_{sam}\rangle} = \gamma\alpha(s)T\int_0^T 2(1-\frac{t}{T})g_1(s,t)dt \tag{5.4}$$

here I_{LO} and $\langle I_{sam}\rangle$ can be measured by blocking the measurement arm and the reference arm respectively. $\langle I_{sam}(s)\rangle = \alpha(s)\langle I_{sam}\rangle$, where $\alpha(s)$ is the ratio between photons with sacttering path s and whole scattering photons. The decorrelation time τ of photons from sacttering path s is much lower than the exposure time T, therefore

$$F(s) = \gamma\alpha(s)T\int_0^T 2(1-\frac{t}{T})\exp(-t/\tau)dt = 2\gamma\alpha(s)T\tau \tag{5.5}$$

Theoretically, $F(s)$ ranges from 0 (fast dynamics) to 1 (no dynamics), but in reality, the visibility factor has an non-zero offset, which comes from both the laser (shot noise) and the camera noise (readout noise and quantization noise), which need to be corrected[24]:

$$F'(s) = (1-\beta) + \beta[2\gamma\alpha(s)T\tau] \tag{5.6}$$

The corrected visibility factor gives the blood flow index $1/F'(s)$. Compared with normal iSVS, the coherence gate produced by the multimode laser makes it possible for us to directly measure the path-dependent dynamics here.

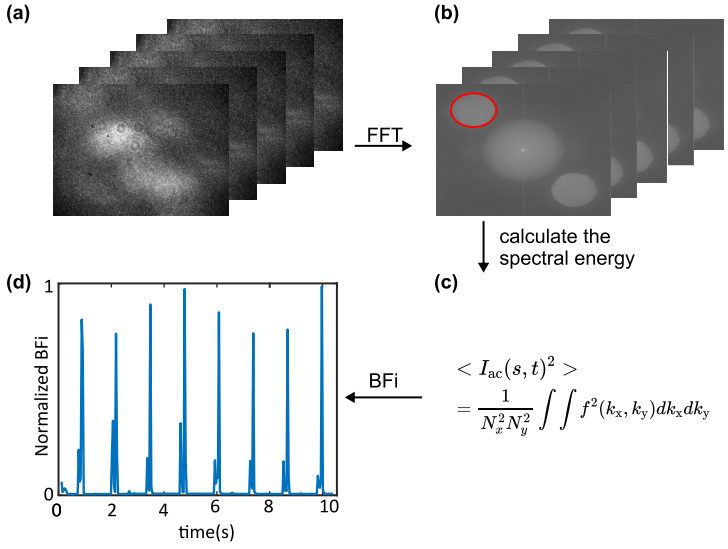

Figure 5.2: The data processing of the CG-iSVS. (a) The raw images acquired from the camera. (b) Spatial FFT of the image in (a). (c) The second moment is calculated directly in the spatial frequency domain using the AC component. (d) The normalized blood flow index.

5.2.3. DATA PROCESSING

Figure 5.2 illustrates the data processing pipeline. First, the raw interferogram recorded by the camera is transformed into the spatial-frequency domain via a two-dimensional Fourier transform. As shown is Figure 5.2(b), the DC term and the AC sidebands are clearly separated. An ellipse detection algorithm is then applied to locate and segment the AC component, which corresponds to the heterodyne signal containing the flow information. Within the selected AC region, the spectral energy is calculated directly in the frequency domain (Figure 5.2(c)) according to Parseval's theorem, providing a quantitative measure of the temporal fluctuations induced by moving scatterers. To remove the contribution of camera and shot noise, the measured spectrum is corrected using Eq. (5.6). Finally, the result is normalized to yield the blood flow index, which serves as a depth-resolved and noise-compensated metric of cerebral blood flow dynamics (Figure 5.2(d)).

5.3. RESULTS

5.3.1. INSTRUMENT RESPONSE FUNCTION

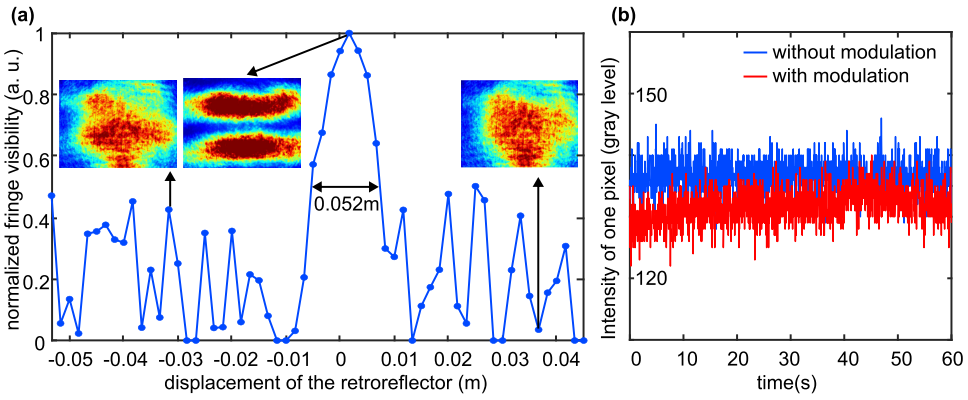

Figure 5.3: Instrument Response Function (IRF) characterization of the CG-iSVS system. (a) Measured fringe visibility from a Michelson interferometer as a function of OPD to characterize the coherence length of the modulated laser diode. (b) Comparison of pixel intensity stability recorded with the waveform generator in the "on" and "off" states, demonstrating the effectiveness of the integration-based averaging.

To characterize the coherence gate width at a modulation amplitude of 0.5 V, a standard Michelson interferometer was constructed. A camera was employed to monitor the interference fringe visibility across varying optical path differences (OPDs). The fringe visibility was quantified using:$(I_{max} - I_{min})/(I_{max} + I_{min})$. In the Michelson interferometer, the retroreflector is translated in 1 mm increments, resulting in a 2 mm increase in the OPD per step. As illustrated in Fig. 5.3(a), high-contrast fringes are observed at zero OPD, which gradually vanish as the OPD increases. The inset displays the interferograms captured by the camera at three distinct positions. Interference fringes are clearly resolved at zero OPD but exhibit significant loss of contrast at the other two positions. The full width at half maximum (FWHM) of the normalized visibility curve yields

a coherence length of 0.052 m, which corresponds to a Time-of-Flight (ToF) gate of 173 ps.

To mitigate intensity variations during current modulation, the laser is modulated at 50 kHz with a camera exposure time of 1/50 s, effectively integrating over 1000 modulation periods. As illustrated in Fig. 5.3 (b), despite the lack of hardware synchronization between the camera and the waveform generator, the intensity of a single pixel exhibits a stability comparable to that of the laser without current modulation.

5.3.2. FLOW UNDER DIFFERENT OPDS

The coherence gate concept was validated using a two-layer tissue-mimicking phantom. The first layer was formulated with carbon black powder (0.0055 wt%) to reproduce the absorption of the scalp, which exhibits an absorption coefficient of 0.74 mm^{-1} at 1064 nm. To introduce scattering similar to that of cranial bone, 0.1 wt% titanium dioxide powder was added, yielding a reduced scattering coefficient of 8.9 mm^{-1} at 1064 nm [33]. The second layer consisted of intralipid diluted (20ml 20% intralipid) in water (60 ml), which was driven by a syringe pump with 0.5 Hz to generate controlled flow, thereby serving as a dynamic scattering medium to mimic blood flow.

To verify the functionality of the coherence gate, we quantified the interferometric intensity (I_{ac}) across a range of OPDs. As illustrated in Fig. 5.4(b), a prominent AC component is observed when the reference arm delay (t_d) is set to 600 ps and 833 ps, whereas the signal is significantly attenuated at t_d = 0 ps and 1167 ps. The overall evolution of the interferometric signal is summarized in Fig. 5.4(a); the observed profile closely follows the distribution-of-time-of-flight (DTOF) of photons migrating through the turbid medium. This correlation confirms that the coherence-gating strategy effectively isolates photons based on their path length.

The depth-selective capability is further demonstrated by the flow measurements. At t_d = 0 ps (Fig. 5.4(c)), the visibility factor fails to detect the flow dynamics because the coherence gate is positioned at the entry surface, where the signal is dominated by ballistic reflections from the static air-medium interface and the initial static layer. In contrast, at t_d = 600 ps and 833 ps, the gate successfully overlaps with the deeper scattering volumes, allowing the system to capture the underlying flow dynamics. Finally, at t_d = 1167 ps, the flow signal becomes nearly undetectable. At this extended delay, although the photons have traveled through the flow region, the signal-to-noise ratio is too low to extract meaningful dynamic information due to the inherent decay of the DTOF.

Furthermore, three samples with static layer thicknesses ranging from 0.8 to 1.2 cm were measured with the reference delay t_d fixed at 600 ps. As shown in Fig. 5.5(a-c), the flow dynamics were successfully captured in all cases. Their corresponding Fourier transforms, shown in Fig. 5.5(d), exhibit clear peaks at 0.5 Hz, demonstrating excellent agreement with the modulation rate of the peristaltic pump.

5.4. CONCLUSIONS AND DISCUSSION

In this chapter, we have introduced and validated a coherence-gated interferometric speckle visibility spectroscopy (CG-iSVS) system designed for depth-sensitive blood flow monitoring. By integrating a coherence-based ToF gate into the iSVS framework, the

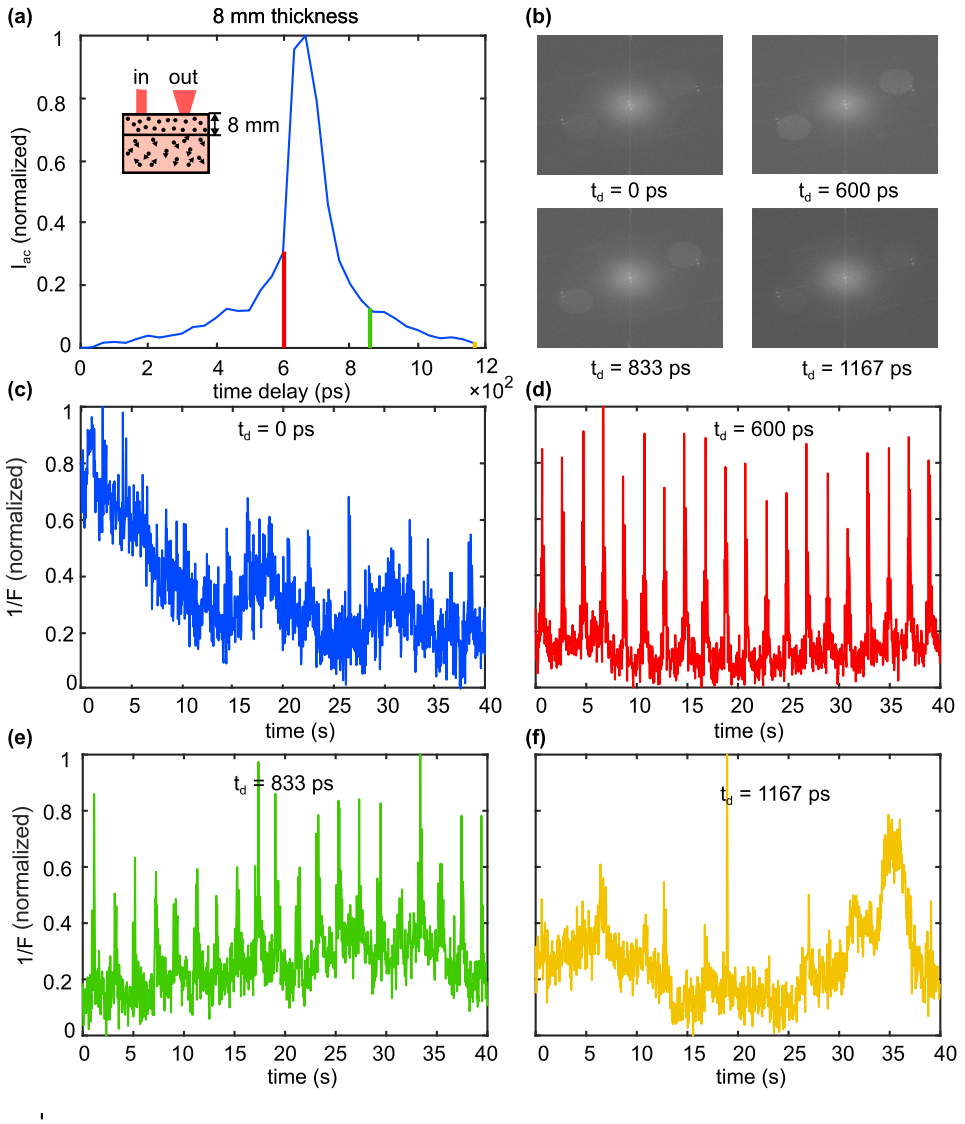

Figure 5.4: Visibility measurements for flow beneath a 0.8 cm static scattering layer. (a) Normalized interferometric intensity I_{ac} as a function of Optical path difference (OPD). (b) Spatial Fourier spectra of interferograms obtained at various OPDs, highlighting the variations in interferometric signal strength. (c)–(f) Normalized speckle visibility $(1/F)$ calculated at different OPDs, illustrating the depth-selective gating effect.

proposed method enables the selective isolation of photons from deep scattering volumes while effectively rejecting those originating from superficial layers. This approach represents a fundamental advancement over conventional SVS and iSVS, which typically rely on large SD separations to achieve depth sensitivity at the expense of photon throughput and spatial resolution.

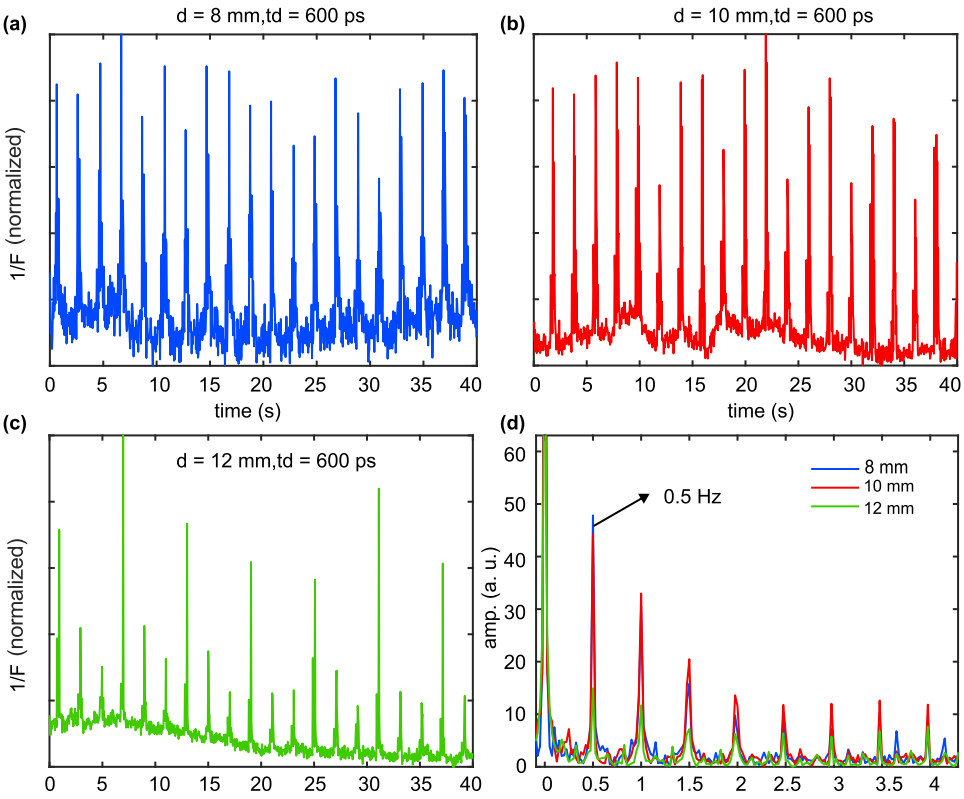

Figure 5.5: Visibility factor measurements for flow beneath static layers of varying thicknesses (0.8 cm, 1.0 cm, and 1.2 cm). Normalized visibility factors obtained with a reference delay of t_d = 600 ps are shown for static layer thicknesses of (a) d = 8 mm, (b) d = 10 mm, and (c) d = 12 mm. (d) The Fourier transform of the aforementioned signals reveals a distinct peak at 0.5 Hz, corresponding to the pump modulation frequency.

Our experimental implementation utilized a high-speed modulated DFB laser diode to establish a stable low-coherence gate. By ensuring the modulation frequency was significantly higher than the camera frame rate, we achieved an effective integration of over 1000 modulation cycles per exposure, maintaining intensity stability comparable to unmodulated states. The off-axis holographic geometry allowed for the efficient separation of the heterodyne signal in the spatial-frequency domain. Validation using a two-layer tissue-mimicking phantom confirmed that the system successfully captures flow dynamics beneath static layers with thicknesses ranging from 0.8 to 1.2 cm.

The CG-iSVS system offers several distinct advantages over traditional speckle-based flow measurement techniques. First, by removing the reliance on long SD separations, the system maximizes photon collection efficiency and improves spatial resolution, which is critical for probing highly scattering biological tissues. Second, the transition from high-speed sensors to a low-frame-rate camera significantly reduces data throughput requirements and hardware costs, facilitating the development of portable and scalable clinical devices. Furthermore, the interferometric detection scheme provides

heterodyne amplification of weak speckle fluctuations, ensuring a robust SNR even when probing deep into turbid media.

Despite these strengths, certain limitations warrant further investigation. The width of the coherence gate is a critical parameter; while a wider ToF gate improves the SNR by integrating more photons, it simultaneously reduces depth specificity. Conversely, a narrower gate enhances depth resolution but may suffer from a degraded SNR. Future work will focus on optimizing this gate width to achieve the ideal trade-off between sensitivity and signal quality for specific clinical applications. Additionally, while this work validated the technique using a controlled two-layer phantom, translating CG-iSVS to *in vivo* applications will require testing in more complex geometries that better represent the human head. Optimization of the source–detector geometry and detection sensitivity will be essential for real-time cerebral blood flow monitoring.

In summary, CG-iSVS provides a scalable and cost-effective approach to depth-selective microvascular imaging. By combining interferometric speckle visibility with coherence-based ToF filtering, this method enables depth-selective probing of dynamics while maintaining high photon efficiency. These results open new opportunities for portable, non-invasive, and clinically viable monitoring of cerebral hemodynamics.

BIBLIOGRAPHY

[1] J.-L. Fan, P. Brassard, C. A. Rickards, R. C. Nogueira, N. Nasr, F. D. McBryde, J. P. Fisher, and Y.-C. Tzeng, "Integrative cerebral blood flow regulation in ischemic stroke", Journal of Cerebral Blood Flow & Metabolism **42**, 387–403 (2022).

[2] S. Ogoh, "Relationship between cognitive function and regulation of cerebral blood flow", The journal of physiological sciences **67**, 345–351 (2017).

[3] C. Iadecola, "Neurovascular regulation in the normal brain and in alzheimer's disease", Nature Reviews Neuroscience **5**, 347–360 (2004).

[4] S. Purkayastha and F. Sorond, "Transcranial doppler ultrasound: technique and application", in Seminars in neurology, Vol. 32, 04 (Thieme Medical Publishers, 2012), pp. 411–420.

[5] A. Cenic, D. G. Nabavi, R. A. Craen, A. W. Gelb, and T.-Y. Lee, "Dynamic ct measurement of cerebral blood flow: a validation study", American Journal of Neuroradiology **20**, 63–73 (1999).

[6] J. A. Detre, D. C. Alsop, L. Vives, L. Maccotta, J. Teener, and E. Raps, "Noninvasive mri evaluation of cerebral blood flow in cerebrovascular disease", Neurology **50**, 633–641 (1998).

[7] J. Wang, H. Rao, G. S. Wetmore, P. M. Furlan, M. Korczykowski, D. F. Dinges, and J. A. Detre, "Perfusion functional mri reveals cerebral blood flow pattern under psychological stress", Proceedings of the National Academy of Sciences **102**, 17804–17809 (2005).

[8] F. F. Jöbsis, "Noninvasive, infrared monitoring of cerebral and myocardial oxygen sufficiency and circulatory parameters", Science **198**, 1264–1267 (1977).

[9] W. M. Kuebler, A. Sckell, O. Habler, M. Kleen, G. E. Kuhnle, M. Welte, K. Messmer, and A. E. Goetz, "Noninvasive measurement of regional cerebral blood flow by near-infrared spectroscopy and indocyanine green", Journal of Cerebral Blood Flow & Metabolism **18**, 445–456 (1998).

[10] R. Cubeddu, A. Pifferi, P. Taroni, A. Torricelli, and G. Valentini, "Experimental test of theoretical models for time-resolved reflectance", Medical physics **23**, 1625–1633 (1996).

[11] T. Durduran and A. G. Yodh, "Diffuse correlation spectroscopy for non-invasive, micro-vascular cerebral blood flow measurement", Neuroimage **85**, 51–63 (2014).

[12] A. Humeau, W. Steenbergen, H. Nilsson, and T. Strömberg, "Laser doppler perfusion monitoring and imaging: novel approaches", Medical & biological engineering & computing **45**, 421–435 (2007).

[13] R. Bandyopadhyay, A. Gittings, S. Suh, P. Dixon, and D. J. Durian, "Speckle-visibility spectroscopy: a tool to study time-varying dynamics", Review of scientific instruments **76** (2005).

[14] C. P. Valdes, H. M. Varma, A. K. Kristoffersen, T. Dragojevic, J. P. Culver, and T. Durduran, "Speckle contrast optical spectroscopy, a non-invasive, diffuse optical method for measuring microvascular blood flow in tissue", Biomedical optics express **5**, 2769–2784 (2014).

[15]J. W. Goodman, *Speckle phenomena in optics: theory and applications* (Roberts and Company Publishers, 2007).

[16]L. Gagnon, M. Desjardins, J. Jehanne-Lacasse, L. Bherer, and F. Lesage, "Investigation of diffuse correlation spectroscopy in multi-layered media including the human head", Optics express **16**, 15514–15530 (2008).

[17]G. Dietsche, M. Ninck, C. Ortolf, J. Li, F. Jaillon, and T. Gisler, "Fiber-based multispeckle detection for time-resolved diffusing-wave spectroscopy: characterization and application to blood flow detection in deep tissue", Applied optics **46**, 8506–8514 (2007).

[18]C. Bruschini, H. Homulle, I. M. Antolovic, S. Burri, and E. Charbon, "Single-photon avalanche diode imagers in biophotonics: review and outlook", Light: Science & Applications **8**, 87 (2019).

[19]J. D. Johansson, D. Portaluppi, M. Buttafava, and F. Villa, "A multipixel diffuse correlation spectroscopy system based on a single photon avalanche diode array", Journal of biophotonics **12**, e201900091 (2019).

[20]W. Liu, R. Qian, S. Xu, P. Chandra Konda, J. Jönsson, M. Harfouche, D. Borycki, C. Cooke, E. Berrocal, Q. Dai, et al., "Fast and sensitive diffuse correlation spectroscopy with highly parallelized single photon detection", APL Photonics **6** (2021).

[21]M. A. Wayne, E. J. Sie, A. C. Ulku, P. Mos, A. Ardelean, F. Marsili, C. Bruschini, and E. Charbon, "Massively parallel, real-time multispeckle diffuse correlation spectroscopy using a 500× 500 spad camera", Biomedical Optics Express **14**, 703–713 (2023).

[22]D. Borycki, O. Kholiqov, S. P. Chong, and V. J. Srinivasan, "Interferometric near-infrared spectroscopy (inirs) for determination of optical and dynamical properties of turbid media", Optics express **24**, 329–354 (2016).

[23]W. Zhou, O. Kholiqov, S. P. Chong, and V. J. Srinivasan, "Highly parallel, interferometric diffusing wave spectroscopy for monitoring cerebral blood flow dynamics", Optica **5**, 518–527 (2018).

[24]J. Xu, A. K. Jahromi, J. Brake, J. E. Robinson, and C. Yang, "Interferometric speckle visibility spectroscopy (isvs) for human cerebral blood flow monitoring", Apl Photonics **5** (2020).

[25]B. Zhang, C. Phillips, E. Venialgo Araujo, S. Iskander-Rizk, J. Pupeikis, B. Willenberg, U. Keller, and N. Bhattacharya, "Study of time-resolved dynamics in turbid medium using a single-cavity dual-comb laser", ACS photonics **11**, 3972–3981 (2024).

[26]J. Xu, A. K. Jahromi, and C. Yang, "Diffusing wave spectroscopy: a unified treatment on temporal sampling and speckle ensemble methods", Apl Photonics **6** (2021).

[27]Y. X. Huang, S. Mahler, J. Mertz, and C. Yang, "Interferometric speckle visibility spectroscopy (isvs) for measuring decorrelation time and dynamics of moving samples with enhanced signal-to-noise ratio and relaxed reference requirements", Optics Express **31**, 31253–31266 (2023).

[28]S. Mahler, Y. X. Huang, M. Liang, A. Avalos, J. M. Tyszka, J. Mertz, and C. Yang, "Assessing depth sensitivity in laser interferometry speckle visibility spectroscopy (isvs) through source-to-detector distance variation and cerebral blood flow monitoring in humans and rabbits", Biomedical Optics Express **14**, 4964–4978 (2023).

[29] A. Torricelli, A. Pifferi, L. Spinelli, R. Cubeddu, F. Martelli, S. Del Bianco, and G. Zaccanti, "Time-resolved reflectance at null source-detector separation:<? format?> improving contrast and resolution in diffuse optical imaging", Physical review letters **95**, 078101 (2005).

[30] J. Sutin, B. Zimmerman, D. Tyulmankov, D. Tamborini, K. C. Wu, J. Selb, A. Gulinatti, I. Rech, A. Tosi, D. A. Boas, et al., "Time-domain diffuse correlation spectroscopy", Optica **3**, 1006–1013 (2016).

[31] M. Zhao, W. Zhou, S. Aparanji, D. Mazumder, and V. J. Srinivasan, "Interferometric diffusing wave spectroscopy imaging with an electronically variable time-of-flight filter", Optica **10**, 42–52 (2023).

[32] F. Fathi, S. Mazdeyasna, D. Singh, C. Huang, M. Mohtasebi, X. Liu, S. R. Haratbar, M. Zhao, L. Chen, A. C. Ulku, et al., "Time-resolved laser speckle contrast imaging (tr-lsci) of cerebral blood flow", IEEE transactions on medical imaging (2024).

[33] A. M. Goldfain, P. Lemaillet, D. W. Allen, K. A. Briggman, and J. Hwang, "Polydimethylsiloxane tissue-mimicking phantoms with tunable optical properties", J. Biomed. Opt. **27**, 074706–074706 (2022).

6

6

Conclusion and outlook

In this thesis, we propose three diffferent techniques, dual-comb diffusing-wave spectroscopy (DC-DWS), frequency-modulated scattering holography (FMSH) and coherence-gated interferometric speckle visibility spectroscopy (CG-iSVS). We focus on optimizing the signal-to-noise ratio, deep-layer specificity and data throughput of interferometric diffuse optics. This concluding chapter summarizes the key features of proposed techniques and gives a perspective on future work.

THIS thesis investigates various interferometric diffuse optics (iDO) techniques and optimizes the system in terms of signal-to-noise ratio (SNR), deep-flow specificity, and data throughput. The research outline, as shown in Fig. 6.1, aligns with the author's scientific progression over the past four years.

6.1. CONCLUSION

In Chapter 1, we began by introducing the field of diffuse optics and its applications. We then outlined the fundamental principles of near-infrared spectroscopy (NIRS), diffuse correlation spectroscopy (DCS) or diffusing-wave spectroscopy (DWS), speckle contrast optical spectroscopy (SCOS), and laser Doppler flowmetry (LDF), discussing their respective limitations as well as current state-of-the-art techniques. This served to clarify the motivation behind the work presented in this thesis.

6.1.1. DUAL-COMB DIFFUSING-WAVE SPECTROSCOPY

In Chapter 2, we began with dual-comb optical coherence tomography (DC-OCT) and demonstrated its extension to the measurement of multiply scattered photons in turbid media. The high mutual coherence between the probe and pump combs enables sampling of the distribution of time-of-flight (DTOF), which encodes the optical properties of the medium. By repeatedly measuring the DTOF at a rate faster than the decorrelation time of the scatterers—and compensating for laser phase fluctuations using a reference interferometer—we can capture the dynamic properties of the turbid media. We analyzed the factors affecting the signal-to-noise ratio (SNR) of the dual-comb system and optimized the measurement speed, temporal resolution, and SNR.

The DC-DWS system integrates time-domain near-infrared spectroscopy (TD-NIRS) and diffuse correlation/diffusing wave spectroscopy (DCS/DWS) into a single modality, enabling simultaneous measurement of both optical and dynamic properties. This integration improves the accuracy of blood flow index (BFI) measurements and holds potential for assessing tissue metabolism. Additionally, the time-of-flight discrimination of DC-DWS helps mitigate contamination from superficial layers. As a result, the system offers an accurate, informative, and compact solution for blood flow monitoring. However, the dual-comb interferometer suffers from low photon utilization, which currently limits its applicability in in vivo settings.

6.1.2. FREQUENCY-MODULATED SCATTERING HOLOGRAPHY

To address the SNR limitations of DC-DWS, in Chapter 3, we compared the SNR and the minimum detectable photon flux across three systems: dual-comb interferometry, frequency-modulated interferometry, and photon-counting detection. Based on this analysis, we proposed a novel method—frequency-modulated scattering holography (FMSH)—which achieves comparable or potentially higher SNR than photon-counting detectors. By reducing the laser modulation speed, we lower the beat frequency between the scattered photons and the local oscillator, allowing a fast CMOS camera to record the temporal interferogram. The highly parallel detection and extended measurement duration significantly enhance the SNR, reaching levels similar to photon-counting systems.

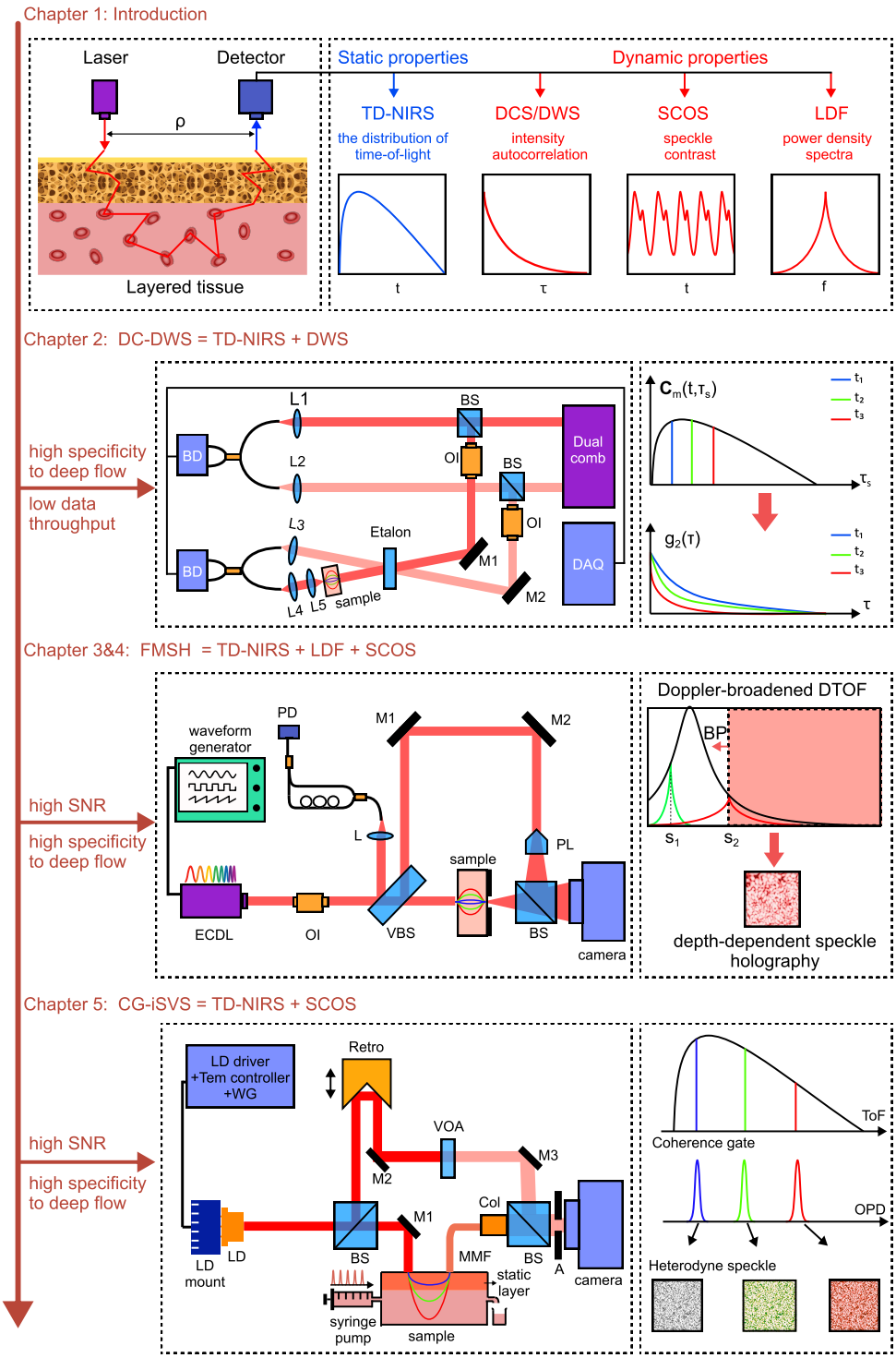

Figure 6.1: Research outline of this thesis.

FMSH is suitable for measuring the optical properties of static media. However, in dynamic media, Doppler broadening of the time-of-flight (DTOF) distribution limits its ability to accurately distinguish between the Brownian motion coefficient and the reduced scattering coefficient.

In Chapter 4, we demonstrated that by applying a bandpass (BP) filter, we can separate the DC and AC components in the time-frequency domain, resulting in heterodyne speckle holography. By computing the ensemble speckle contrast, we capture flow-related fluctuations. Moreover, by selecting different BP filters, we can extract depth-dependent speckle contrast, as photons with different DTOFs exhibit Doppler spectra shifted by different beat frequencies.

As a result, FMSH effectively integrates TD-NIRS, speckle contrast optical spectroscopy (SCOS), and laser Doppler flowmetry (LDF), enabling measurement of both optical and dynamic properties, but currently not at once.

6.1.3. COHERENCE-GATED INTERFEROMETRIC SPECKLE VISIBILITY SPECTROSCOPY

In FMSH, the bandpass (BP) filter serves as a time-of-flight (ToF) gate. However, the use of a high-frame-rate camera leads to substantial data throughput, creating challenges for real-time processing. To overcome this, Chapter 5 introduces coherence-gated interferometric speckle visibility spectroscopy (CG-iSVS). This approach replaces the frequency-modulated laser and fast camera used in FMSH with a distributed-feedback laser diode and a conventional camera. The rapid wavelength modulation of laser diode during camera exposure time provides an effective coherence gate. By adjusting the optical path length difference (OPD) between the measurement and reference arms, we selectively interfere photons with different ToFs, enabling depth-resolved heterodyne speckle contrast measurements and improving sensitivity to deep flow. CG-iSVS also offers high photon throughput while significantly reducing data throughput through the use of a low-frame-rate camera. This not only facilitates real-time processing but also lowers system cost by employing a low-frame-rate camera.

6.2. OUTLOOK

Diffuse optics have enabled non-invasive, portable, low-cost, and continuous monitoring of tissue parameters over the past decades. With growing demands in cerebral activity monitoring, there is an increasing need for systems that provide high accuracy, strong specificity to deep tissue layers, high SNR, and low data throughput. Conventional NIRS systems (e.g., TD-NIRS) can measure blood oxygenation but lack sensitivity to blood flow. In contrast, DCS and DWS techniques offer direct access to flow information but do not provide optical property measurements, leading to inaccuracies in estimating the absolute blood flow index (BFi). Integrating TD-NIRS with DCS/DWS can address this limitation.

Fundamentally, TD-NIRS operates as a light detection and ranging (LiDAR) technique by measuring the time-of-flight (ToF) of photons. In practice, DCS/DWS can be combined with both conventional ToF-based LiDAR (TD-DCS) and interferometric LiDAR approaches (e.g., iNIRS or DC-DWS in Chapter 2). However, these methods suffer

from low photon throughput, which can be mitigated through parallel detection using multiple individual detectors.

The advent of photon-counting detector (PCD) arrays offers a potential solution, yet PCDs remain costly and are highly sensitive to ambient light. Interferometric diffuse optics (iDO), in contrast, offer greater robustness to environmental light and are relatively low-cost.

In iDO, replacing many individual detectors with a camera-based system is a non-trivial but promising strategy for simplifying system architecture and reducing cost. In Chapter 3 and Chapter 4, we present a system that combines interferometric LiDAR with a camera-based detector. This approach increases photon throughput and enables measurement of optical and dynamic tissue properties.

On one hand, the Doppler-broadened DTOF model assumes homogeneous media, where the Doppler spectrum width of each photon path is proportional to its ToF. Extending this model to heterogeneous media remains an important direction for future research. On the other hand, our FMSH system currently struggles to decouple the reduced scattering coefficient from the Brownian motion coefficient. This challenge may be addressed by incorporating multi-wavelength sources.

Diffuse optics also show great promise for brain-computer interface (BCI) development. Compared with electroencephalography (EEG), optical techniques offer the advantage of non-invasively accessing deeper brain activity. Although the hemodynamic response measured optically (e.g., blood flow and oxygenation) is slower than the electrical signals captured by EEG, it provides complementary physiological information. While NIRS has recently been combined with EEG to monitor blood oxygenation, flow-sensitive measurements have yet to be widely integrated. Combining time-of-flight (ToF) gating with flow-sensitive techniques such as DCS, DWS, or SCOS holds strong potential for enabling novel optical BCI systems.

In Chapter 5, we propose a cost-effective approach that uses a wavelength-modulated distributed-feedback laser diode and a CMOS camera to measure blood flow in deep tissue layers. The coherence gate generated by the wavelength-modulation effectively suppresses superficial layer contamination even at short source-detector separations, offering high spatial resolution. These characteristics make the technique well-suited for developing compact and affordable BCI devices. However, its long-term stability and ability to reliably measure in vivo signals remain to be validated.

With the rapid advancement of iDO over the past ten years and the increasing demand for neural activity monitoring, we believe there is substantial opportunity to develop both commercial and clinically viable devices in this field.

Acknowledgements

Back in December 2020, while the world was grappling with the spread of COVID-19, I received the offer to start my PhD. It was a special, bittersweet moment; a journey into the unknown amidst a global crisis. I entered this chapter with both nerves and excitement, eager to discover what I could contribute. Looking back now, this journey has been defined by its grit and its joy, its challenges and its triumphs. But more than the work itself, it is the people who defined this experience. I have been surrounded by such excellence and kindness, and I am honored to take this moment to thank those who made this journey possible.

First and foremost, I would like to express my deepest gratitude to my promoter, who has guided me through this journey with unwavering support. **Nandini**, words truly fail to convey the appreciation for you. You have been a heartwarming, proactive, and brilliant supervisor. By granting me the freedom to explore my own research interests, you fostered a trusting environment that allowed me to grow into an independent researcher. I am especially grateful for your incredible dedication—always being there to offer guidance, regardless of whether it was a workday or a holiday. Whenever my project reached a standstill, your empathy and encouragement provided the motivation I needed to persevere. I am also deeply indebted to you for sharing your invaluable knowledge, and for working so closely with me to secure two NWO XS grants. These successes were pivotal in making this journey smoother. Beyond the laboratory, your genuine care for your students has made this a truly positive and unforgettable chapter of my life. I wish you and your family continued happiness and good health, and I look forward to seeing your career reach even greater heights in the years to come.

Secondly, **Sophinese**, you have been a remarkably dedicated supervisor. I am deeply grateful for the detailed and insightful feedback you provided every time we discussed my work. Although our backgrounds differ, your sharp scientific intuition has been a constant source of inspiration to me. During the manuscript revision process, your logical rigor and creative perspectives made the experience both more robust and truly enjoyable. I would also like to thank you for your leadership within the OPT group; your management of our meetings and outings made our group dynamic both fun and vibrant. I wish you and your family great happiness, and I wish you continued excellence in your research.

I would like to extend a big thanks to my colleague, **Esteban**. You are an exceptional researcher with a true 'first principles' mindset—and, in the best sense of the word, a real geek. I truly valued your company during our time in Zurich; although our experiment didn't succeed then, the experience we shared and our deep discussions were incredibly valuable to me. I wish you and your wife a wonderful life in Breda, and I wish you every success in your future career.

I would like to thank the members of my thesis committee-**Jennigje**, **Christian**, **Allard**, **Turgut** and **Vivek** for dedicating their time to evaluate my work. I am grateful for their presence at my defense and for providing valuable comments that significantly improved the assessment and clarification of this thesis.

Moreover, I would like to express my sincere appreciation for the stimulating scientific discussions and the unwavering support from the Ultrafast Laser group at ETH Zurich, especially **Christopher**, **Justinas**, **Benjamin**, and **Ursula**. I truly enjoyed our collaboration; your professionalism and deep expertise made this process much smoother, and I have learned an immense amount from our time together.

To my PME colleagues with whom I have spent the past few years:

Fabian, you are an exceptional physicist; your solid grasp of fundamental physics is truly impressive. Thank you for our discussions on diffuse optics. I wish you a major breakthrough in your research and much happiness for you and your wife.

Sabina, you are a brilliant researcher whose achievements over the last few years have inspired many "newbies" as they begin climbing the mountain of science. Thank you for being so welcoming whenever we met in your office. I wish you continued success in your career.

Marcel, thank you for organizing the MIMIC meetings. I learned a great deal from those entrepreneurs and researchers, and I hope the event becomes even more successful in the future.

Hassan, thank you for your wisdom and for serving on my Go-NoGo committee and as a reserve member of my doctoral defense. Your career is already a great success, and I wish you and your family continued happiness.

Andres, you are a truly interesting person; thank you for your kind greetings every time I met with Nandini. I wish you happiness every day.

Inge, thank you for the Dutch desserts and for working with us during the most difficult times for the OPT group. I sincerely apologize for interrupting your interlock so many times! I wish you and your family the very best.

Filippo, you are a kind person and a pleasure to work with. Thank you for sharing the camera, which was vital to my work. I wish you great success with your PhD.

Hamed, thank you for your insightful comments in every group meeting. I wish you a successful career and much happiness with your wife.

Ruben, thank you for the discussions regarding ASOPS measurements; they provided me with many valuable insights. I wish you great success in your research and many breakthroughs in your future projects.

Hava and **Hande**, thank you for the fascinating discussions about astrology; they were a wonderful distraction and a joy to share. I wish you both immense happiness and continued success in everything you do.

Peiyu, thank you for the wonderful dishes you brought to every party. **Yuchen**, thank you for your company at every conference and workshop. I wish you both great success in your PhD journeys.

Sifeng, thank you for organizing our parties and for always taking care of the cleanup afterward. I wish you the best in your career, whether in industry or academia.

Yang, thank you for your jokes; you are truly the "life of the party." I wish you great success in your career.

Minxing, thank you for your insights into the stock market. I wish you much success in your future career.

Zichao, thank you for the "Rou-Sheng" deliveries; I wish you great success in your career and a life full of joy.

Mingkai, thank you for those wonderful noodles; I wish you all the best in your research and future endeavors.

Xiliang, thank you for the desserts; your optimism always lights up our parties. I wish you a future as bright and sweet as your treats.

Zhichao, thank you for the thoughtful arrangements for the reception; I wish you a smooth path ahead in your professional journey.

Zhiwei, thank you for providing fruit after lunch; I wish you a fruitful career and happiness in every step you take.

Ze, thank you for the handmade baozi; I wish you continued success in your PI and a very happy life.

Xinxin, thank you for hosting the wonderful hotpot parties; I wish you a warm and prosperous future.

Kai, thank you for taking care of "Xiaoma" every time; I wish you great fulfillment in both your work and family.

Yuheng, thank you for the great conversations and discussions at every party; I wish you endless inspiration for your future research.

Chao, thank you for the jokes and the lively talks; I wish you a career filled with laughter and brilliant achievements.

Zhiling, thank you for being my fitness partner; I wish you and your wife a lifetime of health and happiness together.

Hanqing, you are an inspiration to all of us. Thank you for the barbecue, and I wish you a pioneering career and a wonderful family life.

Ruibo, thank you for your warm hospitality during my stay in Shanghai; I wish you a flourishing career and much success in your home city.

Rui, thank you for the insightful discussions on optics; I wish you many groundbreaking discoveries in your scientific career.

Huihui, thank you for your valuable suggestions on noise removal; I wish you continued success in your academic career, many more groundbreaking publications, and a truly brilliant future as a distinguished scholar.

Yueyue, thank you for the delicious desserts and the wonderful dishes you prepared; I wish you great happiness in your life and every success in your future endeavors.

We also have many wonderful PhD candidates and postdocs within the PME department who make our environment feel like one large family. In particular, I would like to mention **Mengxi**, **Ata Yong**, **Yujiang**,**Lidan**,**Xuerong**, **Xueying**, **Kaiwen**, **Tufan**, **Paulina**, **Bas**, **Thomas**, **Pierre**, **Kushal**, **Sahar**, **Javad**, **Anna**, **Enise**, **Chris**, and **Kai**... Although this list is quite long and I cannot name everyone individually, please know that your presence made a difference. I wish you all the very best of luck and great success in your future careers.

To the master students I have had the pleasure of working with—**Nan**, **Wenpei**, **Marco**, **Xuzheng**, and **Joyce**: thank you for your hard work and dedication throughout this journey. It was a wonderful experience collaborating with you, and I truly enjoyed

our time in the lab together. I wish you all great success in your future careers and hope you achieve all your professional goals.

In addition, I would like to express my sincere gratitude to the secretaries and technicians who have provided immense help throughout this journey. In particular, I would like to thank **Lisette**, **Gaby**, **Marli**, **Sylviane**, **Natalija**, and **Eveline** for their patient administrative support, which made my life much easier.

I am also deeply grateful to **Rob**, **Patrick**, **Alex**, **Bradley**, **Gideon**, and **Spiridon** for their technical expertise and assistance in the lab. Thank you for your hard work and for always being ready to help solve the most challenging technical issues. I wish you all continued success in your roles, good health, and much happiness in your personal lives.

I would like to express my gratitude to my mountaineering partner, **Zhaochong**. Your passion for life is truly inspiring, and I will never forget our camping trips across the Alps. I wish you great success in your career and look forward to many more adventures in the future.

Pan, your enthusiasm for research and your bravery in life have been a guiding light to me. I wish you continued success and all the very best as you navigate your professional and personal journey.

Shenreng, thank you for being a wonderful companion during our Zugspitze adventure. I wish you immense success with your startup; may it reach new heights.

Kai and **Xuan**, thank you for the tasty dishes you brought to every party and for the unforgettable journey we shared in Italy. I will never forget that hot summer and the shared frustration when our travel was delayed in Catania. I wish you both a future filled with smoother travels and great success in your lives.

Keifei, thank you for introducing me to this opportunity and for all the insightful discussions regarding frequency combs. Your guidance was instrumental in the early stages of my work. I wish you continued success in your research and a brilliant future ahead.

Furthermore, I would like to thank **Weiwei** for your companionship throughout this journey. You have taught me so much over the past few years. I wish you true happiness and hope you find the lifelong goals and passions you wish to strive for.

In the end, some words to **my parents**:

河山万里长，不若高堂暖。阿爷，妈妈，感谢你们多年的坚守和默默付出，给我提供的温暖港湾。未来，换我做你们的依靠！

Binbin Zhang
February 2026

About the author

Binbin Zhang was born on February 19, 1996, in Lujiang, China. He attended **Lujiang Middle School** from 2011 to 2014, where he completed his high school education.

In 2014, he began his undergraduate studies in **Measurement and Control Technology and Instrument Engineering** at **Hefei University of Technology** in Hefei, China. He completed his bachelor's degree in 2018 under the supervision of Prof. Jin Zhang. His graduation project focused on **visual navigation of unmanned aerial vehicle (UAV)**.

Following his undergraduate studies, he was recommended for direct admission to the master's program **Instrument and Meter Engineering** at **Tianjin University**, where he pursued research under the supervision of Prof. Xinghua Qu and Prof. Fumin Zhang. He completed his master's degree in 2021, with his thesis focusing on **multi-target ranging based on frequency-modulated-continuous-wave LiDAR**.

In April 2021, he began his PhD research in the group **Optics for Technologies** at **Delft University of Technology** under the supervision of Dr. Nandini Bhattacharya and Dr. Sophinese Iskander-Rizk. His research focused on determining **the optical and dynamic properties of turbid media using interferometric diffuse optics**. The results of this research are presented in this thesis.

List of Publications

Journal paper

4. **Binbin Zhang**, Christopher Phillips, Esteban Venialgo Araujo, Sophinese Iskander-Rizk, Justinas Pupeikis, Benjamin Willenberg, Ursula Keller, and Nandini Bhattacharya, *Study of time-resolved dynamics in turbid medium using a single-cavity dual-comb laser.* ACS photonics 11.10 (2024): 3972-3981..

3. **Binbin Zhang**, Sophinese Iskander-Rizk and Nandini Bhattacharya, *Measurement of optical and time-of-flight-gated dynamic properties of turbid media with photon-counting sensitivity using frequency-modulated scattering holography.* opticaopen.30576617.

2. **Binbin Zhang**, Xuzhen You, Sophinese Iskander-Rizk and Nandini Bhattacharya, *Coherence-gated interferometric speckle visibility spectroscopy (CG-iSVS) with higher spatial resolution and lower cost*, in preparation.

1. **Binbin Zhang**, Marco Loddo, Sophinese Iskander-Rizk and Nandini Bhattacharya, *Deciphering laminar flow in diffuse correlation spectroscopy via modified born series*, in preparation.

Conference contribution

3. **Binbin Zhang**, Christopher Phillips, Esteban Venialgo Araujo, Sophinese Iskander-Rizk, Justinas Pupeikis, Benjamin Willenberg, Ursula Keller, and Nandini Bhattacharya. *Dual comb diffuse correlation spectroscopy*In Neural Imaging and Sensing 2024, p. PC128280K. SPIE, 2024. (Oral).

2. **Binbin Zhang**, Sophinese Iskander-Rizk and Nandini Bhattacharya. *Determination of depth-dependent dynamic properties of turbid media using frequency-modulated scattering holography.* In European Conferences on Biomedical Optics 2025. (Oral).

1. **Binbin Zhang**, Sophinese Iskander-Rizk, and Nandini Bhattacharya. *Depth-resolved dynamics in turbid media via frequency-modulated scattering holography* In The European Optical Society Annual Meeting, 2025. (Oral).

Patent

2. **Binbin Zhang**, Nandini Bbhattacharya. *Depth-dependent dynamic properties measurement device using multiple-wavelength digital holography,*under review.

1. Nandini Bbhattacharya, **Binbin Zhang**. *Optical detection*, WO2024172654A1, 2024-08-22.

TU Delft ISBN: 978-94-6384-927-2